UNIVERSITY of CALIFORNIA

Santa Barbara

Electronic Functionality in Complex Palladium Oxides

A Dissertation submitted in partial satisfaction of the

requirements for the degree

Doctor of Philosophy

in

Materials

by

Leo Kennedy Lamontagne

Committee in charge:

Professor Ram Seshadri, Chair

Professor Stephen Wilson

Professor Gabriel Ménard

Professor Anton Van der Ven

March 2018

The dissertation of Leo Kennedy Lamontagne is approved.

Professor Stephen Wilson

Professor Gabriel Ménard

Professor Anton Van der Ven

Professor Ram Seshadri, Committee Chair

February 2018

Electronic Functionality in Complex Palladium Oxides

by

Leo Kennedy Lamontagne

for my family

Acknowledgments

Firstly, thank you to my advisor, Professor Ram Seshadri, for his guidance throughout the past several years. I am incredibly fortunate to have had the opportunity to work with and learn from him and appreciate his mentorship. I am continually impressed with the investment Ram takes in his students and their growth, both professional and personal. I would also like to thank the rest of my committee, Professors Anton Van der Ven, Stephen Wilson, and Gabriel Ménard for their guidance.

A huge thanks must be given to all of the members of the Seshadri lab, past and present. It has been a privilege to work with such an amazing group of intelligent, hard-working, and supportive people. Special thanks to Professor Geneva Laurita for joining me on Team Palladium and providing training, insights, and fruitful discussions. I have had the great pleasure of working with three incredibly talented undergraduate interns: Huma Yusuf, Mike Knight, and Shahryar Mooraj, and appreciate all of their help.

Thank you to all of the MRL staff, both technical and administrative, for all of their assistance throughout my graduate studies. From fixing equipment, processing reimbursements, and correcting purchase orders, I am thankful for all of their work. Thanks to Dr. Amanda Strom for her continuous efforts to

maintain the TEMPO lab. I'd like to think I helped fix more instruments than I broke, but she might disagree. Thanks to Dr. Jerry Hu, Jaya Nolt, and Shamon Walker for their assistance with NMR experiments.

I am grateful for Dr. Julie Standish and the rest of the MRL education and outreach staff for giving me the opportunity to share my passion for science with many elementary school students in Santa Barbara and undergraduate students from across the globe. Seeing kids get so excited at Science Night demonstrations was a great way to keep myself optimistic and invested in my own research. Super mentoring for the summer internship programs was a valuable experience that not only helped me develop professionally, but also allowed me to befriend people all over the world.

Thank you to all of my friends, especially those that I have made during my time here in Santa Barbara, particularly Kristin, Chelsea, Jason, Molleigh, Doug, Geneva, Chris, Megan, Ryan, and Ignacio. From our valley wine tastings, polo matches, nights out downtown, beach days, and many other adventures, I am thankful for all of the people with whom I was able to experience the west coast. Much more than the perfect weather, it is these relationships I will miss the most as I begin the next chapter of my life.

Most importantly, thank you to my family. The love and support of Mom,

Dad, Will, Laura, Donna, Auntie Tricia, Auntie Kathy, and my grandparents was absolutely crucial to the work presented in this document.

Curriculum Vitae

Leo K. Lamontagne

Education

Ph.D. Materials, University of California, Santa Barbara March 2018

Advisor: Professor Ram Seshadri

B.S. Chemistry and Mathematics, Boston College. June 2013

Magna Cum Laude, College of Arts and Science Honors Program

Advisor: Professor Chia-Kuang (Frank) Tsung

Publications

7. M. Buffon, G. Laurita, **L. K. Lamontagne**, E. Levin, S. Mooraj, D. Lloyd, N. White, T. Pollock, R. Seshadri, Thermoelectric Performance and the Role of Anti-site Disorder in the 24-Electron Heusler $TiFe_2Sn$, *J. Phys. Condensed Matter* **29** (2017) 405702(1-7). [**doi**]

6. **L. K. Lamontagne**, G. Laurita, M. Knight, H. Yusuf, J. Hu, R. Seshadri, K. Page, The Role of Structural and Compositional Heterogeneities in the Insulator-to-Metal Transition in Hole-Doped APd_3O_4 (A = Ca, Sr) *Inorg. Chem.* **56** (2017) 5158–5164. [**doi**]

5. M. L. C. Buffon, G. Laurita, N. Verma, **L. K. Lamontagne**, L. Ghadbeigi, D.

L. Lloyd, T. D. Sparks, T. M. Pollock, R. Seshadri, Enhancement of Thermoelectric Properties in the NbCoSn Half- Heusler/Heusler System Through Spontaneous Inclusion of a Coherent Second Phase, *J. Appl. Phys.* **120** (2016) 075104(1-8). [**doi**]

4. **L. K. Lamontagne**, G. Laurita, M. W. Gaultois, M. Knight, L. Ghadbeigi, T. D. Sparks, M. E. Gruner, R. Pentcheva, C. M. Brown, R. Seshadri, High Thermopower with Metallic Conductivity in *p*-Type Li-Substituted $PbPdO_2$, *Chem. Mater.* **28** (2016) 3367–3373. [**doi**]

3. K. Hofmann, N. Kalyon, C. Kapfenberger, **L. K. Lamontagne**, S. Zarrini, R. Berger, R. Seshadri, B. Albert, Metastable Ni_7B_3 - a New Paramagnetic Boride From Solution Chemistry, and its Crystal Structure, *Inorg. Chem.* **54** (2015) 10873–10877. [**doi**]

2. B. T. Sneed, C. N. Brodsky, C. H. Kuo, **L. K. Lamontagne**, Y. Jiang, Y. Wang, F. Tao, X. Huang, C.-K. Tsung, Nanoscale-Phase Separated Pd-Rh Boxes Synthesized Via Metal Migration: an Archetype for Studying Lattice Strain and Composition Effects in Electrocatalysis, *J. Am. Chem. Soc.* **135** (2013) 14691–14700. [**doi**]

1. **L. K. Lamontagne**†, C. H. Kuo†, C. N. Brodsky, L.Y. Chou, J. Zhang, B. T. Sneed, and C.-K. Tsung, The Effect of Lattice Strain on the Catalytic

Properties of Pd Nanocrystals, *ChemSusChem.* **6** (2013) 1993–2000. [**doi**]

Abstract

Electronic Functionality in Complex Palladium Oxides

by

Leo Kennedy Lamontagne

The study of the electronic and magnetic properties of 4d transition metal oxides is crucial in developing new functional materials while also informing the origins of favorable properties in the highly studied 3d transition metal oxides. In particular, complex palladium oxides represent one subset of 4d transition metal oxides which have received comparatively little attention in regards to their electronic functionality despite reports of interesting electronic properties in the form of compositionally driven insulator-metal transitions. Several semiconducting complex palladium oxides have been shown to be driven metallic upon hole-doping with alkali metals prompting the study of their functional properties for applications such as thermoelectrics. In addition, there exists opportunities for bettering the fundamental understandings of insulator-metal transitions and, more generally, hole-doping in oxides as these complex palladium oxides are diamagnetic with comparatively small amounts of electron-

electron correlation and spin orbit coupling. We present here detailed structural studies of several complex palladium oxides and their resulting electronic properties upon hole-doping. We report that some do show favorable thermoelectric performance and remark on how structural changes imparted by aliovalent hole-dopants can influence functional properties.

First, we discuss the thermoelectric performance of Li-substituted $PbPdO_2$. Upon Li substitution, a decrease in electrical resistivity by over an order of magnitude is observed without a precipitous drop in the Seebeck coefficient leading to a zT of 0.12 at 600 K. The electronic properties of Li-substituted $PbPdO_2$ are near identical to those of the high performing cobaltate thermoelectrics despite the lack of a high degree of spin degeneracy which is believed to be the origin of the favorable properties in the cobaltates. Electronic structure calculations support experimental measurements and conclude that aspects of the band structure derived from the palladium square planar coordination contribute to the performance.

Following this work, we report on a structurally similar material, $LiBiPd_2O_4$. Hole-doping was achieved through Li substitution for Pd as before and through Pb substitution for Bi. Both methods of hole-doping decreased the electrical resistivity by over three orders of magnitude. Despite this decrease, the resistivity remains too high for thermoelectric applications. Owing to a differing

connectivity of the Pd square planes, $LiBiPd_2O_4$ possesses a much higher band gap, leading to the higher resistivity. ^{7}Li solid state nuclear magnetic resonance (NMR) reveals many distinct Li environments arise with Pb substitution. This implies an asymmetric distribution of hole-dopants and may be related to formations of more conductive regions of the material in an insulating matrix.

Next, we study the impact of hole-doping in two isostructural compounds, $SrPd_3O_4$ and $CaPd_3O_4$. Both semiconducting materials have been shown previously to be driven metallic with substitution onto the Sr/Ca site, though reports of the doping level necessary vary widely. Under our preparation and processing condtions, $Ca_{1-x}Na_xPd_3O_4$ is driven metallic above $x = 0.10$, while $Sr_{1-x}Na_xPd_3O_4$ remains semiconducting up to $x = 0.20$. Nearly identical electronic structures imply that there are local structural differences which affect the bulk properties. We observe through sensitive probes including, synchrotron X-ray diffraction (XRD), pair distribution function analysis of total neutron scattering data, and ^{23}Na NMR that indeed there exists larger amounts of local disorder in the Sr compounds. ^{23}Na NMR further reveals the presence of two distinct Na environments one of which aligns with the Na environment in metallic $NaPd_3O_4$ providing evidence of the presence of a percolative insulator-metal transition mechanism.

To further understand the role local disorder and dopant distributions have

on the observed electrical properties, we used Li, and K as dopants in addition to Na. While Li appears to distribute evenly throughout $SrPd_3O_4$, a distinct second phase emerges in $Sr_{0.8}K_{0.2}Pd_3O_4$. Density functional theory calculations (DFT) support our experiments in that it predicts differing behavior when K is used as a dopant versus Li or Na. DFT suggests that K will order when substituted into $SrPd_3O_4$ though the presence of an ordered phase or of clustered KPd_3O_4 can not be determined through synchrotron XRD. The electrical resistivity decreases slightly with increasing size of the hole dopant, but is not drastically affected. There is no evidence of a second phase emerging in $Ca_{0.8}K_{0.2}Pd_3O_4$.

Contents

List of Figures

List of Tables

Chapter 1

Introduction: Complex Palladium Oxides

1.1 Introduction to 4d transition metal oxides

Transition metal oxides are among the most studied classes of materials in solid state chemistry and condensed matter physics. Displaying a wide array of structural, electronic and magnetic properties[1], transition metal oxides are some of the highest performing materials for a wide array of applications. To name a few well known examples, $LiCoO_2$ is the prototypical battery material for almost all portable devices, $Pb_{1-x}Zr_xTiO_3$ is the state of the art piezoelectric

for applications in many electronics, and the copper oxide superconductors are at the heart of high T_c superconductivity research. Despite the large volume of literature relating to transition metal oxides, the bulk of it has been primarily focused toward those containing 3d transition metals. The more localized 3d orbitals lead to a high degree of electron-electron correlation which can give rise to interesting physical phenomena. This is related to the lower crystal field splitting of the 3d orbitals which can lead to unpaired spins and partially filled bands, resulting in interesting magnetic and electronic properties. A comparatively smaller body of work has examined the 4d and 5d transition metal oxides. The heavy 5d transition metals exhibit significant amounts of spin-orbit coupling (SOC) which is attractive to many condensed matter physicists looking to explore new fundamental physics and their resulting electronic and magnetic properties. [2–4]

4d transition metal oxides lie in between with smaller electron-electron correlations than the 3d metals due to their more dispersive 4d orbitals, yet weaker SOC than the 5d metals due to their lower atomic mass. In spite of this, a host of interesting properties are also found in 4d transition metal oxides. $SrMoO_3$ is among the most conducting transition metal oxides, [5] while rare earth molybdenum pyrochlores exhibit unusual magnetotransport properties.[6] $SrRuO_2$ was the first transition metal oxide not containing Cu

to exhibit superconductivity.[7] In regard to magnetic properties, 4d transition metal oxides may have much higher magnetic transition temperatures than their 3d structural analogues owing to the increased orbital overlap driven by their more dispersive d orbitals. $SrTcO_3$ is an extreme example of this with a Néel temperature of 1023 K. [8] In addition to impressive functional properties in their own right, research into 4d structural analogues of important 3d transition metal oxides can provide insight into understanding and improving their functional properties. For example, the structural chemistries of $LiRuO_2$ and $LiRhO_2$ as battery cathodes have been studied to better understand those of $LiCoO_2$ derivatives.[9, 10]

Among the 4d transition metals, the later ones are perhaps the least studied (barring Tc). Not only are these metals rather expensive (Rh, Pd, and Ag), they are also comparatively more electronegative than earlier transition metals. This oxophobic nature, which while favorable for catalysis, makes the preparation of oxides containing these metals difficult as the high temperatures necessary for solid state reactions frequently leads to reduction of the metal oxide precursors.[11] Nevertheless, oxides of these elements span a diverse range of structure types and functional properties. Detailed studies of these materials can inform fundamental relationships between structure and properties, while also potentially realizing new functionality for material applications. The focus here

is on the electronic functionality of complex palladium oxides. In particular, we study the nature of hole-doping in these materials which has been demonstrated to drive insulator-metal transitions. Deeper understandings of the mechanisms of these transitions is of fundamental interest and may also present the possibility of new materials for thermoelectric applications.

1.2 Overview of Complex Palladium Oxides

As a 4d transition metal with 8 d–electrons, the vast majority of complex palladium oxides exist in a diamagnetic, $2+$ oxidation state with square planar coordination. This tendency can be explained by examining palladium's position in the periodic table. Nickel, the 3d metal directly above palladium, possesses smaller crystal field splitting owing to its less disperse 3d orbitals. Small crystal field splitting leads to coordination environments that maximize the number of unpaired electrons. As a result, NiO crystallizes in a rock-salt structure with Ni atoms at the center of octahedra. Below palladium, platinum is a heavy 5d transition metal. Relativistic contraction of the 6s orbital destabilizes the 5d orbitals leading to higher oxidation states being more favored.[12, 13] Thus, PtO_2 with octahedrally coordinated d^6 Pt^{4+} is the most common simple oxide of platinum. Palladium, as a 4d metal, has large crystal field splitting, yet does not experi-

ence significant relativistic effects. These properties lead to an overwhelming propensity toward square planar configuration.

Octahedral crystal field splitting and square planar splitting are closely related. The relationship between the two, as well as the crystal structure of PdO, is demonstrated in Figure 1.1. Starting from an octahedral coordination, the two bonds pointing in the z-direction are elongated until they are effectively removed, leaving a square planar coordination. d–orbitals with a z component are thus more stabilized as less electron–electron repulsion is present. The d_{z^2} orbital which points directly along the z–axis is greatly stabilized in square planar configuration. Likewise, the d_{xy} and $d_{x^2-y^2}$ which primarily point along the xy plane are destabilized as electron-electron repulsion increases in those directions. For an atom with 8d electrons like Pd^{2+}, this configuration maximizes the crystal field stabilization.

Generally, PdO is the only stable simple oxide of palladium. The crystal structure and connectivity of the Pd square planes is shown in Figure 1.1. PdO exhibits both corner connected and edge connected square planes. The connectivity of the square planar units in reported complex palladium oxides varies and affects the observed catalytic and electronic properties. Most reported complex palladium oxides consist of a rather electropositive cation which helps stabilize the material against reduction. The electropositive cation serves to “soften” the

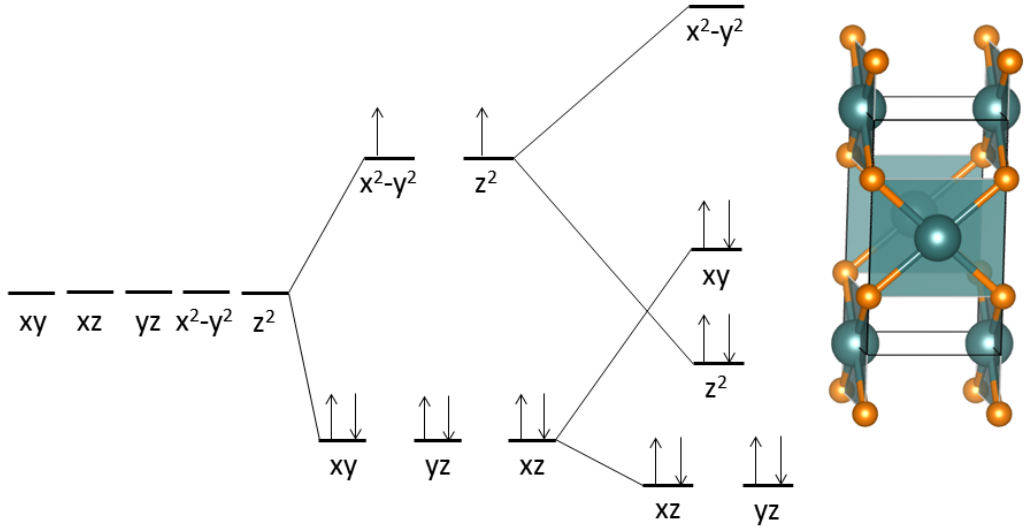

Figure 1.1: d-splitting of square planar coordination related to an octahedral crystal field. Orbitals with a z component are stabilized as the ligands along those directions are removed. The crystal structure of PdO with Pd in green, and O in orange is given as an example of this square planar coordination.

oxygen, destabilizing the O-p states, and resulting in increased covalency in the Pd-O bonds.[11, 14]This increased covalency serves to further increase the crystal field splitting resulting in an even greater propensity for Pd^{2+} to remain in a square planar coordination.

Reports of complex palladium oxides with Pd in oxidation states other than $+2$ or in coordinations other than square planar are few. The most common example of Pd^{+} is the delafossite $PdCoO_2$ which possesses an extraordinarily high electrical conductivity. [15] High pressures are typically required to stabilize Pd in higher oxidation states higher than $2+$. [16–18] Pd^{4+} coordinates in an octahedral arrangement with neighboring oxygen which results in filled t_{2g} levels and diamagnetism. Pd^{3+} is even more rare with the perovskite $LaPdO_3$ being the only existing example.[19] At this oxidation state, there exists an unpaired electron and paramagnetic behavior is observed.

There exist a handful of examples in which Pd^{2+} is octahedrally coordinated in an oxide. This is remarkable as it leaves two unpaired electrons on each Pd atom providing opportunities for studies of 4d magnetism. $PdAs_2O_6$ is an antiferromagnet with a Néel temperature of 140 K.[20] Isostructural compounds with $3d$ metals, $MnAs_2O_6$, $CoAs_2O_6$, and $NiAs_2O_6$, have Néel temperatures of 13 K, 20 K, and 30 K, respectively[21]. Further evidence of higher magnetic transition temperatures with 4d metals is seen in PdF_2 with a Néel temperature of 217 K,

[22] much higher than that of NiF_2 at 73 K. [23] A final example of octahedral Pd^{2+} is $Pd(S_2O_7)$ with a ferromagnetic transition at 12 K. [24] It is evident that more electronegative counter-ions are necessary to weaken the crystal field splitting of the 4d orbitals and promote octahedrally coordinated Pd^{2+}. This creates a great challenge in the preparation of these materials because, as previously mentioned, more electropositive cations are generally necessary to provide stability in complex palladium oxides. Thus, the known examples of magnetic palladium oxides are rather unstable and extremely air and moisture sensitive.

An attractive property of many complex palladium oxides, and the primary focus of this work, is their ability to be readily hole-doped. As discussed, the square planar crystal field splitting leads most complex palladium oxides to be diamagnetic, band semiconductors. The band gaps can be rather small based on the connectivity of the square planes, and the Pd 4d states make up a significant fraction of the states proximal to the Fermi level. These factors prompt holes doped into the valence band to be mobile and drive metallic behavior in many complex palladium oxides. PdO is the most simple example of this effect in which only 1% Li substitution onto the Pd site results in a transition from semiconducting behavior (increasing electrical resistivity with decreasing temperature) to metallic behavior (decreasing electrical resistivity with decreasing temperature). [25] Complex palladium oxides are an ideal playground in which

to study the fundamental phenomena and mechanisms of these transitions as the effects of electron-electron correlations, spin-orbit coupling, and magnetism are limited.

1.3 Insulator-Metal Transitions and Hole-Doping in Oxides

The study of insulator-metal transitions has attracted a considerable amount of attention from solid-state chemists and condensed matter physicists and continues to be a fruitful research area for both fundamental science and functional applications.[26–28] The diverse natures of these transitions are a subject of intense discussions in a search for more complete understandings. Indeed, this is clearly evident in the simple vanadium oxides. Since the 1950's, it has been known that a temperature driven insulator-metal transition in various vanadium oxides can result in an extreme changes of electrical resistivity by over 5 orders of magnitude at a range of temperatures.[29] However, the driving force behind these transitions, whether its caused by a structural Pierels distortion, driven by electron-electron correlation, or some combination of the two is still a matter of debate even today. [30–33]

A compilation of many materials systems that undergo similar temperature driven insulator-metal transitions is given in Figure 1.2 from Professor James Rondinelli at Northwestern. The location of the bar corresponds to the insulator-metal transition temperature (T_{MIT}) and the height and location represents the magnitude of the resistivity before and after the transition. Understanding these transitions and how to control their transition temperature and electrical resistivity change is crucial for their use in a number of electronic applications. Beyond temperature driven transitions, other mechanisms include, pressure, photo-induced, and compositionally driven insulator-metal transitions. [27, 28]

Compositionally driven insulator-metal transitions, like in many complex palladium oxides, involve the doping of carriers into a material in order to drive it from an insulating or semiconducting state, into a metallic one. This can be accomplished through electron or n-type doping which inserts electrons into the conduction band of a material, or through hole or p-type doping which involves the removal of electrons from the valence band, or equivalently the insertion of holes into the valence band. Understanding how these transitions progress and controlling the extent of the transition is important for a number of applications such as increasing the superconducting transition temperature in the high T_c cuprates, [34], or optimizing the power factor in thermoelectric materials. [35]

Compositionally driven insulator-metal transitions in complex palladium ox-

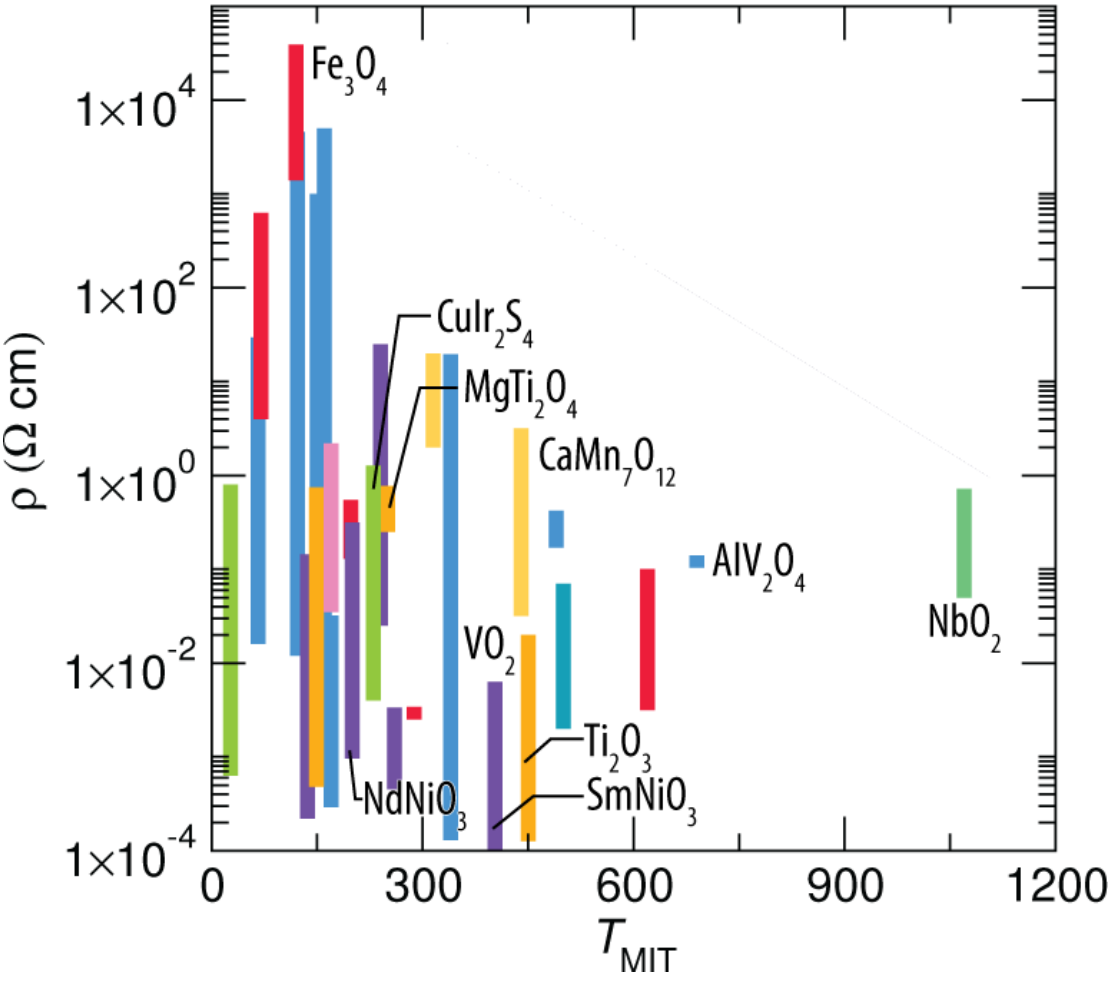

Figure 1.2: Resistivity versus temperature of various materials undergoing temperature driven insulator-metal transitions. The bar location is the temperature of the transition while the bar height describes the change in resistivity across the transition.

ides are rather rare examples of non-magnetic oxides that can be successfully hole-doped. It is common for hole-doping attempts in oxides to result in immobile, localized holes on the oxygen atoms. This problem is clearly illustrated in the field of transparent conducting oxides (TCOs) in which n-type tin doped indium oxide possess great carrier mobility, while the search for comparable p-type materials remains ongoing. [36, 37] Thus, from a fundamental perspective, understanding hole-doping in complex palladium oxides and the related insulator-metal transition mechanisms is a fruitful endeavor. In addition, the high thermoelectric performance in many degenerately doped semiconductors further prompts the study of these transitions in complex palladium oxides for functional applications.

1.4 Oxide Thermoelectrics

As about half of all energy produced in the United States is lost as waste heat, [38], utilizing thermoelectric materials, which convert a heat gradient into electricity, to recapture this lost energy is an appealing notion. Oxide materials in particular are ideal for certain thermoelectric applications due to their high temperature air stability. [39, 40] The performance of a material as a thermoelectric is governed by its dimensionless figure of merit, ZT, given below

$$ZT = \frac{S^2}{\kappa\rho}T \tag{1.1}$$

in which S is the Seebeck coefficient, κ is the thermal conductivity, ρ is the electrical resistivity, and T is the temperature.

A high Seebeck coefficient corresponds to a larger voltage created across a given temperature gradient over a material. Thermal conductivity should be as low as possible to ensure a strong temperature gradient, and electrical resistivity should be minimized to promote charge flow. The Seebeck coefficient and electrical resistivity can be thought of as contraindicated properties as the Seebeck coefficient is increased with increasing effective carrier mass and low carrier concentrations, while the electrical resistivity is lowered with lower effective masses and higher carrier concentrations. Correspondingly, insulators have larger Seebeck coefficients, typically hundreds of μV/K, with prohibitively high electrical resistivities. Conversely, metals have low electrical resistivities and also near zero Seebeck coefficients. Thus, it is of no surprise that high thermoelectric performance is found in many doped semiconductors or semimetals in which the electrical resistivity is sufficiently low without a precipitous drop in the Seebeck coefficient. The electronic properties of a given thermoelectric material can be optimized through doping, but both can rarely be simultaneously

improved, and thus large improvements in the figure of merit of electronically optimized materials are primarily achieved by lowering the thermal conductivity.

It is of interest to explore new materials for thermoelectric applications which may have intrinsically favorable electronic properties. The discovery of a high Seebeck coeffcient with metallic resistivities in Na_xCoO_2 has prompted an increased effort in the field of oxide thermoelectrics.[41] Research has since attributed this high performance to a high degree of spin degeneracy on the mixed $3+/4+$ cobalt ions. [42] Most of the state of the art oxide thermoelectrics are cobalt based and structurally analogous to Na_xCoO_2. Still, a promising n-type oxide thermoelectric remains elusive, prompting the study of new materials systems to better understand design principals and search for high performance.

Chapter 2

High Thermopower with Metallic Conductivity in p-Type Li-Substituted $PbPdO_2$

$PbPdO_2$ is a band semiconductor with a band gap arising from the filled d^8 nature of square-planar Pd^{2+}. We establish that hole doping through Li substitution for Pd in $PbPdO_2$ results in a p-type metallic oxide with a positive temperature coefficient of resistance for substitution amounts as small as

[1]The contents of this chapter have substantially appeared in Reference[43]. Reproduced with permission from : L. K. Lamontagne, G. Laurita, M. W. Gaultois, M. Knight, L. Ghadbeigi, T. D. Sparks, M. E. Gruner, R. Pentcheva, C. M. Brown, R. Seshadri, High Thermopower with Metallic Conductivity in *p*-Type Li-Substituted $PbPdO_2$, *Chem. Mater.* **28** (2016) 3367–3373. Copyright 2016 American Chemical Society.

2 mol % of Li for Pd. Furthermore, $PbPd_{1-x}Li_xO_2$ demonstrates a high Seebeck coefficient, and is therefore an oxide thermoelectric material with high thermopower despite the metallic conductivity. Up to 4 mol % Li is found to substitute for Pd as verified by Rietveld refinement of neutron diffraction data. At this maximum Li-substitution, the resistivity is driven below the Mott metallic maximum to $3.5\times10^{-3}\,\Omega\,$cm with a Seebeck coefficient of 115 μV/K at room temperature which increases to 175 μV/K at 600 K. These electrical properties are almost identical to the well-known p-type oxide thermoelectric Na_xCoO_2. Non-magnetic Li-substituted $PbPdO_2$ does not possess a correlated, magnetic state with high spin degeneracy as found in some complex cobalt oxides. This suggests that there are other avenues to achieving high Seebeck coefficients with metallic conductivities in oxide thermoelectrics. The electrical properties coupled with the moderately low lattice thermal conductivities allow for a zT = 0.12 at 600 K; the maximum temperature measured here. The trend suggests yet higher values at elevated temperatures. First-principles calculations of the electronic structure and electrical transport provide insight into the observed properties.

2.1 Introduction

Thermoelectric materials develop an electrical potential when subject to a temperature gradient owing to the Seebeck effect, and conversely develop a thermal gradient when subject to an electrical potential through the Peltier effect. Devices made from such thermoelectric materials are currently used for refrigeration and heating, and are being widely explored for waste heat recovery.[35] To be effective, these materials must have low electrical resistivities to conduct the charge carriers with minimal loss, and a high Seebeck coefficient to produce sufficient voltages. Additionally they should have minimal lattice thermal conductivity, since the thermal gradient must be maintained. These properties combine in a dimensionless thermoelectric figure of merit zT given by the formula $zT = S^2T/(\rho\kappa)$, where S is the Seebeck coefficient, ρ is the electrical resistivity, and κ the total thermal conductivity, measured at temperature T. In addition to their utility, thermoelectric measurements provide deep insights into the electrical and thermal transport properties of materials, including insight into the underlying band structure.

Oxide materials possess many attractive qualities for waste heat recovery as they are generally light weight materials with the potential for high temperature air stability.[39, 40] However, oxide materials have not reached the level

of performance of current state-of-the-art main group thermoelectrics. This is in part due to higher thermal conductivities compared to other material families, but is additionally a result of low power factors (S^2/ρ). While many oxides possess favorable Seebeck coefficients, finding oxides with the necessary metallic conductivities while retaining these high Seebeck coefficients has proved difficult.[44] Currently, the highest performing oxide materials are p-type complex cobalt oxides which sprung from the discovery of high thermopower in metallic Na_xCoO_2.[41] These compounds possess metallic resistivities yet retain high Seebeck coefficients. A key feature in all of the promising cobalt oxides are CoO_2 layers comprising mixed valent Co^{3+} and Co^{4+}. The highly correlated, mixed valent cobalt ions provide the necessary electrical properties, and the layered structure results in a low thermal conductivity, giving rise to a modestly high thermoelectric performance.

With the promising performance of the complex cobalt oxides, research into the thermoelectric properties of other oxide materials has been of interest. Misfit rhodium oxides have been explored as the 4d analogues of the cobalt oxides and have shown comparable room temperature Seebeck coefficients with metallic conductivities.[45–47] However, the exploration of other 4d metal compounds has been relatively sparse.

Complex oxides of palladium are particularly interesting as many are

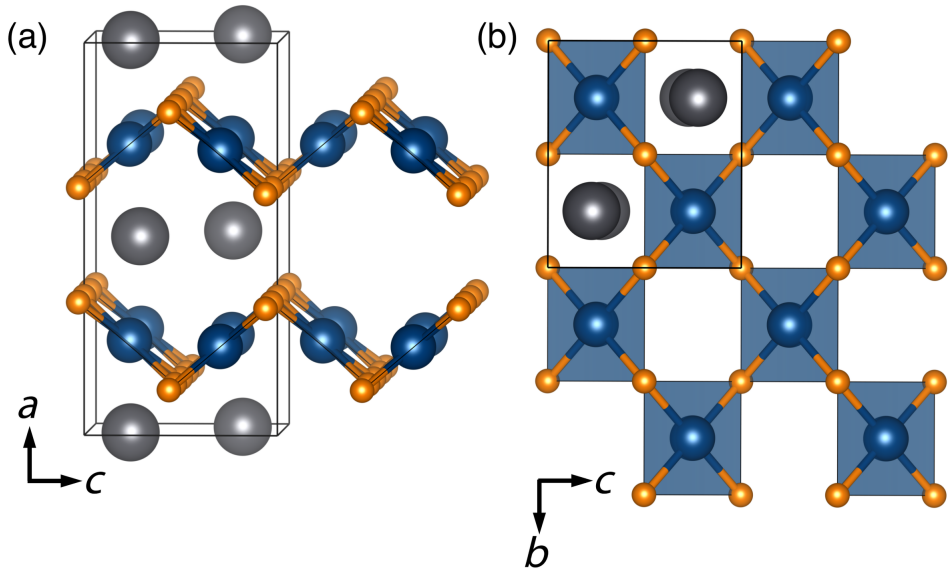

Figure 2.1: Depictions of the orthorhombic $Imma$ (space group #74) crystal structure of $PbPdO_2$. (a) Shows the corrugated layers of corner-connected PdO_4 square planes, arranged in a checkerboard pattern as seen in the top view in (b). Pb atoms (large spheres) are 4-coordinate with O, capping PbO_4 square pyramids between the Pd–O layers.

known to undergo compositionally driven metal-insulator transitions with hole doping,[48, 49] and the transitional regime is often a fertile playground for thermoelectric research. PdO itself is driven metallic with as little as 1 mol % Li substitution.[25] p-type oxide metals starting from non-magnetic parent compounds are relatively uncommon, prompting the investigation of their thermoelectric properties. $PbPdO_2$ is an attractive material for thermoelectric investigation due to its layered nature of Pd square planar units (suggesting potentially lower thermal conductivity) and the possibility for hole doping (suggesting control of electrical properties). $PbPdO_2$, like many other complex palladium oxides, is a small band gap semiconductor. Below 100 K, the resistivity has been reported to display semiconducting behavior *ie.* it increases with decreasing temperature. Above 100 K, the material behaves like a metal with resistivity increasing with temperature.[50] The structure shown in Figure 4.1 consists of layers of Pb atoms, with the lone pairs pointing in the plane, alternating with layers of square planar PdO_4 units. These PdO_4 square planes form a two dimensional tilted checkerboard pattern.[51] $PbPdO_2$ has attracted attention following suggestions from preliminary electronic structure calculations that it could behave potentially as a spin gapless semiconductor with appropriate substitution.[52, 53] More recent calculations using hybrid functionals have pointed to the existence of a small band gap.[54] $PbPdO_2$ has been shown pre-

viously to incorporate Co[55, 56] and Cu[57] onto the Pd site. The small band gap and potential to control electrical properties through aliovalent substitution, coupled with an interesting layered structure, makes it attractive for exploring thermoelectric properties.

Here we report the thermoelectric performance of polycrystalline Li-substituted $PbPdO_2$ at elevated temperatures. Rietveld refinements of neutron diffraction patterns confirm the Li substitution onto the Pd site, with a solubility limit of approximately 4 mol % Li. With Li-substitution, we observe a 10-fold decrease in the resistivity to below the Mott metallic limit without a precipitous drop in the Seebeck coefficient. Metallic conductivities with Seebeck coefficients nearing 200 μV/K at 600 K are remarkable in a non-magnetic oxide material, and points to the need to explore other oxide systems for thermoelectric performance. The experimental results are backed up with density functional theory electronic structure calculations, including calculations of the Seebeck coefficient within Boltzmann transport theory, which suggest that the unusually high power factor is likely to have its origins in the unusual band structure, rather than as a result of spin or charge correlation.

2.2 Methods

Polycrystalline samples of $PbPdO_2$ without and with Li substituting for Pd were prepared by heating stoichiometric amounts of $PbCO_3$, PdO, and Li_2CO_3 powders. The precursors were finely ground using an agate mortar and pestle and pressed into pellets at 100 MPa. The pellets were placed on beds of powder of the same composition to prevent contamination from the alumina crucible. Reactions were carried out at 700 °C for 12 hours. Samples were reground and reheated several times (typically three times) to ensure a complete reaction of the precursors.

Laboratory X-ray diffraction studies were carried out on samples mixed with a silicon standard on a Panalytical Empyrean diffractometer with Cu-K_α radiation. Neutron diffraction studies on samples loaded in vanadium cans at room temperature employed a constant $\lambda = 2.078$ Å wavelength from a Ge-(311) monochromator of the BT-1 neutron powder diffractometer at the National Institute for Standards and Technology (NIST). Neutron powder diffraction was carried out on the stoichiometric and the highest Li-substituted sample. Rietveld[58] refinement was performed using the TOPAS academic software suite.[59] Crystal structures were visualized using VESTA.[60] Prior to the

[0]Certain commercial equipment, instruments, or materials are identified in this document. Such identification does not imply recommendation or endorsement by the National Institute of Standards and Technology nor does it imply that the products identified are necessarily the best.

measurement of physical properties, the resulting powders were compacted into dense pellets using Spark Plasma Sintering (SPS), following details described previously.[61] Densification was carried out at $T = 950\,\mathrm{K}$, as measured by a pyrometer, for 15 minutes under vacuum, with residual Ar flow. Neutron diffraction measurements carried out before and after the SPS treatment did not reveal any significant changes in the structure and composition. Pycnometry measurements conducted on a Micromeritics AccuPyc 1340 Pycnometer confirm sample densities greater than 95% of the theoretical density for all samples. Elemental analysis was performed on the stoichiometric and highest substituted samples by Galbraith Laboratories, Knoxville TN. For the nominal composition $PbPdO_2$, the analysis gave Pb:Pd weight ratio of 60.9%:28.0 (expected 59.9%:30.8%) and for the nominal 8 mol % Li-substituted sample, the analysis gave a Pb:Pd:Li ratio of 59.7%:26.5%:0.168% (expected 61.3%29.0%:0.164%). The Seebeck coefficient and electrical resistivity were measured in a He atmosphere underpressure using an ULVAC Technologies ZEM-3 instrument. Hall coefficients were measured at 11 K using a 4 probe configuration on a Quantum Design Dynacool PPMS. Thermal diffusivity was measured using the laser flash technique between room temperature and 973 K under an air atmosphere on a Netzsch LFA 457 system. Pellets for the measurement, approximately 8 mm in diameter and 2 mm thick, were sprayed with a layer of carbon paint in order to minimize er-

rors in the emissivity. The thermal conductivity was calculated using $\kappa = \alpha C_{\mathrm{p}} \rho$, where α, C_{p}, and ρ are thermal diffusivity, heat capacity, and density, respectively. The Cowan model[62] for determining diffusivity, and the Dulong-Petit molar heat capacity, $C_{\mathrm{p}} = 3R$, were employed.

The electronic structure of unsubstituted $PbPdO_2$ was calculated using density functional theory (DFT) as implemented in the Vienna *ab initio* Simulation Package VASP[63, 64] with projector-augmented wave (PAW) pseudopotentials.[65, 66] A cut-off energy of 500 eV was employed, which is substantially above the requirements for the potentials and scalar-relativistic corrections. For structure optimization and band structure calculations, the Perdew-Burke-Ernzerhof exchange-correlation functional within the generalized gradient approximation (GGA-PBE) was employed.[67] The standard primitive unit cell of the conventional body-centered orthorhombic cell was obtained using AFLOW.[68] A Γ centered k-mesh of $8\times8\times8$ was used for structure optimization. The Brillouin zone paths for band structure calculations were adapted from Setyawan and Curtarolo.[69] Additional calculations of the density of states (DOS) employed the HSE06 screened hybrid functional.[70] Spin-orbit coupling (SOC) can be important for empty Pb^{2+} $6p$ states.[71] Calculations of the band structure with and without spin-orbit coupling verified that valence band states, which are the important consideration here, are not impacted by the exclusion

of SOC. Transport properties were calculated at constant carrier concentration using Boltzmann transport theory in the constant relaxation time approximation. We employed the BOLTZTRAP code[72] based on k-dependent eigenvalues obtained from DFT calculations performed with VASP. Further details of how such calculations were carried out are provided alongside the results of the calculations.

2.3 Results and discussion

2.3.1 Preparation and characterization

Various amounts of Li were substituted into $PbPdO_2$ to study the change in electronic properties. Li^+ was expected to substitute for Pd^{2+} rather than Pb^{2+} because of their similar Shannon-Prewitt ionic radii: 0.590 Å for 4-coordinate Li^+, 0.64 Å for 4-coordinate square planar Pd^{2+}, and 0.98 Å for 4-coordinate Pb^{2+}.[73] Rietveld refinement of neutron diffraction patterns was performed to confirm the location and amount of Li substitution into the structure as Li poorly scatters X-rays. The samples studied here are post-SPS, and represent the materials whose physical properties were measured. Figure 2.2 shows the Rietveld refinements of both (a) the stoichiometric $PbPdO_2$, and (b) the nominally sub-

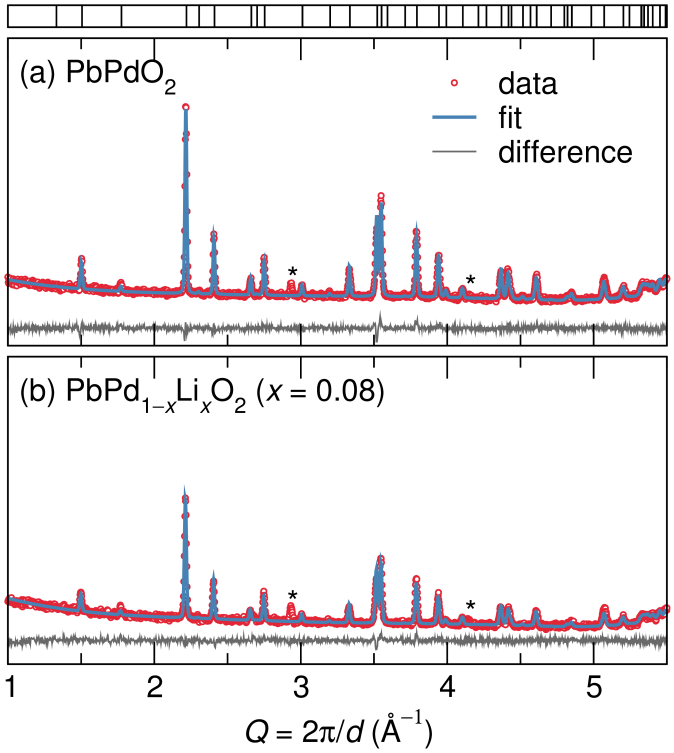

Figure 2.2: Rietveld refinements of neutron diffraction data of (a) pristine $PbPdO_2$ and (b) the nominally 8 mol %-substituted $PbPd_{0.92}Li_{0.08}O_2$, showing the quality of the fits. The top panel indicates the Bragg reflection marks for $PbPdO_2$. Asterisks mark the positions of reflections from the vanadium sample can.

stituted $PbPd_{0.92}Li_{0.08}O_2$; the results of which are summarized in Table 2.1. The Li occupancy on the Pd site for the nominally 8 mol %-substituted sample was determined to be 4.2(9)%. The Pd and Li occupancy was constrained to sum to 1. The excess Li is not observed in neutron diffraction, though elemental analysis matches the nominal Li content. The Li impurity phase is most likely too small to see in diffraction data. Refinements with the Li on the Pb site were conducted, but did not improve the fits, supporting the Li substitution on the Pd site.

In further support for Li substitution for the Pd, the bond valence sums (BVS) for Li on both the Pd and Pb sites were calculated.[74] Li on the Pd site with a Li–O bond distance of 2.029 Å gives a BVS = 0.87. On the Pb site, the Li–O distance is 2.339 Å, giving a BVS = 0.38. While both sites leave Li underbonded, Li on the Pd site is more favored as the BVS is closer to the ideal value of BVS = 1 for Li^+.

For the nominally 8 mol % Li substitution, PbO impurities were observed by diffraction prior to SPS. No PbO phase is observed after SPS possibly due to the reducing atmosphere of the SPS process which can result in Pb being reduced and melted into the graphite die. In addition to densifying the material, SPS appears to introduce approximately 6 % Pb vacancies in the samples, while no oxygen vacancies were observed.

Table 2.1: Structural parameters of $PbPdO_2$ at room temperature, as determined by Rietveld refinement of neutron diffraction data. Orthorhombic space group: $Imma$ (#74) The sites are Pb 4e $(0, \frac{1}{4}, z)$; Pd 4c $(\frac{1}{4}, \frac{1}{4}, \frac{1}{4})$, and O 8$f$$(x, 0, 0)$.

Nominal Composition	$PbPdO_2$	$PbPd_{0.92}Li_{0.08}O_2$
a (Å)	9.4394(4)	9.4358(6)
b (Å)	5.4508(2)	5.4487(3)
c (Å)	4.6514(2)	4.6470(3)
Pb Occupancy	0.94(1)	0.927(9)
Li Occupancy	–	0.042(9)
Pb z Position	0.7751(6)	0.780(7)
O x Position	0.3488(4)	0.3498(5)
Pb U_{iso} (Å^2)	0.010(1)	0.012(1)
Pd/Li U_{iso} (Å^2)	0.005(2)	0.004(2)
O U_{iso} (Å^2)	0.010(1)	0.014(1)
O–O–O (°)	102.5(2)	101.9(3)
R_{wp} (%)	3.9	3.5

The change of the lattice parameters with Li substitution was monitored to further understand structural and compositional changes. Figure 2.3 shows the room temperature resistivity, lattice parameters and unit cell volume as a function of substitution. The room temperature resistivity drops below the Mott metallic limit of $10^{-2}\,\Omega\,\mathrm{cm}$ with as little 2 % Li substitution and only decreases slightly with further substitution. Upon substitution, the a and b lattice parameters remain relatively constant, while the c axis contracts with Li content up to 4 mol % Li. A lattice contraction is expected due to the smaller Li ion as well as the necessary oxidation of Pd^{2+} to Pd^{3+} to maintain neutrality. The c lattice parameter remains constant after 4 % Li substitution, which suggests a solubility limit of Li into the structure further supporting the refined Li occupancy values from neutron diffraction of the nominal 8 mol % sample. This also explains the PbO impurity phase in the higher-substituted samples. The small solubility limit of Li potentially arises from steric resistance to further lattice contraction from the Pb lone pairs, and resistance of Pd to further oxidize.

Ozawa *et al.* have reported that the angle of the Pd square planes can affect the electrical properties.[57] The difference in this angle with Li substitution (O–O–O()$inTable2.1)isonly0.6$. Thus, a slight change in orbital overlap is not likely to significantly affect the electrical properties relative to the increased charge carriers from hole-doping.

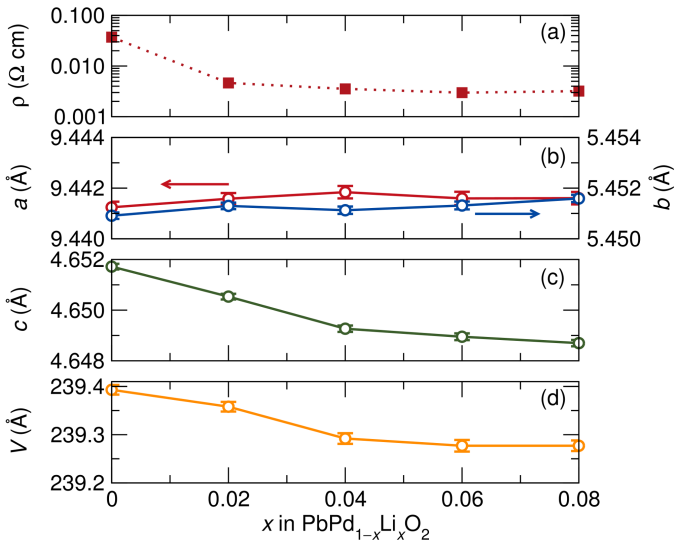

Figure 2.3: Room temperature resistivity, lattice parameter and unit cell volume changes as a function of Li substitution in $PbPdO_2$. Only the c parameter changes significantly up to 4 mol % Li. The constant values above 4 mol % suggest a solubility limit of Li in the structure. Error bars indicate one standard deviation.

2.3.2 Electrical transport and Seebeck coefficient

The electrical properties of $PbPdO_2$ with substitution are shown in Figure 2.4. Stoichiometric $PbPdO_2$ shows a room temperature resistivity of 0.037 Ω cm, which is considerably lower than the 0.75 Ω cm reported by Ozawa and co-workers.[50] The difference can be attributed to the densification of the material through SPS. Upon substitution with 4 mol % Li, the room temperature resistivity drops to 3.5×10^{-3} Ω cm. The Seebeck coefficient is 215 μV/K at room temperature for $PbPdO_2$. This is also substantially higher than previous reports,

possibly due to densification from SPS. It is unusual for both the resistivity and Seebeck coefficient to change favorably, highlighting the importance of dense pellets not only for their robustness, but also for optimal performance. Upon substitution with Li, the Seebeck coefficient drops, but the room temperature value is still greater than 100 μV/K for all substitutions and increases with temperature. Because of instrumental constraints requiring a He atmosphere for sample measurements, it was not possible to reliably measure samples at higher temperatures due to surface reduction. Therefore, peak Seebeck coefficients are not reached for the temperatures measured and approach 200 μV/K at 600 K. However, the materials are stable in air to temperatures of 1000 K at which even higher Seebeck coefficients would be expected.

Hall measurements on the stoichiometric and 8 mol % Li substituted samples suggested carrier concentrations of 1.88×10^{18} cm^{-3} and 3.72×10^{18} cm^{-3} respectively. These concentrations are an order of magnitude higher than the the value of 1.8×10^{17} cm^{-3} reported by Ozawa and co-workers[50] which in turn explains why we observe an order of magnitude difference in resistivity (lower in the samples measured here). It is expected, that given an order of magnitude decrease in the resistivity with Li substitution, we would see a corresponding increase in the carrier concentration. We see only a slight increase.

The resistivity and Seebeck coefficient values obtained for the polycrys-

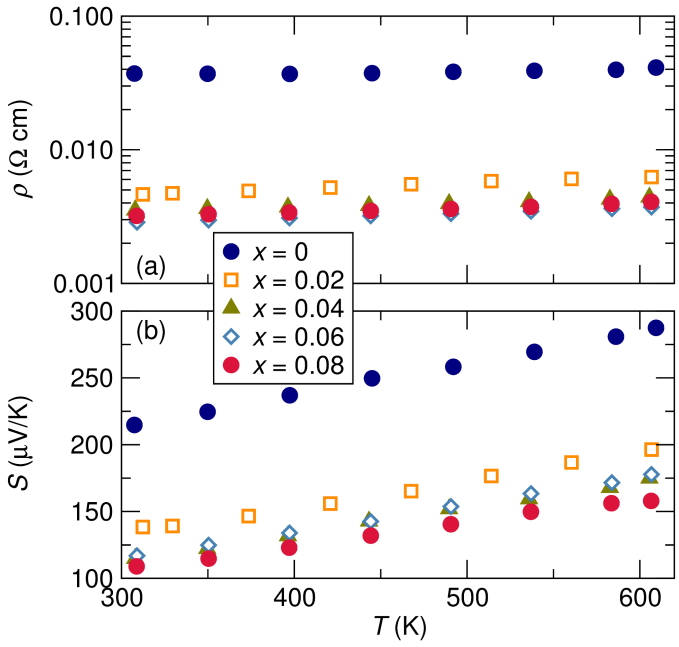

Figure 2.4: (a) Resistivity and (b) Seebeck coefficients for $PbPd_{1-x}Li_xO_2$. The resistivity drops by an order of magnitude with 2 mol % substitution while the Seebeck coefficient drops by 100 μV/K. The Seebeck coefficients of the Li-substituted samples increase with temperature and approach 200 μV/K at 600 K.

talline Li-substituted $PbPdO_2$ materials are almost identical to those of polycrystalline $Na_xCoO_{2-\delta}$, which has a Seebeck coefficient of $100\,\mu$V/K and resistivity of $2\times10^{-3}\,\Omega\,$cm at 300 K.[75] Single crystals of some complex cobalt oxides are the highest performing oxide thermoelectric materials and many different compositions have been explored since the discovery of high thermopower in $NaCoO_2$. [76, 77] Central to the thermoelectric performance of these cobaltate compounds is the high Seebeck coefficient with metallic resistivities. When first observed, the Heikes formula[78] was unable to explain the unexpected thermopower at high temperatures. Koshibae and co-workers proposed a generalized Heikes formula for these compounds which explained the high thermopower at elevated temperatures,[79, 80] by accounting for the spin and orbital degeneracies associated with Co^{3+} and Co^{4+} in various spin states, supported by the observed reduction in the Seebeck with applied magnetic fields.[42] Other explanations point to unique band structures for this class of materials. [81–83]

Interestingly, Li-substituted $PbPdO_2$ consists of almost entirely diamagnetic square-planar, Pd^{2+} except for the small number of holes that dope into the Pd–O conduction band. This implies that the relatively high Seebeck coefficient must arise for reasons distinct from what is observed in the complex cobalt oxides.

2.3.3 Electronic structure and Boltzmann transport analysis

The electronic structure of $PbPdO_2$ was calculated to better understand the electronic properties and is shown in Figure 2.5. The GGA-PBE band structure suggests a semi-metal with the valence band maximum at the Z point and the conduction band minimum at the Γ point. On either side of the valence band maximum are flat regions that then disperse towards peaks at the T and Y points. The presence of both flat and disperse bands just under the Fermi level may explain the high Seebeck coefficient, in conjunction with moderately high mobility in the hole-doped compound. GGA-PBE is known to underestimate the band gap in $PbPbO_2$,[54] and leads to the semimetal prediction. In order to more reliably obtain the expected band gap of the material, hybrid functionals (HSE06) were employed to calculate the DOS.

Hybrid functionals such as HSE06[70], which usually yield more realistic band gaps, were employed to obtain the densities of state of $PbPdO_2$, as shown in Figure 2.6(a). The calculations employed 25% Hartree-Fock exchange. It is seen that the valence band comprises mostly Pd d states and the filled O p states, while the conduction band has components of Pd d and Pb s and p states. Since a dense mesh of k-points are necessary to obtain acceptable accuracy for Boltzmann transport calculations, we did not continue with the computation-

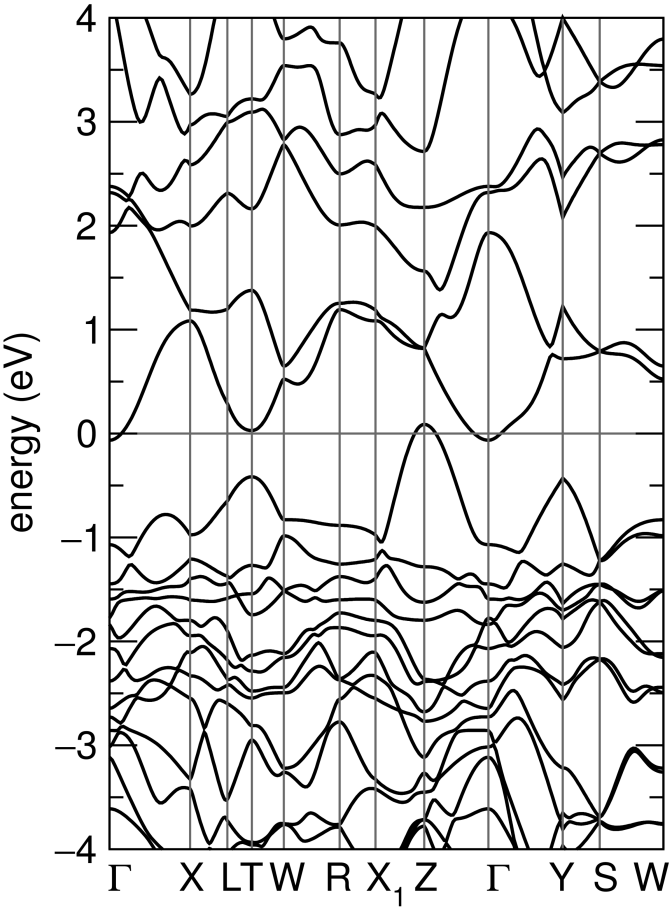

Figure 2.5: Band structure $PbPdO_2$ using the GGA-PBE functional, which predicts a semimetal with regions of flat and disperse bands below the Fermi level.

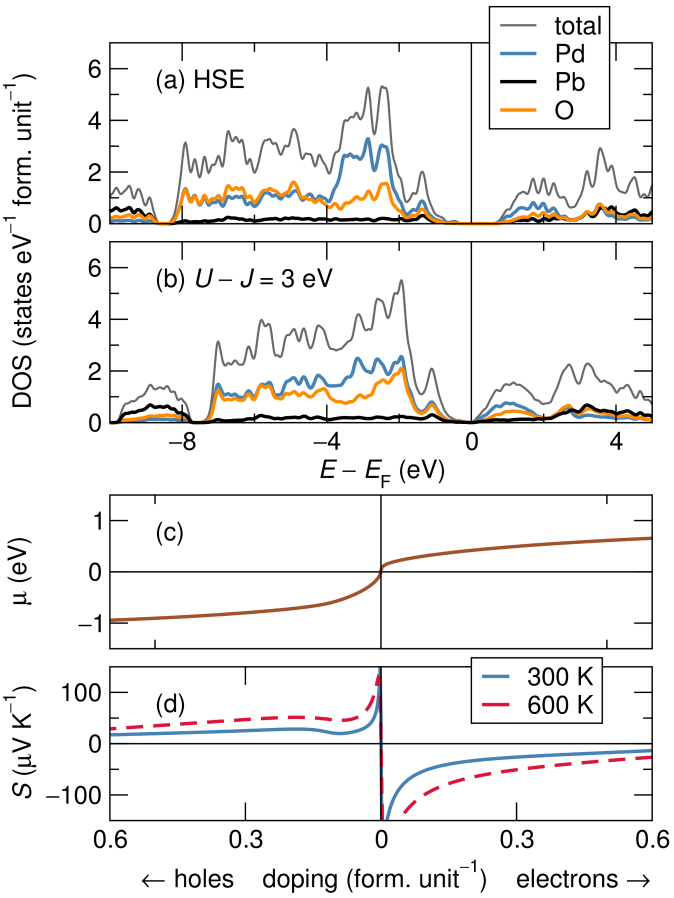

Figure 2.6: Element-resolved electronic density of states of $PbPdO_2$ from (a) HSE06 hybrid functional calculations and (b) GGA + U calculations with U_{eff} = 3 eV. The two bottom panels, (c) and (d) respectively display the chemical potential μ and the trace of the Seebeck coefficient tensor S as a function of doping, as obtained from Boltzmann transport calculations.

ally expensive HSE06 calculations, which were limited to a comparatively small k-point mesh of 83 in the full Brillouin zone. Instead, we used the GGA + U scheme in the rotationally invariant scheme of Dudarev *et al.*,[84] where we invoked a Hubbard U term on the Pd-d states to correct for static correlations, using a value of U between 2.65 eV and 5.65 eV. J was fixed to 0.65 eV in both cases. Calculations of the band structure were carried out with and without SOC (which is computationally expensive) and it was verified that the valence band structure, which is of relevance to the hole-doping studied here, is largely unchanged upon ignoring SOC effects, and SOC was not employed for the transport calculations. The computationally simpler scheme allowed us to employ 31^3 k-points (*ie.* 29791 k-points) in the full Brillouin zone which, in combination with the standard settings for BOLTZTRAP, provided sufficiently converged transport properties in the prior, similar case of $PtCoO_2$.[85] Starting approximately from $U_{eff} = U - J = 3$ eV, a band gap opens that is significantly smaller than the gap obtained with the hybrid functional as seen in Figure 2.6(b). However, the absolute position of the peaks, the overall shape of the DOS, and character and hybridization of states are rather similar for the valence band, for the HSE06 calculation and for the $U_{eff} = U - J = 3$ eV, calculation.

Panels (c) and (d) of Figure 2.6 respectively display the chemical potential μ and the trace of the Seebeck coefficient tensor, as a function of filling in terms of

doping of holes or electrons *per* formula unit, as obtained from the Boltzmann transport calculations. As one removes electrons from $PbPdO_2$ and dopes holes into the valence band, it is seen that the chemical potential does not change very much, even for quite substantial doping [Figure 2.6(c)]. The Seebeck coefficient was seen to be somewhat isotropic, and therefore only the trace of the Seebeck tensor S is displayed here. S is seen to rapidly drop just as one introduces holes into $PbPdO_2$, with the values ranging between 150 μV K^{-1} to 30 μV K^{-1} at 300 K for small hole doping levels. In addition, as seen in the experimental data, that values at 600 K are substantially larger than those at 300 K. The trend and the magnitude of the values encourage the comparison with experiment, and suggest that even simple Boltzmann transport theory captures some of the physics in this system. To ensure that the results presented here are not excessively sensitive to the value of the Hubbard U that was selected, we also performed calculations using $U_{eff} = 5$ eV, and found substantially similar results to the ones found for $U_{eff} = 3$ eV.

2.3.4 Thermal conductivity and thermoelectric figure of merit

The thermal conductivities of stoichiometric $PbPdO_2$ and $PbPd_{0.96}Li_{0.04}O_2$ were measured from room temperature to 973 K. At the highest measured tem-

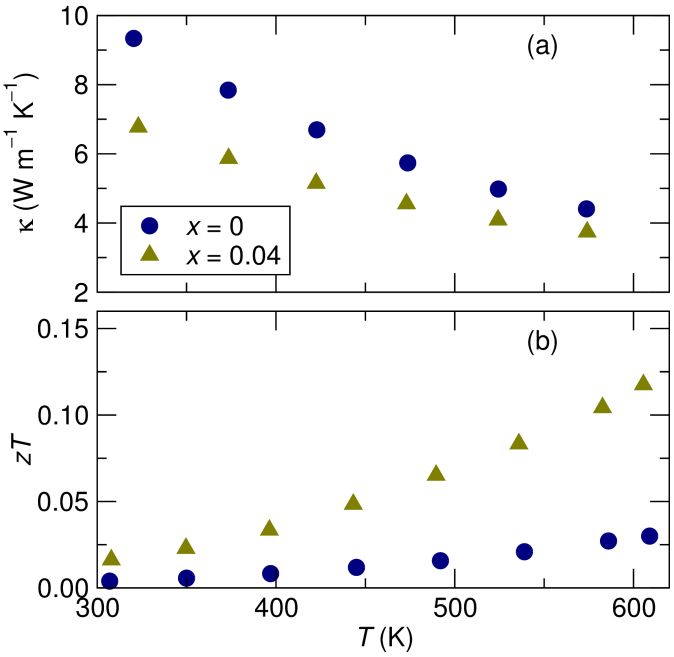

Figure 2.7: (a) Thermal conductivity and (b) zT of $PbPd_{1-x}Li_xO_2$ samples obtained from the electrical and thermal transport measurements. The thermal conductivity of $4\,W\,m^{-1}\,K^{-1}$ gives Li-substituted $PbPdO_2$ a $zT = 0.12$ at 600 K. Higher zT values are anticipated as the temperature is further increased.

perature of 973 K, the values for both samples approach 2.5 W m^{-1} K^{-1}. Low thermal conductivity is expected from the crystal structure, which consists of a layered arrangement of heavy Pb atoms, and potentially, lattice anharmonicity due to the lone pairs in an asymmetric coordination environment.[86] However, the measured values of the thermal conductivity are somewhat high for an effective thermoelectric. Applying the Wiedemann-Franz law, $\kappa_{el} = LT/\rho$, where κ_{el} is the electronic contribution to thermal conductivity and L is 2.44$\times$10^{-8} W Ω K^{-2}, we obtain a κ_{el} of about 0.36 W m^{-1} K^{-1} for the Li-substituted sample at the highest temperature, leading to lattice thermal conductivities just greater than 2 W m^{-1} K^{-1}. For example, at temperatures near 700 K, widely used thermoelectrics have values of lattice thermal conductivity below 1 W m^{-1} K^{-1}.[44] The thermal conductivity can be combined with the electrical properties to give the thermoelectric figure of merit, $zT = S^2T/(\rho\kappa)$. Figure 2.7 shows the measured thermal conductivity and the resulting zT. The Li-substituted sample of $PbPdO_2$ has a $zT = 0.12$ at 600 K. It is clear that the peak zT has not been reached and electrical measurements to higher temperature would yield even higher zT values due to smaller thermal conductivities and larger Seebeck coefficients. In addition, single crystals of Li-substituted $PbPdO_2$ could show markedly decreased resistivities similar to what is seen in Na_xCoO_2 in which the resistivity at 800 K drops from 3.6$\times$10^{-3} Ω cm to 5.2$\times$10^{-4} Ω cm [75], without signifi-

cant effects on the Seebeck coefficient or thermal conductivity, and therefore yet higher values of zT.

2.4 Conclusion

Li has been substituted for Pd in $PbPdO_2$, corresponding to hole doping. The Li substitution site and level of substitution have been established through Rietveld refinement of neutron diffraction data. The substitution limit appears to be close to 4 mol % Li substitution, beyond which evidence for further substitution is not observed. Metallic resistivities are reached with as little as 2 % Li substitution for Pd. The Seebeck coefficient of the substituted samples remains high, at $>$100 μV/K at room temperature and approaches 200 μV/K at 600 K. Despite the relatively high lattice thermal conductivity of the compound, a zT = 0.12 is measured at 600 K. Similar electrical properties are observed in the high performing complex cobalt oxide compounds, arising from spin and orbital degeneracy, which are not present in Li-substituted $PbPdO_2$. Our findings suggest potentially new avenues to achieving high performing oxide thermoelectric materials, and encourage the search for such properties in oxides of more earth-abundant metals than the ones studied here.

Chapter 3

Hole Doping in $LiBiPd_2O_4$ through Li^{1+} and Pb^{2+} Substitution

$LiBiPd_2O_4$ is a band semiconductor structurally analogous to $PbPdO_2$ with half of the Pb^{2+} replaced by Li^{1+} and half by Bi^{3+}. We establish that as in $PbPdO_2$, $LiBiPd_2O_4$ can successfully be hole-doped through Li substitution for Pd and also through Pb substitution for Bi. Both avenues of hole doping are observed to decrease the electrical resistivity by over three orders of magnitude, decreasing from $10^5\,\Omega$cm to $100\,\Omega$cm. The electrical resistivity of hole-doped $LiBiPd_2O_4$ is four orders of magnitude higher than that of hole-doped $PbPdO_2$ precluding its study of further thermoelectric properties. Electronic structure

[1] Michael Knight and Ram Seshadri have contributed to the contents of this chapter.

calculations show that a larger band gap caused by the change in connectivity of the Pd square planar units is the reason for the increased resistivity. ^{7}Li NMR has been used to study the successive hole doping in $LiBi_{1-x}Pb_xPd_2O_4$ $0 \leq x \leq 0.2$. One Li environment is observed in $LiBiPd_2O_4$ as expected due to the one crystallographic Li site. Upon Pb substitution, up to 5 distinct Li environments are observed. These new environments may imply an asymmetric distribution of Pb atoms or the emergence of small, more metallic, regions in a matrix of insulating material.

3.1 Introduction

In light of the favorable thermoelectric performance of Li-substituted $PbPdO_2$ discussed in the prior Chapter, an effort was conducted to explore other complex palladium oxides for high temperature thermoelectric applications. Li-substituted $PbPdO_2$ possessed a 2D layered arrangement of the corner connected Pd square planes. Pb atoms separated the Pd layers. The electrical resistivity and Seebeck coefficient matched almost identically to $NaCoO_2$ which is the prototypical oxide thermoelectric material. The origin of this high performance in $NaCoO_2$ is believed to arise from the spin degeneracy of the Co atoms. Consisting almost entirely of diamagnetic Pd^{2+}, the electrical performance of Li-

substituted $PbPdO_2$ likely arises from other mechanisms.

$LiBiPd_2O_4$, first prepared by Laligant *et al.*, [87] was identified as a structurally similar material to $PbPdO_2$ and thus likely to exhibit similar thermoelectric properties. The crystal structure of $LiBiPd_2O_4$ and its relation to $PbPdO_2$ is given in Figure 3.1. $LiBiPd_2O_4$ can be related to $PbPdO_2$ by replacing half of the Pb^{2+} ions with Li^{1+} and half with Bi^{3+}. Like $PbPdO_2$, $LiBiPd_2O_4$ consists of 2D layers of corner connected Pd square planes. However, they are canted differently due to the differing ionic radii of the Li and Bi atoms which reside between the layers. The presence of layered Pd square planes and a heavy atom with a lone pair of s-electrons suggest that the thermoelectric performance of these two materials may be similar.

$LiBiPd_2O_4$ is also attractive to study due to the multiple possible avenues to achieve hole-doping and the presence of Li, a preferable nucleus for NMR, in large quantities. In this study, hole-doping has been achieved though Pb^{2+} substitution onto the Bi^{3+} site which has been shown to decrease the resistivity in Bi_2PdO_4. [88] As in $PbPdO_2$, hole-doping has also been achieved by Li^+ substitution onto the Pd^{2+} site. ^{7}Li solid state NMR shows only one Li environment in $LiBiPd_2O_4$ as expected, but many distinct Li environments arise with Pb substitution. Both Li and Pb substitution decrease the electrical resistivity by over 3 orders of magnitude, but it does not go through an insulator-metal transition,

remaining too resistive for thermoelectric applications. Calculations of the electronic structure reveal a large indirect band gap which prevents the transition. Changes in orbital overlap of the palladium square planes are likely the cause of the increased resistivity in $LiBiPd_2O_4$ compared to $PbPdO_2$.

3.2 Experimental and Computational Methods

Polycrystalline samples of $LiBiPd_2O_4$, $Li_{1.1}BiPd_{1.9}O_4$ and $LiBi_{1-x}Pb_xPd_2O_4$ $0 \leq x \leq 0.2$, were prepared by heating stoichiometric amounts of Li_2CO_3, Bi_2O_3, PdO, and $PbCO_3$ powders. The precursors were ground in an agate mortar and pestle and pressed into a pellet at 100 MPa. The pellets were placed onto beds of powder of the same composition to prevent contamination from the alumina crucible. The samples were heated at 700 °C for 12 hours in a box furnace. This procedure was repeated twice to ensure a complete reaction of the precursors.

The crystal structures were characterized by X-ray powder diffraction on a Panalytical Empyrean powder diffractometer with Cu-K_α radiation. Rietveld[58] refinement was performed using the TOPAS academic software.[89] Crystal structures were visualized using VESTA.[60] For electrical resistivity measurements, the materials were sintered as bar pellets approximately 9 mm in length and four copper wires were attached with a silver paste

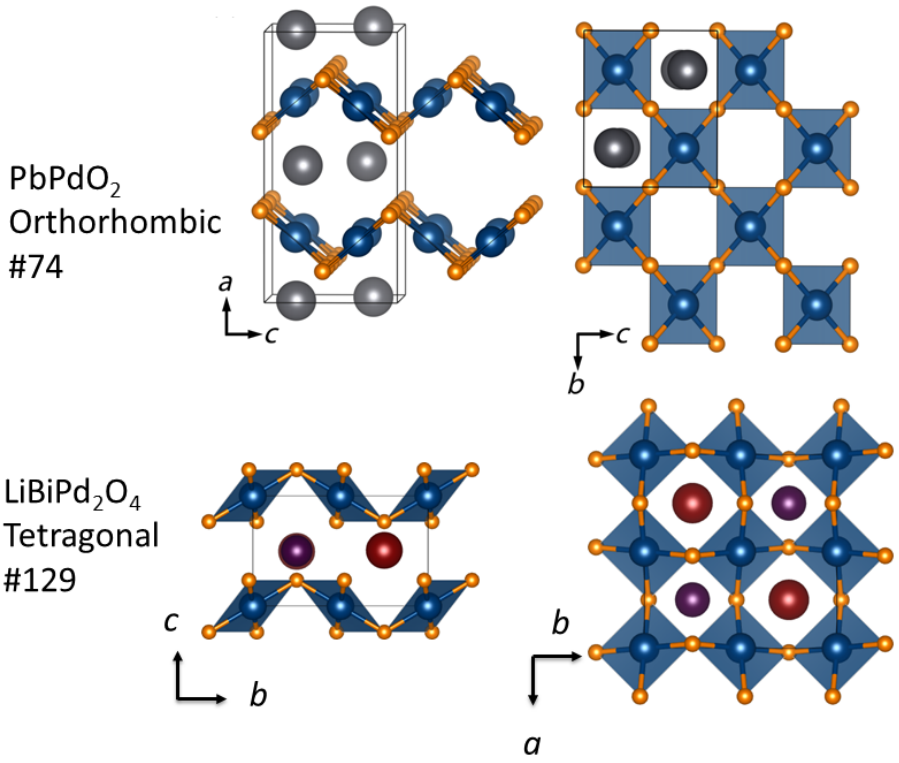

Figure 3.1: Crystal Structure of (top) $PbPdO_2$ compared to (bottom) $LiBiPd_2O_4$ Pb, Pd, O, Li, and Bi are colored silver, blue, orange, purple, and red respectively. In both structures, the PdO square planes corner connect in 2D layers. The differing size of the Li and Bi in $LiBiPd_2O_4$ cause the layers to cant slightly.

before running them in a He refrigerator from 300 K to 25 K. Single pulse ^{7}Li solid-state magic angle spinning (MAS) NMR experiments were performed at 300 K on a Bruker500 MHz spectrometer. Samples were packed into a 4 mm zirconia rotor with Kel-F caps and spun at a rate of 10 kHz. The electronic structure was calculated using density functional theory (DFT) as implemented in the Vienna *ab initio* Simulation Package (VASP)[63, 64] with projector-augmented wave (PAW) pseudopotentials.[66] For structure optimization, the exchange-correlation was described by Perdew-Burke-Ernzerhof within the generalized gradient approximation (GGA-PBE)[67] using a Γ center k-mesh of $8\times8\times8$ and a tetrahedron smearing method.

3.3 Results and discussion

$LiBiPd_2O_4$ crystallizes in the tetragonal space group P4/nmm (129). The layered arrangement of the Pd square planes are canted to allow the lone pair of the Bi atoms to point along the c axis towards the Pd square planes. This is in contrast to $PbPdO_2$ in which the lone pair of the Pb atom are directed between the layers. Polycrystalline $LiBiPd_2O_4$ was prepared through a solid state reaction at 700 °C. Up to 20 mol% Pb was found to substitute onto the Bi site before impurities were observed in the XRD patterns. Excess Li substitution onto the Pd

site corresponding to a formula of $Li_{1.1}BiPd_{1.9}O_4$ was also confirmed to be phase pure through XRD. A representative Rietveld refinement of $LiBi_{0.9}Pb_{0.10}Pd_2O_4$ is shown in Figure 3.2. Due to the near identical scattering strength of Pb and Bi for X-rays, site occupancy refinements could not confirm substitution.

The change in lattice parameters with increasing Pb substitution is presented in Figure 3.3. The a lattice parameter decreases slightly with increasing Pb substitution from 6.9034 Å to 6.9022 Å. The c parameter decreases by a larger amount, from 4.3552 Å to 4.3500 Å. The decrease is expected due to the slightly smaller ionic radius of Pb^{2+} compared to Bi^{3+} as well as the necessary oxidation of Pd^{2+} to Pd^{3+} to maintain charge neutrality. It is of note that the c lattice parameter decreases by a greater amount compared to the a lattice parameter. The decreasing c lattice parameter corresponds to lowering the distance between the Pd square plane layers. The substitution does little to change the orientation or configuration of the square planes themselves. The successive decrease in lattice parameter and phase purity is strong, albeit indirect, evidence that the Pb substitution is successfully substituting onto the Bi site in the lattice.

As mentioned in the introduction, ^{7}Li represents an ideal NMR nucleus to monitor any potential insulator-metal transition in these materials. ^{7}Li is a quadrupolar spin 3/2 nucleus, though the symmetrical tetrahedral coordination of the Li atoms should minimize quadrupolar splitting. Li is present in

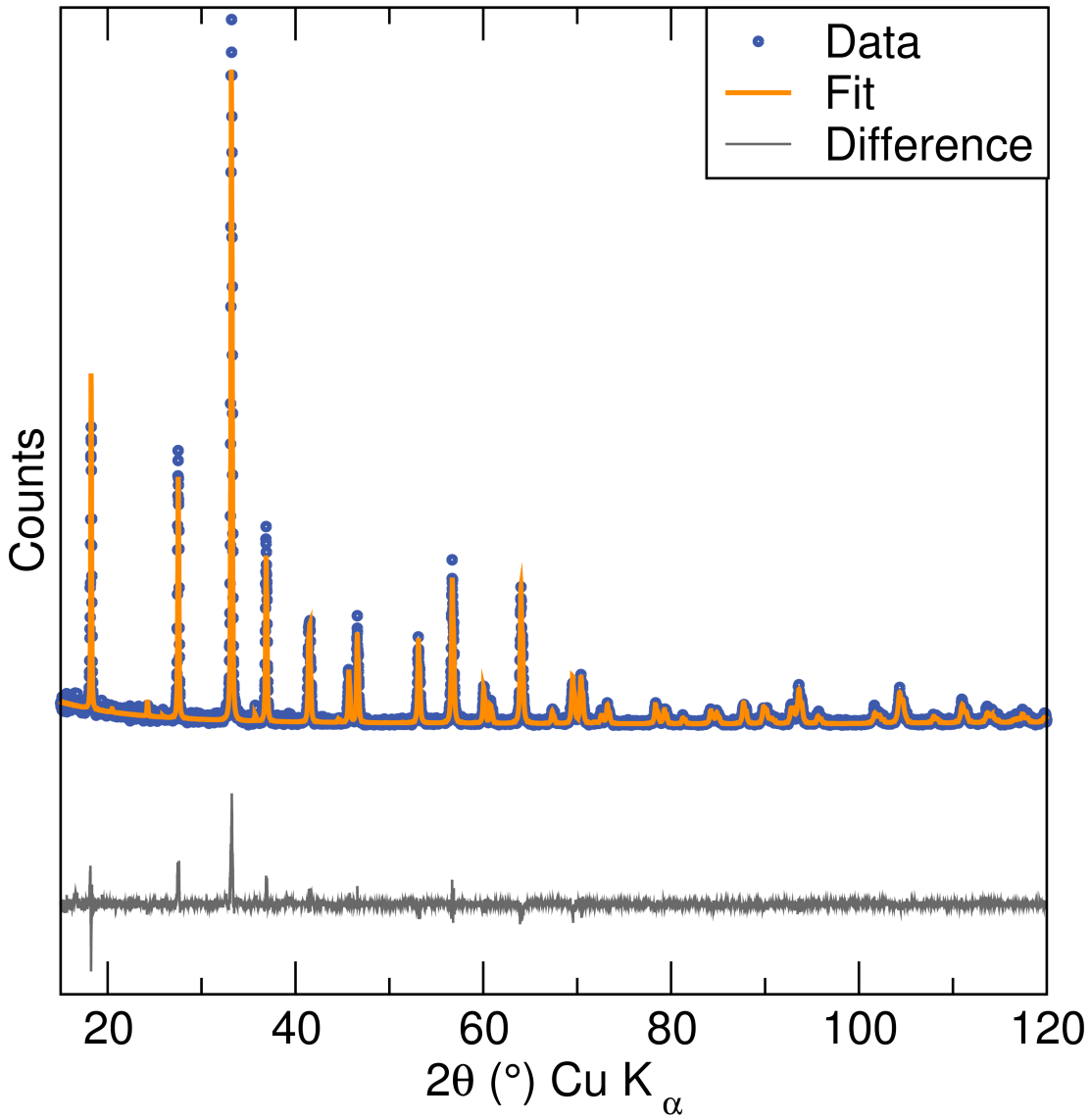

Figure 3.2: Rietveld refinement of laboratory X-ray diffraction data of $LiBi_{0.9}Pb_{0.1}Pd_2O_4$.

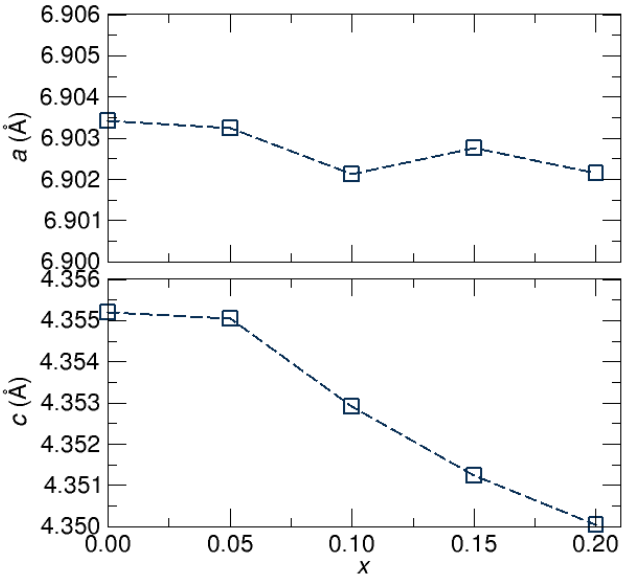

Figure 3.3: Variation of lattice parameters in $LiBi_{1-x}Pb_xPd_2O_4$.

high abundance before any substitution occurs and successive changes in the NMR spectrum can be observed with hole doping with the aim to better understand any potential metallic transition in these and related materials. Figure 3.4 shows representative spectra of the Li_2CO_3 precursor, pristine $LiBiPd_2O_4$, $LiB_{0.9}Pb_{0.1}Pd_2O_4$, and $Li_{1.10}BiPd_{1.9}O_4$.

As expected, $LiBiPd_2O_4$ shows one distinct Li environment at -2.6ppm, slightly shifted upfield from the Li_2CO_3 precursor. The peak does not show any evidence of a quadrupolar lineshape owing to the tetrahedral coordination of the Li ion. Differences in peak shape between $LiBiPd_2O_4$ and Li_2CO_3 may be due to varying relaxation rates between the two materials. Of particular note is the observed spectrum of $LiB_{0.9}Pb_{0.1}Pd_2O_4$. With Pb substitution, at least 5 new, distinct Li environments are observed. The details and evolution of these peaks will be discussed in detail.

Finally, the ^{7}Li spectrum of $Li_{1.10}BiPd_{1.9}O_4$ does not show any appreciable difference from $LiBiPd_2O_4$. There is a slight tail to higher ppm which may be from a new Li environment or a slight amount of Li_2CO_3 precursor. One would expect a significant fraction of at least one new Li environment to be observed in this spectrum which would arise from Li in a square planar coordination. As evidenced in the resistivity measurements to be discussed, Li substitution for Pd results in a drastic drop in the electrical resistivity. If small regions in the ma-

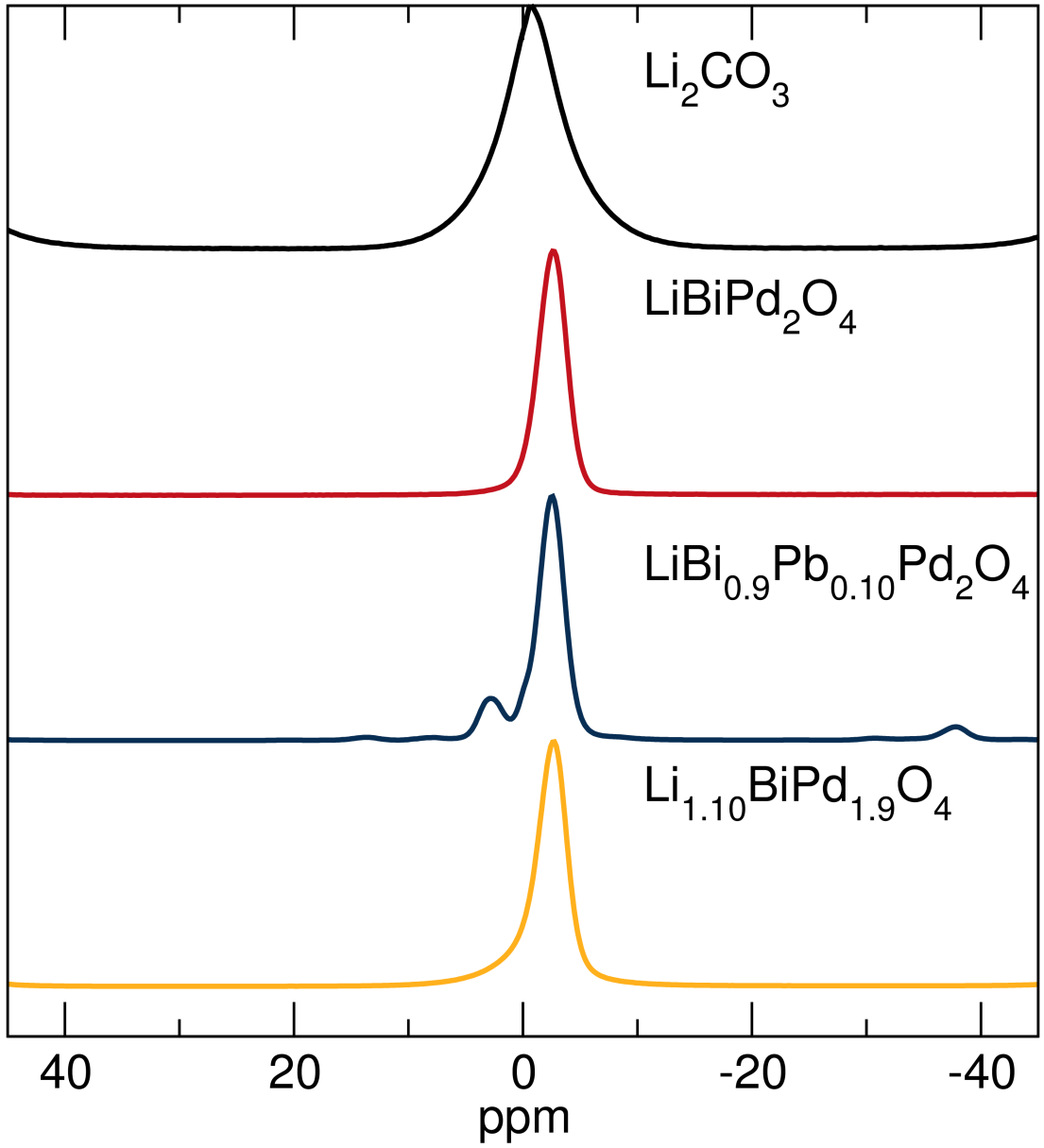

Figure 3.4: ^{7}Li solid state MAS NMR of Li_2CO_3, $LiBiPd_2O_4$, $LiBi_{0.9}Pb_{0.1}Pd_2O_4$, and $Li_{1.1}BiPd_{1.9}O_4$. Numerous new Li environments are evident in $LiBi_{0.9}Pb_{0.1}Pd_2O_4$, while only one Li environment is observed in $Li_{1.1}BiPd_{1.9}O_4$.

terial begin to exhibit metallic behavior, as believed to happen in $CaPd_3O_4$ and $SrPd_3O_4$, [90] the lack of an observable, new Li environment can be explained. It is likely, a combination of the Knight shift as well has the lower symmetry of the square planar coordination has significantly broadened and/or shifted the Li signal. Extended frequency ranges were explored with increased collection times, but a broad signal was not observed.

The evolution of the NMR spectra with increasing Pb substitution is given in Figure 3.5. All peaks are scaled by the intensity of the main signal in $LiBiPd_2O_4$. With Pb substitution, 5 new Li environments are evident. These new Li environments are surprising as the materials are phase pure according to XRD, and thus suggest there are structural complexities with hole doping. From peak integration, we see the most intense peak that emerges with Pb substitution comprises 25% of the Li environments at the highest level of Pb substitution. Thus, we do not believe its origin is that of a Li_2O impurity, which also possesses a shift around 3 ppm. XRD diffraction may not reveal small amounts of impurities composed of light elements like Li and O, but would certainly show an impurity phase if 25% of the Bi/Pb had not reacted with the Li precursor. It is of note that the 3 environments upfield from the main signal (shoulder at -7 ppm, small peak at -32 ppm, and slightly larger peak at -38ppm) all saturate at a x=0.15 and do not grow relatively larger when x=0.20. The 2 environments downfield

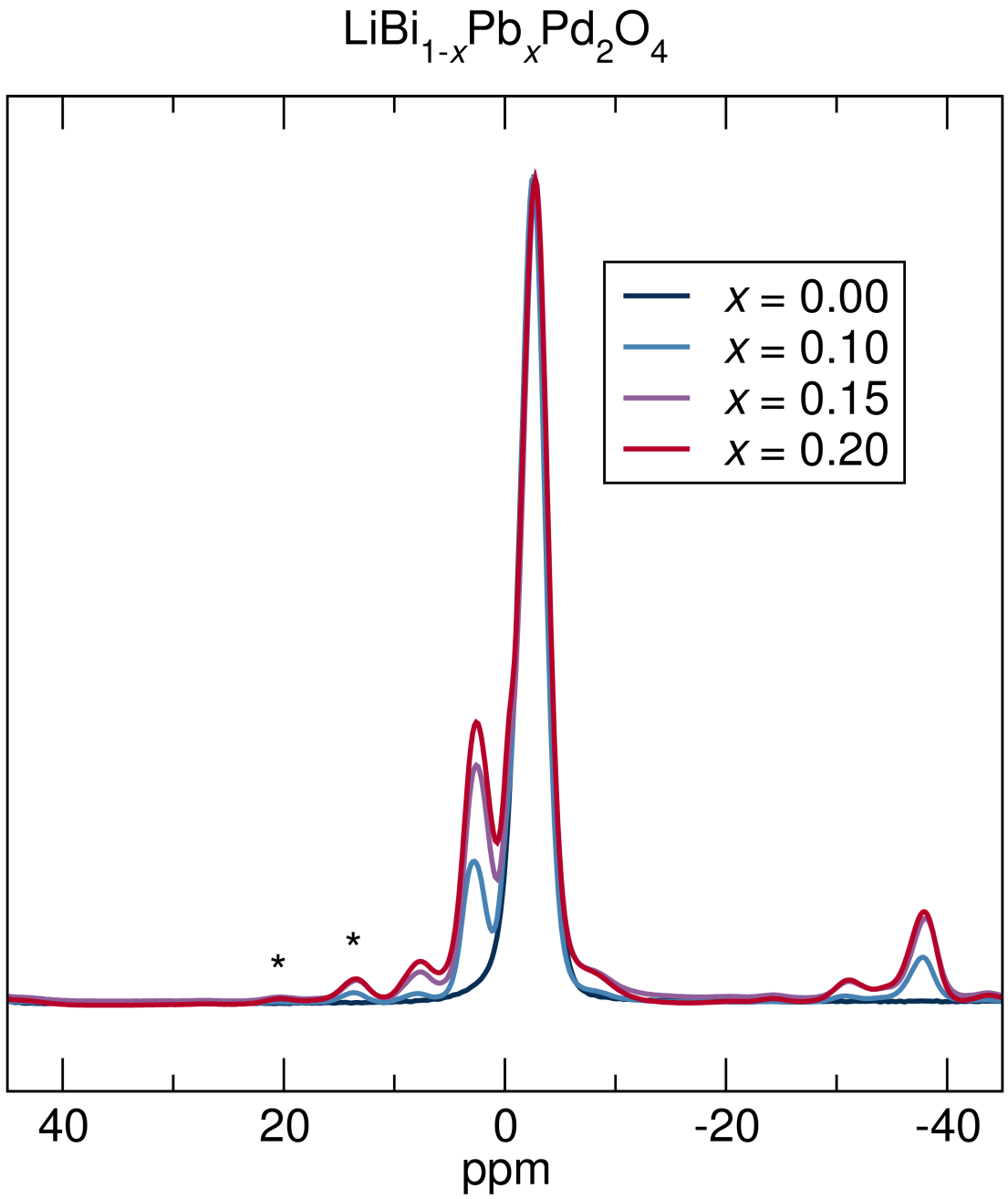

Figure 3.5: ^{7}Li solid state MAS NMR of $LiBi_{1-x}Pb_xPd_2O_4$. At least 5 new Li environments are observed with Pb substitution that grow relative to the signal from pristine $LiBiPd_2O_4$. Asterisk denotes spinning sidebands from the 10 kHz spinning speed.

(large peak at 3 ppm, smaller peak at 8 pmm) continue to grow relative to the main signal up through x=0.20.

The Knight shift in Li based metals has been reported to shift the signal up to 250 ppm for Li metal, [91, 92] though materials with fewer Li-s states near the Fermi level can show much less of a shift. Li-Sn alloys can have Li chemical shifts ranging from 6 ppm to 80 ppm.[93] As will be shown through electrical transport measurements, $LiBiPd_2O_2$ is insulating, though the resistivity drops by three orders of magnitude with Pb substitution. It may be then that the new Li environments correspond to more conductive regions of material through the Knight shift or hyperfine splitting from the necessary Pd^{3+} atoms. An asymmetric distribution of the Pb atoms, through for example dopant clustering, may also give rise to the multiple signals observed.

The electrical resistivity of pristine and hole-doped $LiBiPd_2O_4$ is given in Figure 3.6. Pristine $LiBiPd_2O_4$ is insulating with a resistivity on the order of $10^5 \Omega$ cm. The resistivity does not appreciably change with 10 mol% Pb substitution. With successive substitution the resistivity drops by 3 orders of magnitude to 100Ω cm. Interestingly, when excess Li is used to substitute onto the Pd site in $Li_{1.05}BiPd_{1.95}O_4$, the resistivity is even lower than $LiBi_{0.8}Pb_{0.2}Pd_2O_4$. Nominally, this Pd substitution levels corresponds to 4 times as many holes doped into the material over the Li substitution. This is consistent with our previous works in

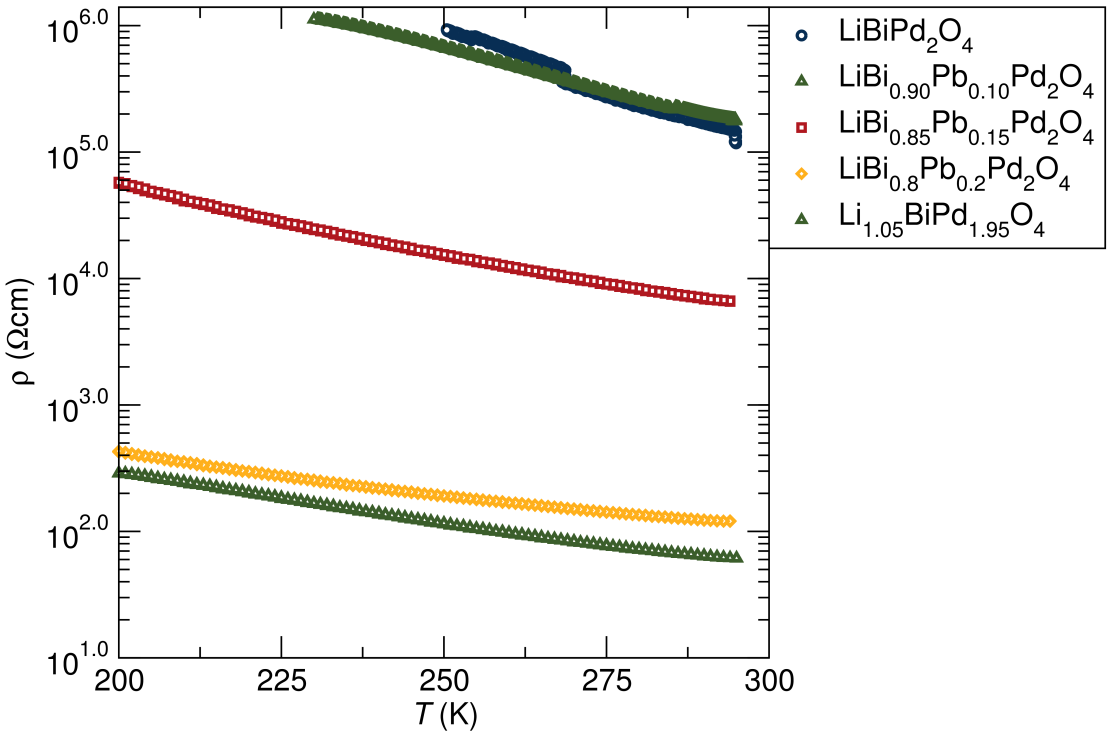

Figure 3.6: Electrical resistivity of pristine $LiBiPd_2O_4$ and hole-doped through Li or Pb substitution. A larger amount of Pb substitution is needed to get a comparable drop in resistivity as Li substitution.

which Li substitution for Pd in $PbPdO_2$ drove an insulator-metal transition with as little as 2 mol% substitution,[43] where as roughly 15 mol% Na substitution for Ca was needed to drive a transition in $CaPd_3O_4$.[90] Substituting onto the Pd site likely results in more mobile carriers as the top of the valence band in these complex palladium oxides consists mostly of Pd-d and O-p states.

Despite the large decrease in resistivity with hole-doping, the materials remain much too resistive for thermoelectric applications in which resistivities $<0.01\Omega$ cm are necessary. It is prudent then to discuss the physical and electronic structure differences between $LiBiPd_2O_4$ and $PbPdO_2$ which we have shown to exhibit favorable electrical properties for thermoelectric applications. [43] Figure 3.7 shows the electronic band structure calculated through DFT. $LiBiPd_2O_4$ is an indirect band gap semiconductor, like $PbPdO_2$, though it possesses a much larger band gap. The PBE functional, which is known to underestimate band gaps in these materials, predicts a band gap of 1 eV. $PbPdO_2$ is predicted to be a semimetal using the PBE functional. As the DOS show the states at the top of the valence band to be comprised of Pd-d and O-p states, it can be concluded that the differing angles of the Pd square planes result in the increased electrical resistivity. Decreased orbital overlap, particularly of the d_{z^2} orbital which has been predicted to lead to good conductivity, [94] leads to the larger band gap and makes conduction more difficult. Hole-doping is success-

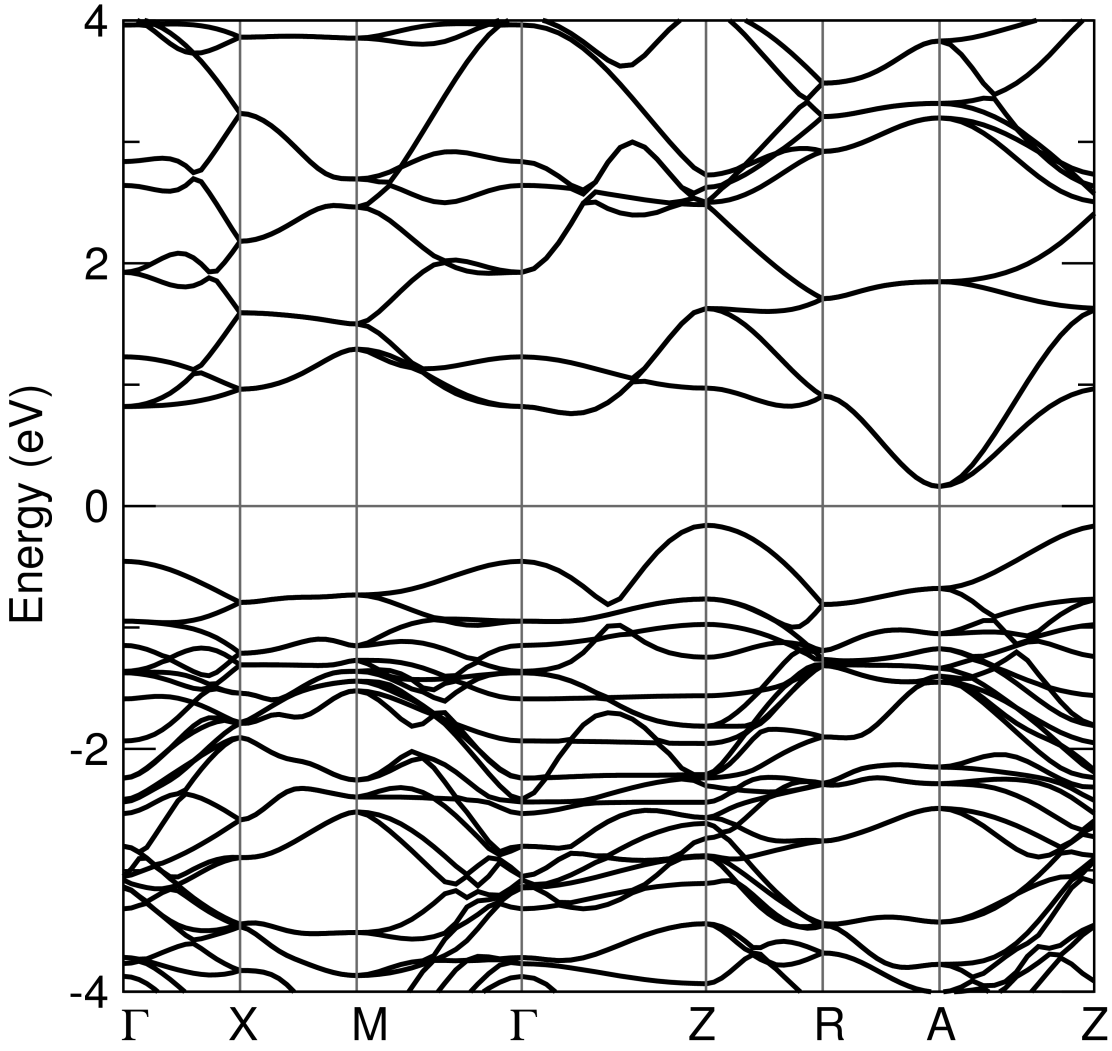

Figure 3.7: Electronic band structure of $LiBiPd_2O_4$.

ful in $LiBiPd_2O_4$ as seen through the decrease in resistivity, and ^{7}Li NMR shows features that are similar to materials that do undergo an insulator-metal transition. Structural modifications that increase the orbital overlap of the Pd square planes would likely lead to increased conduction and a complete insulator-metal transition as seen in $PbPdO_2$.

3.4 Conclusions

$LiBiPd_2O_4$ has been prepared and successfully hole-doped through Li substitution onto the Pd site or through Pb substitution for Bi. Despite only one crystallographic Li site, ^{7}Li NMR of $LiBi_{1-x}Pb_xPd_2O_4$ displays at least 5 unique Li environments. Differing distributions of the Pb dopant along with a Knight shift- like effect, may account for these observations. Despite a decrease in resistivity of over three orders of magnitude, the hole-doped material remains insulating and does not transition to a metal as seen in other complex palladium oxides. A large band gap owing to decreased orbital overlap of the Pd-d orbitals and O-p orbitals likely lead to more insulating behavior. This work highlights the importance of structural considerations when exploring new functionality in materials, and the potential for local probes such as NMR in understanding transition mechanisms with chemical substitutions.

Chapter 4

The Role of Structural and Compositional Heterogeneities in the Insulator-to-Metal Transition in Hole-Doped APd$_3$O$_4$ (A = Ca, Sr)

The cubic semiconducting compounds APd$_3$O$_4$ (A = Ca, Sr) can be hole-doped by Na substitution on the A site and driven towards more conducting

[1]The contents of this chapter have substantially appeared in Reference [90]. Reproduced with permission from: L. K. Lamontagne, G. Laurita, M. Knight, H. Yusuf, J. Hu, R. Seshadri, K. Page, The Role of Structural and Compositional Heterogeneities in the Insulator-to-Metal Transition in Hole-Doped APd$_3$O$_4$ (A = Ca, Sr) *Inorg. Chem.* **56** (2017) 5158–5164. Copyright 2017 American Chemical Society.

states. This process has been followed here by a number of experimental techniques in order to understand the evolution of electronic properties. While an insulator-to-metal transition is observed in $Ca_{1-x}Na_xPd_3O_4$ for $x \geq 0.15$, bulk metallic behavior is not observed for $Sr_{1-x}Na_xPd_3O_4$ up to $x = 0.20$. Given the very similar crystal and (calculated) electronic structures of the two materials, the distinct behavior is a matter of interest. We present evidence of local disorder in the *A* = Sr materials through the analysis of the neutron pair distribution function which is potentially at the heart of the distinct behavior. Solid-state ^{23}Na nuclear magnetic resonance studies additionally suggest a percolative insulator-to-metal transition mechanism wherein presumably small regions with a signal resembling metallic $NaPd_3O_4$ form almost immediately upon Na substitution, and this signal grows monotonically with substitution. Some signatures of increased local disorder and a propensity for Na clustering are seen in the *A* = Sr compounds.

4.1 Introduction

The study of insulator-to-metal transitions is an important topic in the fields of materials chemistry and condensed-matter physics. The profound change in properties associated with the transition are of great fundamental interest,

even at the level of separating the elements into metals and non-metals.[26] In addition, a huge range of useful materials functionalities are often found associated with materials that display such transitions.[27, 28] In particular, understanding compositionally driven insulator-to-metal transitions in which carriers are doped into a material can lead to tuned carrier concentrations for optimal electrical properties in thermoelectric materials[35] or elevated T_c in superconductors.[34] An important question regarding the nature of the transition driven by charge carrier doping into semiconducting or insulating hosts is whether the transition is percolative (in the sense of forming as puddles of metal in the insulating background that coalesce at some concentration and drive the entire system metallic), or whether it occurs suddenly across the entirety of the material. Percolation of metallic regions is believed to lead to the colossal magnetoresistance observed in $LaMnO_3$, [95–97] and leads to interesting magnetic and electronic properties in Sr substituted $La_{1-x}Sr_xCoO_3$. [98–101] While the change in carrier concentration can be estimated based on the amount of doping, there are other considerations that can affect the onset of an insulator-to-metal transition. The size of the dopant ion relative to the crystallographic site, as well as complimentary changes in valence to maintain neutrality can impart local distortions that can also affect an insulator-to-metal transition.[102]

Many complex palladium oxides have been previously shown to un-

dergo compositional insulator-to-metal transitions.[25, 48–50, 103] The small bandgaps and significant Pd-d states just below the Fermi level in complex palladium oxides allows for the ease of hole-doping. Previous studies have suggested that some palladium oxides may have unique gapless electronic structures that can lead to interesting physics[52, 104], though these results may be influenced by the tendency of some DFT functionals to underestimate bandgaps in small bandgap semiconductors. [54] Furthermore, complex palladium oxides are typically diamagnetic, allowing for more detailed studies of local structural changes throughout insulator-to-metal transitions with the use of solid-state NMR, which, while useful in examining local phase separation, is difficult to utilize in magnetic oxide materials. [105, 106] Recently, we have observed a high Seebeck coefficient with metallic conductivity in the complex palladium oxide $PbPdO_2$ when it undergoes an insulator-to-metal transition with Li-substitution. [43]. A better understanding of the insulator-to-metal transitions can lead to improvements in the functional properties of these and other oxide materials.

$CaPd_3O_4$ and $SrPd_3O_4$ both crystallize in the cubic $NaPt_3O_4$ structure type, highlighted in Figure 4.1. The alkaline-earth cation resides in an 8-coordinate cubic site, while the d^8 palladium is in its preferred square-planar coordination. The palladium square planes are corner-connected and form a 3D network throughout the crystal.[107] Given the identical crystal structures, one

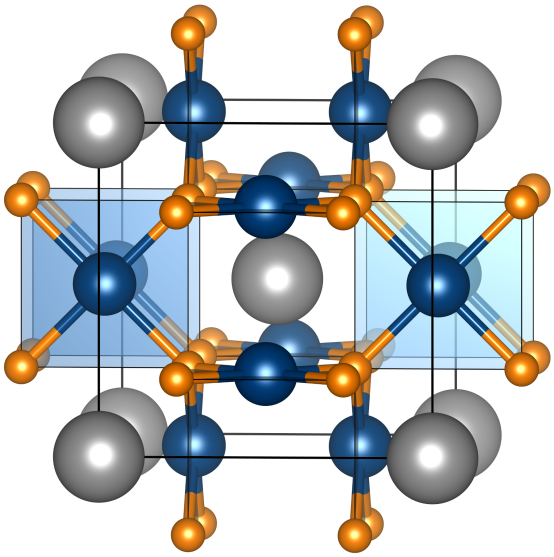

Figure 4.1: Crystal structure of APd$_3$O$_4$ (A = Ca, Sr) in cubic $Pm\bar{3}n$ (#223). Ca/Sr, Pd, and O are colored silver, blue, and orange respectively. The PdO$_4$ square planes in APd$_3$O$_4$ exhibit 3D corner connectivity. The alkaline-earth element sits in a symmetric, 8-coordinate, cubic site. The Wyckoff positions are A in 2a (0, 0, 0,); Pd in 6c ($\frac{1}{4}$, 0, $\frac{1}{2}$); and O in 8e ($\frac{1}{4}$, $\frac{1}{4}$,$\frac{1}{4}$).

would expect that a compositionally driven insulator-to-metal transition in both $CaPd_3O_4$ and $SrPd_3O_4$ would occur around the same dopant level assuming the electronic structures were also similar. However, insulator-to-metal transitions in these compounds have been reported to occur under a wide range of hole-dopant levels. Ichikawa and co-workers reported a transition in $CaPd_3O_4$ around 10 mol % Li doping onto the Ca site.[48]. However, when Na was used as a dopant, Itoh, Yano and Tsuda reported 30 mol % was necessary to drive the transition and remarked how processing can affect the observed electronic properties. [103, 108] In the system $Sr_{1-x}Na_xPd_3O_4$, Taniguchi and co-workers reported a transition around 10 mol % Na.[49]

To better understand the nature of the insulator-to-metal transitions in these compounds and account for the reported differences, we have prepared and processed $Ca_{1-x}Na_xPd_3O_4$ and $Sr_{1-x}Na_xPd_3O_4$ with $0 \leq x \leq 0.2$ under identical conditions. The metallic end-member compound $NaPd_3O_4$ has also been prepared and studied as a reference. We find that while the electronic structures of $CaPd_3O_4$ and $SrPd_3O_4$ are nearly identical, $CaPd_3O_4$ is driven metallic above 10 mol % Na substitution, while $SrPd_3O_4$ remains a semiconductor with a negative $d\rho/dT$ (slope of resistivity as a function of temperature) up to 20 mol % Na substitution. X-ray diffraction studies suggests Na clustering or a distribution gradient in both compounds at high doping levels and, along with solid-state ^{23}Na

NMR, suggests a percolative insulator-to-metal transition in $CaPd_3O_4$. However, increased local disorder observed in both NMR and analysis of total scattering data using the pair distribution function suggest disorder as a barrier to bulk metallicity in $SrPd_3O_4$.

4.2 Experimental and Computational Methods

Polycrystalline samples of $A_{1-x}Na_xPd_3O_4$ (A = Ca, Sr), $0 \leq x \leq 0.2$, were prepared by heating stoichiometric amounts of $CaCO_3$, $SrCO_3$, PdO, and Na_2CO_3 powders. The precursors were ground in an agate mortar and pestle and pressed into a pellet at 100 MPa. The pellets were placed onto beds of powder of the same composition to prevent contamination from the alumina crucible. The samples were heated at 600 °C for 12 hours in a flowing O_2 tube furnace. This procedure was repeated twice to ensure a complete reaction of the precursors. The end-member $NaPd_3O_4$ was prepared in a similar manner at 700 °C.

The crystal structures were characterized by X-ray powder diffraction on a Panalytical Empyrean powder diffractometer with Cu-K_α radiation. Lattice parameters were determined by mixing the prepared materials with a silicon standard and recording from 10° 2θ to 120° 2θ. The x = 0.05 and x = 0.20 samples were additionally studied through synchrotron X-ray diffraction at the 11-

BM beam line at the Advanced Photon Source at Argonne National Laboratory with wavelength $\lambda = 0.414159$ Å. Rietveld[58] refinement was performed using the TOPAS academic software.[89] Crystal structures were visualized using VESTA.[60] Neutron scattering data for pair distribution function (PDF) analysis was collected at the NOMAD diffractometer[109] at the Spallation Neutron Source, Oak Ridge National Laboratory. Least-squares refinement of the reduced PDF was performed using the PDFgui program.[110] Single pulse ^{23}Na solid-state magic angle spinning (MAS) NMR experiments were performed at 300 K on a Bruker ASCEND III HD 400 MHz (9.4 T) spectrometer. Samples were packed into a 4 mm zirconia rotor with Kel-F caps and spun at a rate of 8 kHz. The single pulse experiment used a pulse length of 0.83 μs corresponding to a $\pi/12$ tip angle. The ^{23}Na shifts were referenced to 1 M NaCl. For electrical resistivity measurements, the materials were sintered as bar pellets approximately 9 mm in length and four copper wires were attached with a silver paste before running them in a He refrigerator from 300 K to 25 K. The electronic structure was calculated using density functional theory (DFT) as implemented in the Vienna *ab initio* Simulation Package (VASP)[63, 64] with projector-augmented wave (PAW) pseudopotentials.[66] For structure optimization, the exchange-correlation was described by Perdew-Burke-Ernzerhof within the generalized gradient approximation (GGA-PBE)[67] using a Γ center k-mesh of $8\times8\times8$ and

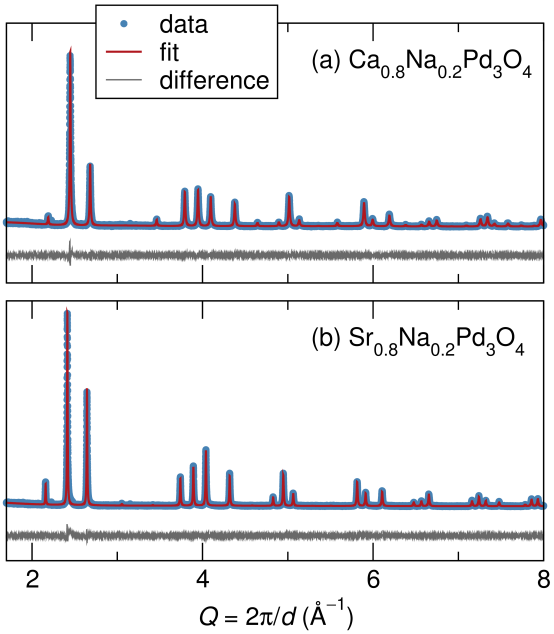

Figure 4.2: Single phase refinements of nominal (a) $Ca_{0.8}Na_{0.2}Pd_3O_4$ and (b) $Sr_{0.8}Na_{0.2}Pd_3O_4$ from synchrotron X-ray data.

a tetrahedron smearing method. A screened hybrid functional (HSE06) [70] was used to calculate the density of states (DOS).

4.3 Results and discussion

4.3.1 Average Structure from Diffraction

Polycrystalline samples of APd_3O_4 (A = Ca, Sr) were prepared phase pure with up to 20 mol % Na substitution onto the A site. The reactions were done

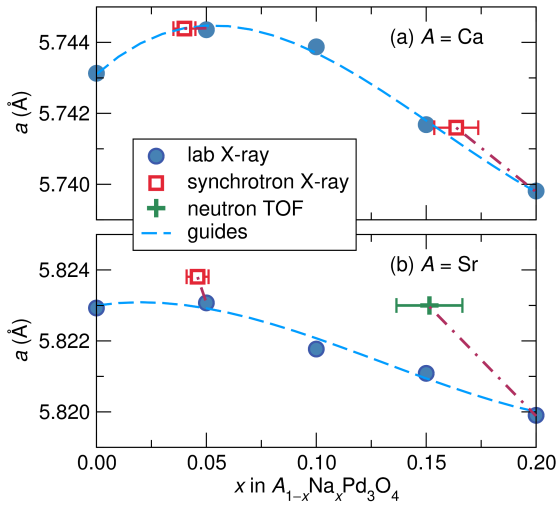

Figure 4.3: Changes in lattice parameters for (a) $Ca_{1-x}Na_xPd_3O_4$ and (b) $Sr_{1-x}Na_xPd_3O_4$ with Na substitution. Blue circles represent stoichiometric Na substitution levels and lattice parameters refined on a laboratory Cu-K_α diffractometer with a Si standard. Red squares represent refined Na occupancy values and lattice parameters from synchrotron X-ray diffraction data for the nominal $x = 0.05$ and $x = 0.20$ substitution levels. The green plus represents the refined Na occupancy value and lattice parameter using neutron diffraction data.

in a flowing O_2 atmosphere at 600 °C to prevent the reduction of the PdO to Pd metal. Rietveld refinements of synchrotron XRD data confirmed the phase purity, shown in Figure 4.2 for the highest Na substitution levels.

The lattice parameters for the samples were determined through Rietveld refinement of laboratory Cu Kα radiation with a Si standard. The lattice pa-

rameters for both the Ca and Sr materials generally decrease with increasing Na doping, as shown in Figure 4.3. The lattice parameter for $CaPd_3O_4$ decreases from 5.743 Å to 5.740 Å and the lattice parameter of $SrPd_3O_4$ decreases by an identical amount, from 5.823 Å to 5.820 Å. This is surprising as the ionic radii of Na^{1+} in an 8-coordinate site (1.18 Å) is slightly larger than Ca^{2+} (1.12 Å) and smaller than Sr^{2+} (1.26 Å). [73] This suggests that the decreasing lattice parameter does not primarily arise from the size difference of the dopant ion, but by the necessary oxidation of the Pd^{2+} to Pd^{3+} to maintain charge neutrality. The slight increase in the lattice parameter with small Na substitution in $CaPd_3O_4$ may be attributed to the larger ionic size of the Na^{1+} ion dominating at smaller substitution levels. Refined Na occupancy values and lattice parameters from the synchrotron X-ray data are shown in Figure 4.3. For the nominal $x = 0.05$ substitution level, the refined Na occupancies are in good agreement with expectations. Peak tails, which are only seen in the high resolution synchrotron X-ray diffraction data for the $x = 0.20$ materials lead to an underestimation of the Na occupancy and a slight discrepancy in the refined lattice parameters, the details of which will be discussed presently. Refined values from neutron time of flight (TOF) diffraction data are used in Figure 4.3 for the $x = 0.20$ Sr sample as the significant peak tails in the X-ray data prevented reliable refinements.

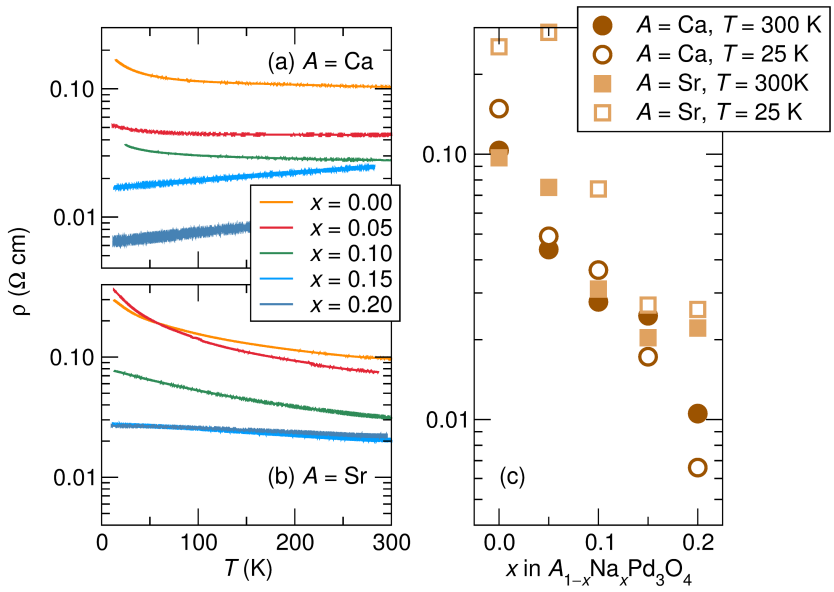

Figure 4.4: Resistivities of APd$_3$O$_4$ (A = Ca, Sr) with Na doping. CaPd$_3$O$_4$ undergoes an insulator-to-metal transition above $x = 0.10$ as seen through the decrease in resistivity with temperature at these levels. Despite similar room temperature resistivity values, SrPd$_3$O$_4$ does not undergo an insulator-to-metal transition even up to $x = 0.20$.

4.3.2 Electrical Properties and Electronic Structure

In order to study the insulator-to-metal transitions in these materials, the electrical resistivity was measured with successive doping. Pristine CaPd$_3$O$_4$ displays semiconducting behavior with a room temperature resistivity of 0.1 Ω cm. An insulator-to-metal transition occurs beyond 10 % Na doping as seen through the positive $d\rho/dT$ for the $x = 0.15$ and $x = 0.20$ compositions, similar

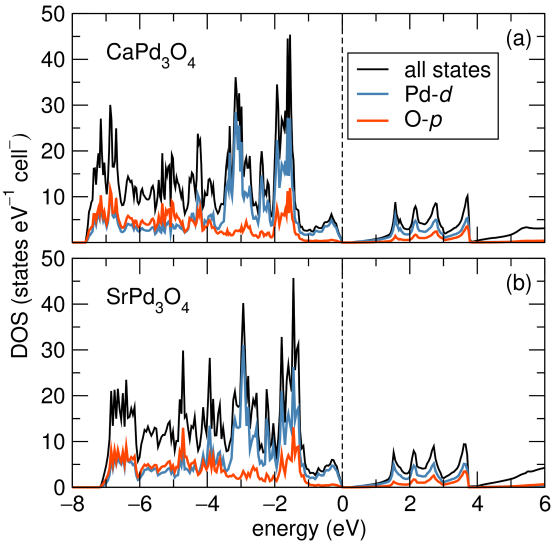

Figure 4.5: Density of states calculated using a hybrid functional for (a) $CaPd_3O_4$ and (b) $SrPd_3O_4$. The calculated bandgaps are 0.25 eV and 0.22 eV, respectively.

to the substitution amount Ichikawa and co-workers reported upon Li doping in $CaPd_3O_4$.[48] Unsubstituted $SrPd_3O_4$ exhibits a room temperature resistivity almost identical to $CaPd_3O_4$. However, even up to $x = 0.20$, the material remains semiconducting with a negative $d\rho/dT$, though the resistivity values are near identical to those reported by Taniguchi and co-workers. [49]. This result is surprising as both materials were prepared and processed identically and from the lattice parameter changes appear to be incorporating the Na dopants up to 20 mol %.

To explore the differing electronic behavior in these compounds, DFT calculations were carried out to investigate any differences in the electronic structure.

The density of states (DOS) for both of the pristine materials are shown in Figure 4.5. It is important to note that the DOS calculations were carried out using a hybrid functional in order to obtain a more accurate band gap value. The HSE calculations predict very small, nearly identical bandgaps of 0.25 eV for $CaPd_3O_4$ and 0.22 eV for $SrPd_3O_4$. Both compounds show significant Pd-d states just below the Fermi level. The DOS for both compounds possess similar features both below and above the Fermi level, and the band structures for both compounds are almost indistinguishable near the Fermi level. The extreme similarities in the electronic structures of these compounds implies that the differences in the onset of the insulator-to-metal transition are not due to any fundamental differences in the physics of the materials, but may be due to deviations in the local structure imparted through hole-doping.

4.3.3 Deviations from Average Structure: Structural Heterogeneities

Close inspection of the synchrotron diffraction data reveals that the nominal $Ca_{0.80}Na_{0.20}Pd_3O_4$ and $Sr_{0.80}Na_{0.20}Pd_3O_4$ samples have peak tails to higher Q on all Bragg peaks, highlighted in the (enlarged) difference curves presented in Figure 4.6. The tails are more pronounced in $Sr_{0.80}Na_{0.20}Pd_3O_4$. For both

the Ca and Sr compounds substituted with only 5 mol % Na, the peaks appear symmetric and the difference curves do not reveal any features. The tails in the highly substituted samples suggest a deviation from the average crystallographic structure. This may be attributed to either a gradient or clustering of the Na dopants as the dopant concentration increases, as a uniform distribution of dopant ions should produce symmetric peaks with a corresponding shift in the lattice parameters.

Two different models were applied to better capture the peak tails in the 20 % substituted samples. To simulate a concentration gradient of Na dopants across the material, a model was created with 8 $Pm\bar{3}n$ phases with the lattice parameter and Na occupancy shifted by a constant amount between each phase. To simulate Na clustering, the second model was constructed of 2 phases where the Na concentration, lattice parameter, and size/strain contributions to the peak shapes were allowed to refine independently. These methods have been used in many material systems to examine phase separation and structural heterogeneity. [111, 112] Figure 4.7 illustrates the fit of each model to the main reflection (021) of $Sr_{0.80}Na_{0.20}Pd_3O_4$. The total Na occupancy was not fixed in either of the models and refined to between 12 % and 16 % total occupancy. While both models are able to capture the peak tails, there is no substantial difference between the two, and the nature of the Na substitution is still unclear

from analysis of the diffraction data.

The peak tails in synchrotron X-ray diffraction data of the highly substituted samples prompt a close study of the local structure in these materials in order to both explore the nature of the insulator-to-metal transition and to explain differences in the observed electronic properties. Neutron PDF data was utilized to investigate local deviations from the average crystallographic structure. Least squares fits of the PDFs are shown in Figure 4.8. The data was fit against the crystallographic structure with nominal site occupancies over a fit range of 1.5 Å to 5 Å. The results of the fits are given in Table 4.1.

By comparing the resulting fits against the average models, relative degrees of local disorder can be ascertained. As demonstrated by the goodness of fit parameters, R_w, (Table 4.1) the 5% substituted $CaPd_3O_4$ and $SrPd_3O_4$ are locally fit well with the average structure. Interestingly, the 20% substituted $SrPd_3O_4$ results in a poorer fit to the average model than the 20% substituted $CaPd_3O_4$, evidenced by a large increase in the resulting Rw value. This is indicative of a more locally disordered structure, and by examining the features of the PDF that are not being captured by the average model, the nature of the distortion may be qualitatively inferred. A significant peak shoulder occurring around 3 Å is present only in the highest substituted $SrPd_3O_4$. This correlation distance corresponds to the Pd–Pd and O–O interactions of proximal Pd square planar units.

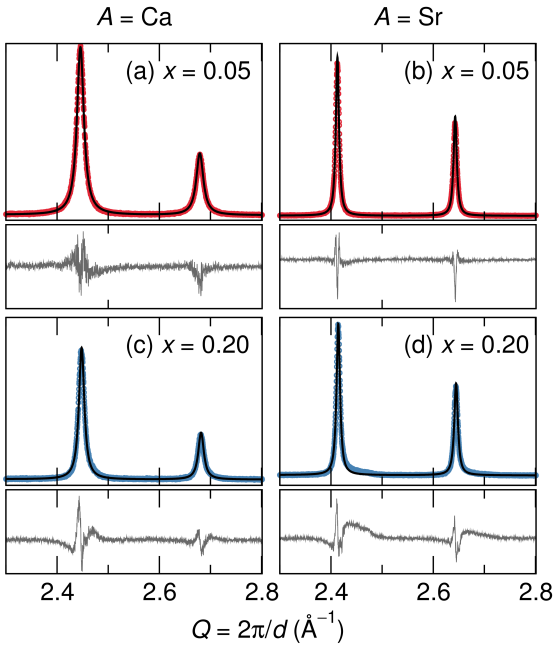

Figure 4.6: Diffraction patterns and Rietveld fits for the 5% Na-substituted (a) $CaPd_3O_4$ and (b) $SrPd_3O_4$ and (c,d) 20 % Na-substituted materials.While the 5 % substituted compounds have symmetric peak shapes, the peaks of the 20 % Na-substituted compounds have a tail to higher Q. This is clearly evident in the difference curves (enlarged for clarity) which possess a broad feature after every peak.

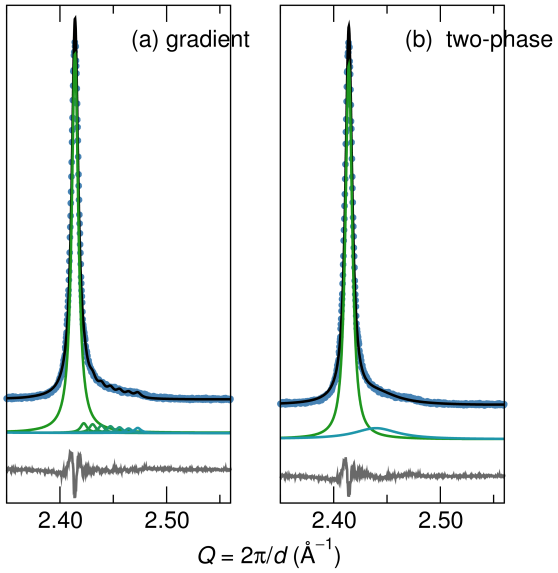

Figure 4.7: Fits of the primary (021) reflections of nominal $Sr_{0.80}Na_{0.20}Pd_3O_4$ using (a) an Na-gradient model and (b) a 2-phase Na-cluster model result in a similar quality fit.

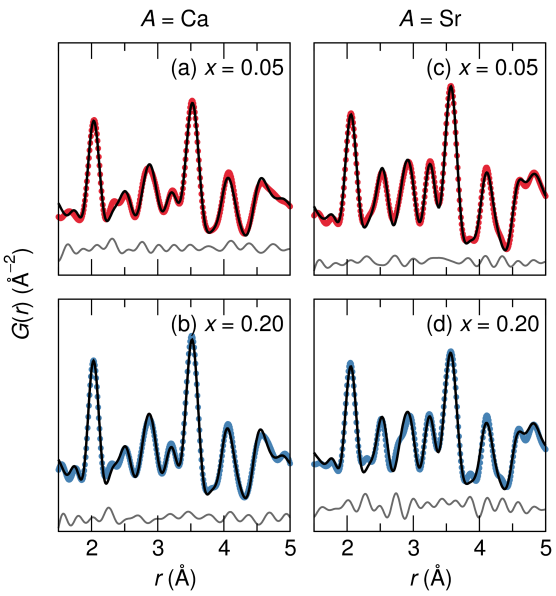

Figure 4.8: PDF fits against the crystallographic structures. Both of the lightly Na-substituted ($x = 0.05$) samples (a,c) and the highly Na-substituted ($x = 0.20$ b,d) $CaPd_3O_4$ are well fit with the average structure. The highly Na-subsituted $SrPd_3O_4$ is comparatively more poorly fit, indicating that the local environment is more disordered.

Table 4.1: Results of fits of the neutron PDF data against the $Pm\bar{3}n$ models for $A_{1-x}Na_xPd_3O_4$ with x = 0.05 and 0.20 and A = Ca and Sr.

	A = Ca		A = Sr	
	x = 0.05	x = 0.20	x = 0.05	x = 0.20
a (Å)	5.759(4)	5.748(3)	5.829(3)	5.821(3)
A/Na U_{iso} (Å^2)	0.0078(18)	0.0077(15)	0.0040(7)	0.0028(7)
Pd U_{iso} (Å^2)	0.0042(6)	0.0034(4)	0.0034(4)	0.0044(4)
O U_{iso} (Å^2)	0.0070(8)	0.0064(6)	0.0055(5)	0.0058(6)
R_w (%)	12.7	11.0	9.0	17.7

Thus, slight distortions of the Pd square planar network around Na dopants may be present, which is reasonable given the greater size difference between the Sr^{2+} and Na^{1+} ions. In addition to local distortions, any potential Na clustering may result in poorer fits to the local structure. A two phase fit including the possibility of a Na_2CO_3 impurity was attempted, as some amount of Na_2CO_3 was observed in solid state ^{23} Na NMR (see next section), though it did not improve the fit or capture the observed peak shoulder.

4.3.4 Deviations from Average Structure: Compositional Heterogeneities

In addition to PDF, solid-state ^{23}Na NMR was conducted to study the resolved local environment of the Na dopants in these materials. ^{23}Na is a spin 3/2 quadrupolar nucleus in 100% abundance, making it an attractive nucleus to study in the materials before and after an insulator-to-metal transition as well as to examine differences between the Ca and Sr compounds. As a reference, we prepared metallic $NaPd_3O_4$, which possesses the same structure as $CaPd_3O_4$ and $SrPd_3O_4$ and can be thought of as a Na substitution level of x = 1.00. The structure of $NaPd_3O_4$ has been reported previously,[18, 113] and reported electric properties are in agreement with our measurements. [103, 108] A higher preparation temperature than was used for Na substitution in $CaPd_3O_4$ and $SrPd_3O_4$ was needed for phase purity. The different panels of Figure 4.9 summarize the results on this interesting metallic oxide. Figure 4.9(a) displays a Rietveld refinement of X-ray diffraction data of $NaPd_3O_4$ displaying a single cubic phase with a =5.638 Å. Figure 4.9(b) displays a dominant peak observed at -6 ppm, as is expected due to the single Na site in the structure. This peak is narrow due to the symmetric environment of the crystallographic site, despite the quadrupolar nature of the ^{23}Na nucleus. A small amount of a potential im-

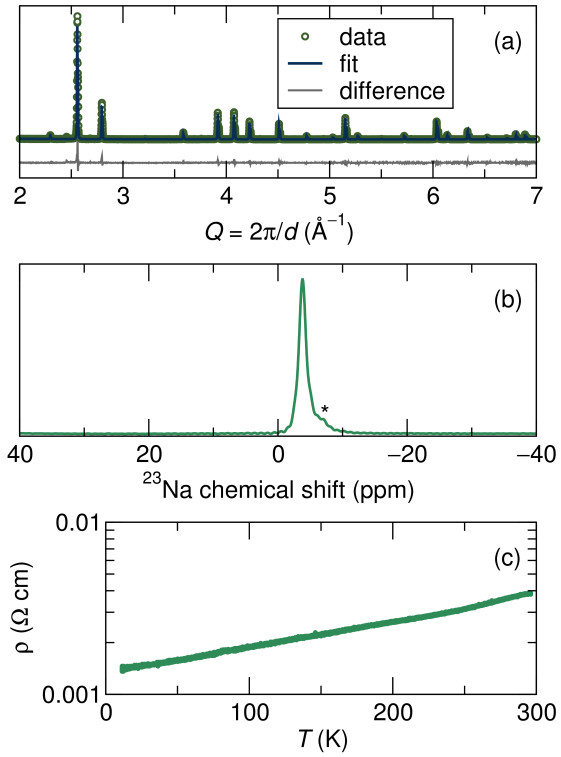

Figure 4.9: Results on the pure end-member ($x = 1$) compound $NaPd_3O_4$. (a) X-ray diffraction Rietveld refinement showing the phase pure nature of this composition. (b) ^{23}Na solid-state single pulse magic angle spinning NMR spectra (9.4 T, MAS at 8 kHz) showing a principle single peak corresponding to the single site in the crystal structure with a potential minor impurity on the right edge of the peak marked by (*). (c) Resistivity *vs.* temperature for a pressed pellet of $NaPd_3O_3$ showing the highly metallic nature of this hole-doped oxide.

purity marked by * in Figure 4.9 may also be present. Note that despite the metallic nature of the sample, established from the resistivity *vs.* temperature data shown in Figure 4.9(c), that the peak is not strongly Knight-shifted by the conduction electrons.[114] The ^{23}Na Knight shift can vary widely in magnitude and direction between various types of Na-substituted compounds,[115–117] but is generally expected to be small in a system like $NaPd_3O_4$ where the conduction states are derived from other atoms, namely Pd.

Figure 4.10 shows magic angle spinning (MAS) spectra of various Na substitution levels in $CaPd_3O_4$ and $SrPd_3O_4$. All of the spectra display two distinct Na environments which is surprising as the Na substitutes onto only one crystallographic site in these materials. A sharp peak centered at 7 ppm and a broad peak around -10 ppm are present at all levels of Na substitution in both series. The broad peak grows in intensity relative to the sharp peak with increasing Na substitution. A small amount of Na_2CO_3 was detected in the $SrPd_3O_4$ samples, denoted with a star in Figure 4.10. Based on the peak shape and chemical shift of the $NaPd_3O_4$ spectrum, we conclude the sharp peaks in the Ca and Sr compounds arise from Na in an undistorted environment, *i.e.* an isolated Na in the APd_3O_4 matrix. The insulating Ca/Sr matrix surrounding the isolated Na explains the differing chemical shifts in regards to the pure Na compound. The broad signal(s) appear at chemical shifts similar to the sharp peak of $NaPd_3O_4$,

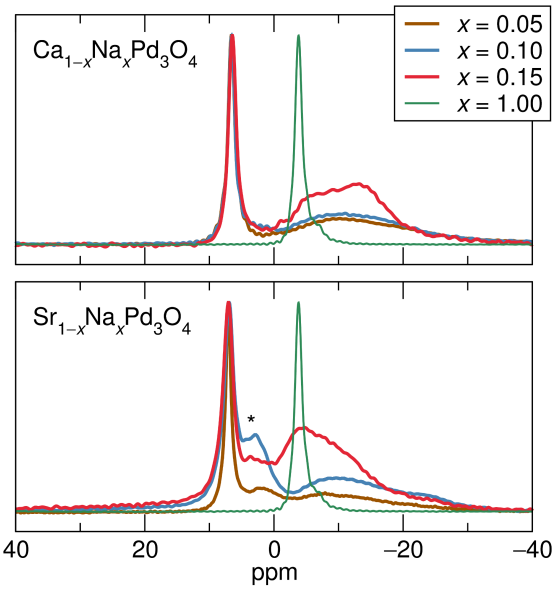

Figure 4.10: Single-pulse solid-state ^{23}Na MAS NMR spectra (9.4 T, MAS at 8 kHz) of Na-substituted $CaPd_3O_4$ and $SrPd_3O_4$. All of the Ca and Sr samples show 2 distinct Na environments represented by a sharp peak at 7 ppm and a broad signal centered around -10 ppm which grows relative to the sharp peak with increasing Na substitution. Metallic $NaPd_3O_4$ ($x = 1.00$) shows a single sharp peak at -6 ppm. The asterisk represents a small amount of Na_2CO_3 precursor.

and thus we propose the origin of the broad peaks as arising from Na in metallic, Na-rich environments. The broadness may arise from a distribution in chemical shifts due to a distribution of the number of proximal Na atoms and/or a distorted Na coordination environment, leading to quadrupolar effects. In $SrPd_3O_4$, this peak is broader and more asymmetric in nature, further supporting a higher degree of disorder in comparison to the Ca sample at the same Na substitution level. Additionally, $SrPd_3O_4$ clearly shows a greater tendency for a clustering of the Na dopants at x = 0.15, as the broad peak begins to coalesce towards the $NaPd_3O_4$ (x = 1.00) peak. The $CaPd_3O_4$ samples do not show as clear a clustering at the Na substitution levels studied through NMR. The greater ionic size difference of Na and Sr most likely leads to the increased propensity for Na clustering. For both samples, the relative intensity of the broad peak grows with increasing Na concentration, suggesting a percolative insulator-to-metal transition mechanism. Even at small Na-substitution levels, there is evidence of metallic domains most likely arising from Na atoms in nearby proximity. However, the local disorder present in the Sr compounds limits the domain growth, thus preventing bulk metallicity.

^{23}Na NMR evidence suggests the formation of what appear to be metallic regions immediately upon Na substitution, despite bulk electrical transport suggesting that the samples remain in the insulating regime.This points to metallic

and insulating regions in the sample that are phase-separated. This phenomena is well known in alkali-metal liquid NH_3 solutions, where the phase separation between more metallic, high alkali-content liquid from the insulating, less concentrated liquid can be physically observed, and has also been followed by NMR.[118] The phenomena of such microscopic phase separation was predicted by Mott,[119] who pointed out that the insulator and the metal must lie in separate minima of the free energy characteristic of first-order phase transitions. Similar local heterogeneity has been observed in Li-NMR of ^{7}Li-deintercalated $LiCoO_2$,[120] and in a study of Li-ordering in $Li_{1-x}Sn_{2+}As_2$.[121]

In conclusion, Na has been substituted into both $CaPd_3O_4$ and $SrPd_3O_4$ under identical conditions and subtle differences in the local structure of these materials have been studied. Despite identical crystal and electronic structures, $CaPd_3O_4$ is more easily driven metallic with hole doping through Na substitution. Neutron pair distribution function data reveal $SrPd_3O_4$ is more locally disordered with high Na substitution. ^{23}Na NMR reveals an apparent percolative insulator-to-metal transition mechanism as metallic domains in the materials grow with increasing Na substitution. Increased disorder and a tendency for the Na to cluster when substituted into $SrPd_3O_4$ are believed to act against metallicity by limiting metallic domain growth. This work highlights the need for detailed local probes to elucidate differences in observed material properties

that are not easily explained by average structure techniques such as diffraction.

Chapter 5

Dopant Size Influences on the Structure and Electronic Properties of $A\mathrm{Pd_3O_4}$ (A = Ca, Sr)

The choice of dopant in materials systems can play an important role on the observed functional properties. The cubic, semiconducting compounds $A\mathrm{Pd_3O_4}$ (A = Ca, Sr) are hole-doped with either Li, Na, or K onto the A site in order to observe any change in the structure or electrical resistivity imparted by varying the size of the hole-dopant. A small, yet distinct second phase is observed

[1] Shahryar Mooraj, Joshua Bocarsly and Ram Seshadri have contributed to the contents of this chapter.

through synchrotron X-ray diffraction in $Sr_{0.8}K_{0.2}Pd_3O_4$ that is not present when Li or Na is used as the dopant. This phase can be fit identically to the pristine $SrPd_3O_4$ crystal structure with a smaller lattice parameter suggesting that the K dopant is phase separating into local regions of KPd_3O_4. Density functional theory calculations support the observation that K behaves differently when used as a hole-dopant compared to Li or Na. These calculations predict an ordering of the K dopant in the $SrPd_3O_4$ matrix. Electronic transport measurements show a slight decrease in resistivity with increasing size of the hole-dopant for the A = Sr materials.

5.1 Introduction

As discussed in the previous chapter, the degree of structural disorder induced by a Na hole-dopant varies between semiconducting $SrPd_3O_4$ and $CaPd_3O_4$ despite both of these materials possessing the same crystal structure. The impact of this disorder has profound effects on the observed electronic transport properties. As observed through solid state ^{23}Na NMR, the Na dopant in $Sr_{1-x}Na_xPd_3O_4$ showed a tendency at high x values to form local regions of metallic $NaPd_3O_4$. This apparent Na "clustering"' was not as evident in $Ca_{1-x}Na_xPd_3O_4$, suggesting that the Na dopant was distributing more evenly in

this material. This difference may be attributed to the differing ionic sizes of the involved elements. 8 coordinate Na^{1+} possesses an ionic radius of 1.18 Å which is closer to 8 coordinate Ca^{2+} (1.12 Å) than Sr^{2+} (1.26 Å).[73]

Na is not the only potential hole-dopant in these complex palladium oxide systems. Li has also been shown to drive these semiconducting materials metallic, though there is a great discrepancy in the amount of dopant needed to drive the insulator-metal transition which may also depend on preparation and processing conditions. Between 10 % and 30 % of alkali metal substitution has been reported as necessary to drive the transition. [48, 49, 103, 108] Naively, one would expect the choice of alkali metal dopant to make no difference on the observed structure and electronic properties of these $A Pd_3O_4$ systems as they should all contribute one hole. Observed differences may be attributed to the size and distribution of the chosen dopant atom and are crucial to understand for these and other systems.

For example, in a thermoelectric material, the dopant choice may impact the thermal conductivity in addition to the electrical properties. Evenly distributed dopants may act as point defects and efficiently scatter short wavelength phonons, whereas dopant clusters appearing phase separated would affect phonon scattering and thus thermal conductivity differently. This influence has been studied in Heusler and half-Heulser materials. Half-Heuslers of for-

mula XYZ consist of a rocksalt arrangement of the X and Z atoms with the Y atoms ordering on half of the tetrahedral sites. Corresponding Heusler compounds of formula XY_2Z have Y atoms completely filling the 8 tetrahedral sites. Incorporating excess Y atoms into the half-Heusler may cause the full Heusler to phase separate out or may lead to the formation of a solid solution based on the constituent elements and processing conditions. The resulting microstructure can greatly impact the observed thermoelectric properties.[112, 122, 123]

In particular for these $A\text{Pd}_3\text{O}_4$ materials and others undergoing compositionally driven insulator-metal transitions, understanding dopant behavior is crucial in regards to tuning the Fermi level. Recently, SrPd_3O_4 was predicted to be a Dirac semimetal with linear band crossings close to the Fermi level.[124] Dirac semimetals possess unique and attractive transport properties due to the massless nature of the charge carriers. These properties are optimized when the crossing occurs directly at the Fermi level as in graphene.[125] Thus, an attractive dopant would not impart much strain or disorder into the crystal, so as to not change the electronic band structure beyond adjusting the position of the Fermi level.

In order to observe changes in local disorder with differences in hole doping, polycrystalline samples of $A_{1-x}X_x\text{Pd}_3\text{O}_4$ (A = Ca, Sr X = Li, Na, K) have been prepared. Synchrotron X-ray diffraction conducted on the Sr compounds reveals

that when K is chosen as a hole dopant, a second phase precipitates out. This is contrary to Li, and Na dopants in which local disorder is only evident through peak tailing in the diffraction patterns. DFT calculations correspondingly predict a different behavior in the K substituted materials. No evidence of phase separation is present in the Ca compounds. Along with the differences in the local structure, the electrical resistivity decreases slightly with increasing ionic radius. Our results suggest that dopant choice may serve a useful role in tuning structural properties concurrently wtith electronic properties for applications such as thermoelectrics.

5.2 Experimental and Computational Methods

Polycrystalline samples of $A_{1-x}X_xPd_3O_4$ (A = Ca, Sr (X = Li, Na, K, Ag), $0 \leq x \leq 0.2$, were prepared by heating stoichiometric amounts of $CaCO_3$, $SrCO_3$, PdO, Li_2CO_3, Na_2CO_3, and K_2CO_3 powders. The precursors were ground in an agate mortar and pestle and pressed into a pellet at 100 MPa. The pellets were placed onto beds of powder of the same composition to prevent contamination from the alumina crucible. The samples were heated at 700 °C for 12 hours in a flowing O_2 tube furnace. This procedure was repeated twice to ensure a complete reaction of the precursors.

The crystal structures were characterized by X-ray powder diffraction on a Panalytical Empyrean powder diffractometer with Cu-K_α radiation. Some samples were additionally studied through synchrotron X-ray diffraction at the 11-BM beam line at the Advanced Photon Source at Argonne National Laboratory with wavelength $\lambda = 0.412666\,$Å. Rietveld[58] refinement was performed using the TOPAS academic software.[89] Crystal structures were visualized using VESTA.[60] For electrical resistivity measurements, the materials were sintered as bar pellets approximately 9 mm in length and four copper wires were attached with a silver paste before running them in a He refrigerator from 300 K to 25 K.

DFT was used to study the energetics of the solid solutions between $SrPd_3O_4$ and APd_3O_4 (A = K, Na, Li) by enumerating supercells with some Sr atoms replaced by A atoms. All such symmetrically inequivalent decorations with supercells with volume up to 3 times the volume of the primitive cubic SrPd3O4 cell were enumerated using the CASM code. [126–129] The energies of each cell was calculated using VASP, as described previously. K-mesh densities of about 3500 points / (number of atoms in cell) were used. Pymatgen was used to set up and run the VASP calculations. [130]

5.3 Results and discussion

Polycrystalline samples of APd$_3$O$_4$ (A = Ca, Sr) were prepared with up to 20 mol % Li, Na, or K substitution onto the A site. The reactions were done in a flowing O_2 atmosphere at 700 °C to prevent the reduction of the PdO to Pd metal. Rietveld refinements of synchrotron XRD data confirmed the phase purity, shown in Figure 5.1 for the highest substitution levels of the dopants in SrPd$_3$O$_4$. The K substituted Sr compound possessed a second phase of identical crystal structure with smaller lattice parameters which will be discussed in detail.

Both SrPd$_3$O$_4$ and CaPd$_3$O$_4$ crystallize in the cubic space group Pm$\bar{3}$n (223). The lattice parameter decreases for both materials regardless of which alkali metal is used as a hole dopant. Figure 5.2 shows the decrease in lattice parameter versus the ionic radii of the alkali metal used to dope. From smallest to largest, this corresponds to Li, Na, and then K. For reference, the ionic radii of Ca^{2+} and Sr^{2+} are 1.12 Å and 1.26 Å respectively. The dashed lines denote the lattice parameter of the stoichiometric, unsubstituted materials. There are no immediately obvious trends in the change of lattice parameter with ionic radii of the dopant or differences between SrPd$_3$O$_4$ and CaPd$_3$O$_4$. It is important to note that the lattice parameters decrease with K substitution despite K^+ being

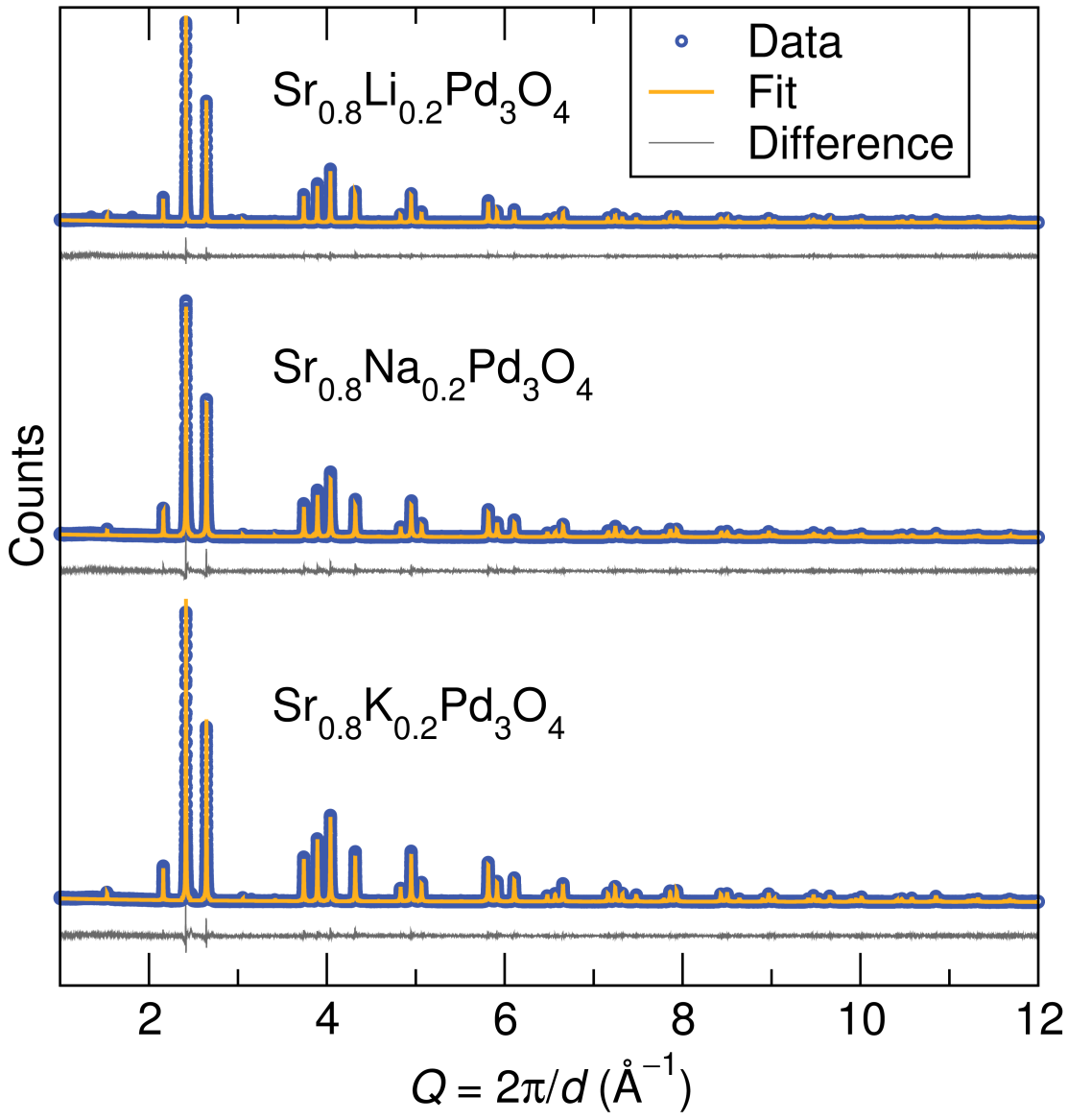

Figure 5.1: X-ray diffraction patterns of $Sr_{0.8}Li_{0.2}Pd_3O_4$, $Sr_{0.8}Na_{0.2}Pd_3O_4$, $Sr_{0.8}K_{0.2}Pd_3O_4$ fit through a one phase refinement.

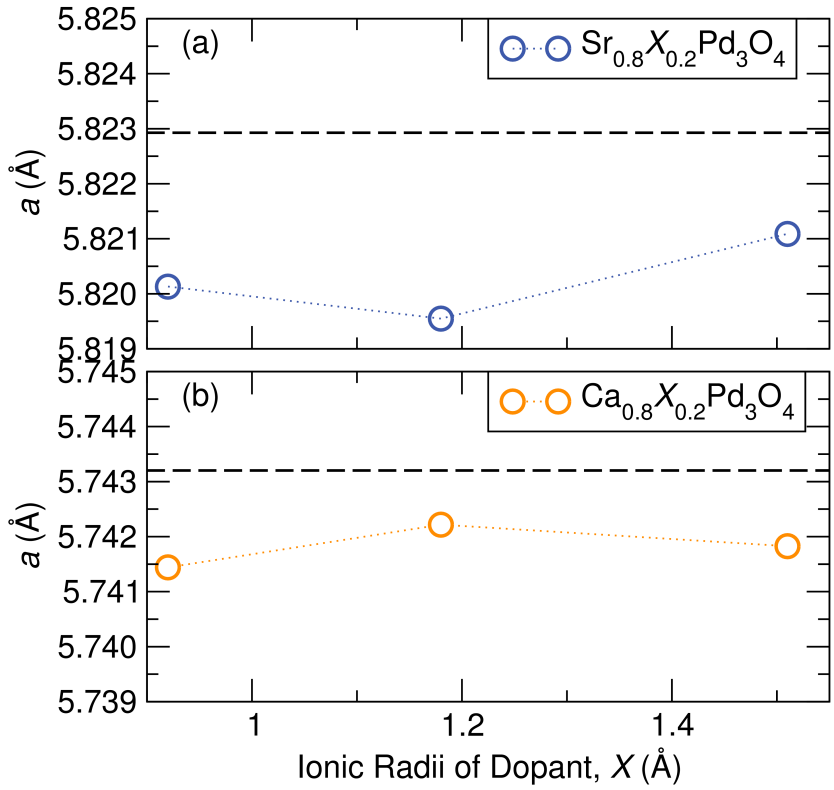

Figure 5.2: Lattice parameter decrease of (a) $Sr_{0.8}X_{0.2}Pd_3O_4$ and (b) $Ca_{0.8}X_{0.2}Pd_3O_4$ (X = Li, Na, K) versus the ionic radi of the X dopant. All dopants decrease the lattice parameter by roughly the same amount implying that the oxidation of Pd^{2+} to Pd^{3+} is the primary driver of the contraction. Dashed lines represent the lattice parameter of the pristine, unsubstituted compounds.

considerably bigger than both Ca^{2+} and Sr^{2+} which can be explained by the necessary oxidation of Pd^{2+} to Pd^{3+} to maintain charge neutrality with hole doping.

A close examination of the synchrotron XRD patterns can explain this and inform differing behavior amongst the choice of dopant atoms for the Sr compound. The two most intense (021) and (211) diffraction peaks from the synchrotron diffraction patterns are shown in Figure 5.3 with their corresponding fits and difference curves from one-phase Rietveld refinements. As seen in prior work,[90] the Bragg peaks of the Na substituted material possess peak tails to high Q that are not accurately capture by a symmetric peak refinement. $Sr_{0.8}Li_{0.2}Pd_3O_4$ also possesses the same peak tailing, though less dramatic. These tails were previously described as arising from either a gradient distribution of the Na dopant or a tendency for the Na dopants to cluster forming regions of $NaPd_3O_4$ like material in an $SrPd_3O_4$ matrix. ^{23}Na solid state NMR data further showed some evidence of some clustered regions amongst a large degree of local disorder suggesting that it is probably a combination of both leading to the peak tailing.

The diffraction pattern of $Sr_{0.8}K_{0.2}Pd_3O_4$ differs from those of $Sr_{0.8}Li_{0.2}Pd_3O_4$ and $Sr_{0.8}Na_{0.2}Pd_3O_4$. Rather than peak tailing, low intensity, but distinct, peaks are observable after each peak of the main phase. These peaks can be fit very well with a second phase of the same $Pm\bar{3}n$ crystal structure with a smaller

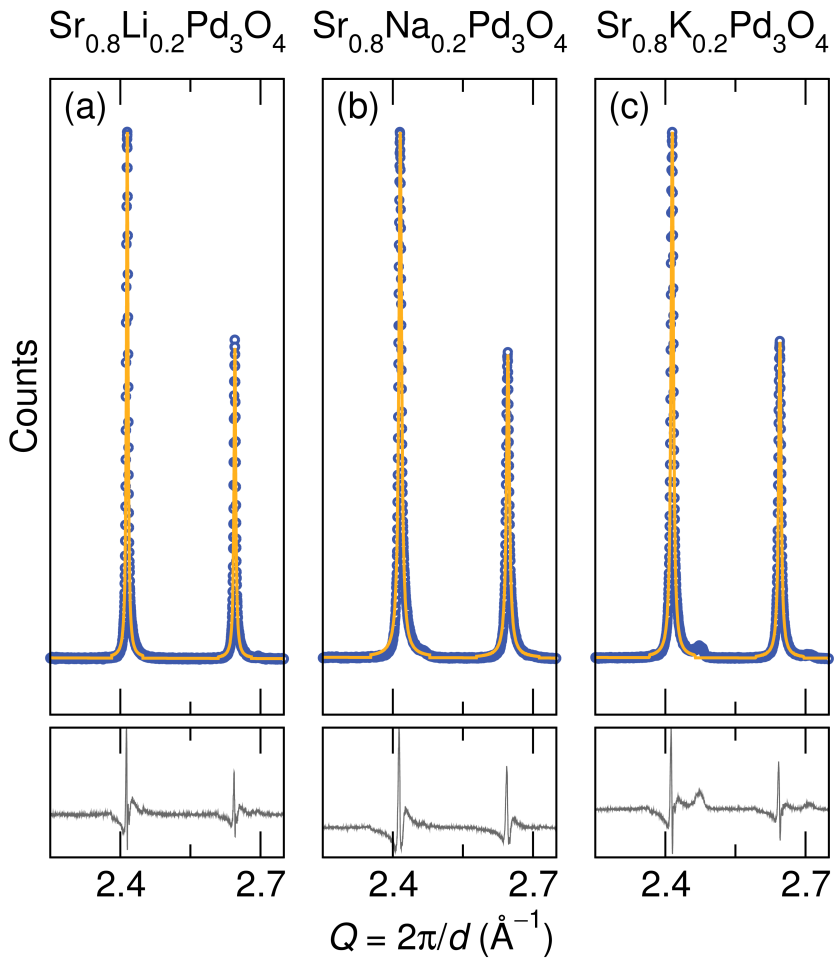

Figure 5.3: Comparison of 1 phase Rietveld refinements focusing on select Bragg reflections in (a) $Sr_{0.8}Li_{0.2}Pd_3O_4$, (b) $Sr_{0.8}Na_{0.2}Pd_3O_4$, and (c) $Sr_{0.8}K_{0.2}Pd_3O_4$. Peak tailing is evident in (b) while a distinct second phase shifted to higher Q is present in (c).

lattice parameter of 5.692 Å. This is strong evidence that the K dopants have a much stronger tendency than the Li or Na dopants to cluster together to form regions of "KPd_3O_4" like material. While the low intensity of these reflections make confidant occupancy refinements difficult, the site occupancy of the Sr/K site refines to almost fully K occupied, further supporting that this second phase consists of clustered K dopants.

Thus a trend with ionic radii size of the dopant can be described in which the larger dopants atoms have a greater tendency to substitute nearer each other. This is seen through the relatively symmetric diffraction peaks of $Sr_{0.8}Li_{0.2}Pd_3O_4$, then the peak tailing in $Sr_{0.8}Na_{0.2}Pd_3O_4$ and then a fully distinct second phase in $Sr_{0.8}K_{0.2}Pd_3O_4$. As shown in Figure 5.2, $Sr_{0.8}K_{0.2}Pd_3O_4$ has a lattice parameter that is much closer to the stoichiometric $SrPd_3O_4$ material. This observation can also be explained by the clustering of the K dopant, as the main phase would have less dopant in its lattice. No evidence of a second phase was seen in diffraction data of Li,Na, or K doping in $CaPd_3O_4$. This is unexpected as the ionic size difference between Ca^{2+} and K^{+} is even greater than that of Sr^{2+} and K^{+} suggesting that ionic size differences are not solely responsible for the varying dopant distributions.

In order to understand the driving forces behind the differing behavior of the K dopant, density functional theory (DFT) calculations were conducted to

assess the relative stability of model crystals with varying concentrations and orderings of the dopants. Figure 5.4 summarizes these calculations for the Li, Na, and K dopants in $SrPd_3O_4$. Each circle represents one calculation with the given dopant concentration and energy per Sr site relative to the interpolation of the energies of the two end members. The circle color denotes cell volumes of either 1, 2 or 3 times the size of the standard $SrPd_3O_4$ unit cell. Multiple points at a given dopant concentrations correspond to the number of symmetrically distinct orderings of the dopant that are possible. It is clear that the relative energies for the K substituted $SrPd_3O_4$ compounds are much lower than those of the Na substituted and Li substituted compounds whose energies scatter around 0 meV/Sr site.

The strongly negative relative energies for K substituted $SrPd_3O_4$ shown in Figure 5.4 imply that an ordered arrangement of K dopants is the most stable. A hull of positive energies would predict that the K is more stable phase separating into regions of $SrPd_3O_4$ and KPd_3O_4. For the Na and Li substituted compounds, the small relative energies both above and below zero imply that the dopants do not tend to either order or phase separate, and will likely randomly substitute into the $SrPd_3O_4$ lattice.

The DFT calculations do not support that the second phase evident in the preparation of $Sr_{0.8}K_{0.2}Pd_3O_4$ is a clustered KPd_3O_4phase but instead could be

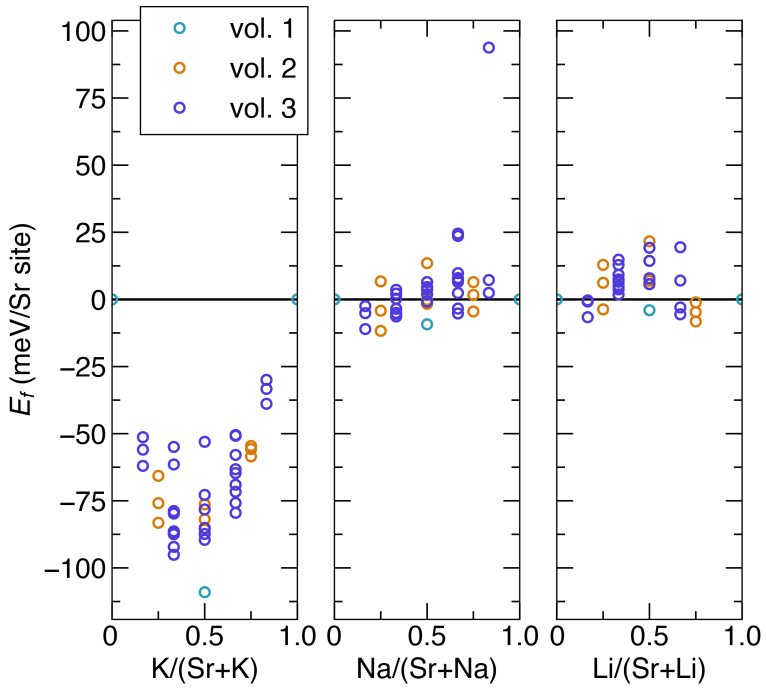

Figure 5.4: DFT calculations of solid solutions of Li, Na, and K substitution in $SrPd_3O_4$. Each circle represents one possible, unique arrange of the dopant atom in a cell either 1, 2 or 3 times the size of the standard $SrPd_3O_4$ unit cell given my the color. Strongly negative energies indicate a more stable, ordered arrangment of the dopant while energies above 0 indicated instability and a drive to phase separate.

a phase consisting of K ordered onto the lattice of Sr sites. Due to the structural similarity of the relatively stable phases shown in Figure 5.4 the expected diffraction patterns would posses peaks at identical positions. New diffraction peaks due to the lowering of symmetry would be low intensity. Attempts to refine the second phase with these predicted K orderings have been inconclusive. Despite the high resolution provided by synchrotron radiation, the small amount of the second phase results in any potentially identifying diffraction peaks to be too low intensity for observation. While the second phase is clearly evident only in the K substituted material, it is not exactly clear whether it consists of K ordered on a Sr lattice or a completely K clustered phase. The significantly smaller lattice parameter of the second phase suggests that it consists of more oxidized Pd^{3+} than the main phase. It is also important to note that the second phase does not appear to be a meta-stable phase resulting from slow diffusion kinetics of K as the phase fraction of the second phase grows slightly with repeated heatings.

The electrical resistivity of $SrPd_3O_4$ substituted with either 15 mol % or 20 mol % Li, Na or K is shown in Figure 5.5. At 15 mol % substitution levels, all three samples are semiconducting with resistivity increasing with decreasing temperature. At 20 mol % substitution levels, all samples transition into metallic behavior with resistivity decreasing with decreasing temperature. It is impor-

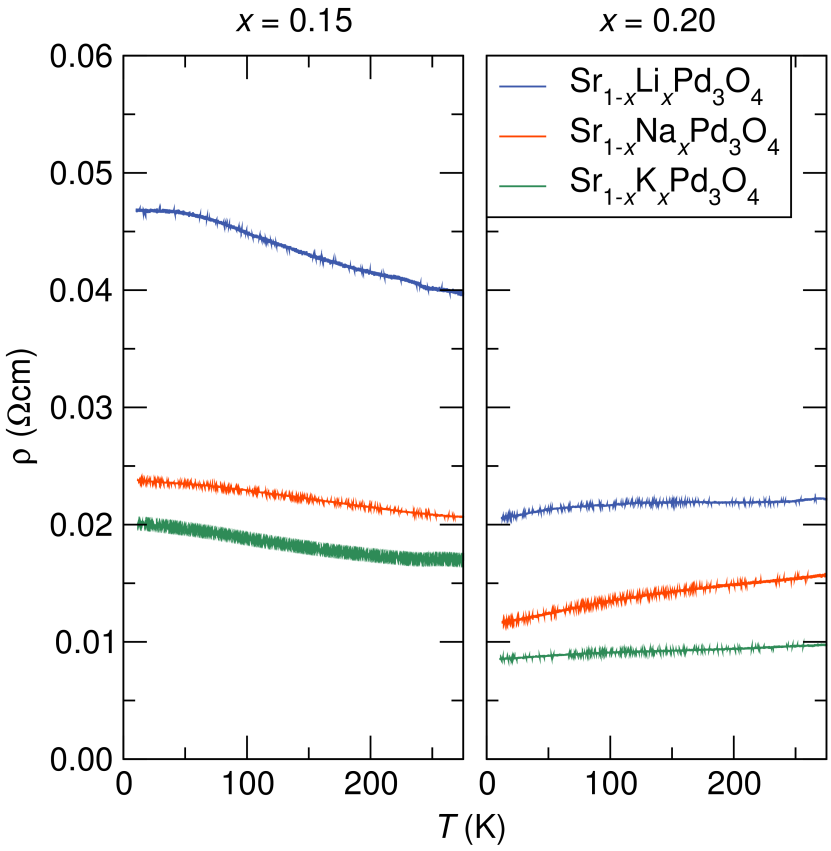

Figure 5.5: Electrical resistivity of $Sr_{1-x}X_xPd_3O_4$ (X = Li, Na, K) (x = 0.15, 0.20) The change in slope for all dopants indicates the change in electric transport behavior from semiconducting (x = 0.15) to metallic (x= 0.20).

tant to note that this behavior is different than in our previous study in which a 20 mol% Na substitution did not lead to metallic behavior. This discrepancy can be explained by the higher preparation temperature of 700 °C verses the 600 °C of our prior study. The higher temperature was selected to better ensure the reactivity of the various precursors and likely removes much of the local disorder evident in the prior work.

There exists a trend across both substitution levels that the resistivity decreases with increasing ionic size. This observation along with the trend for the larger dopant ions to substitute closer together further suggest that the insulator-metal transition is driven through a percolation mechanism. Regions that are richer in the dopant atom behave more metallic and at a significant dopant concentration analogous to a a percolation threshold, bulk metallic behavior is observed. Resistivity measurements of the same substitution levels in hole-doped $CaPd_3O_4$ do not show any clear trend with dopant choice, which is not unexpected as the structural analysis did not give any evidence of differing distributions between the three hole dopants.

The distinct phases present in $Sr_{0.8}K_{0.2}Pd_3O_4$, but not $Sr_{0.8}Li_{0.2}Pd_3O_4$ or $Sr_{0.8}Na_{0.2}Pd_3O_4$ broadly reflect the importance of structural considerations with regard to functional materials properties. While Li,Na, and K, substitution all correspond to nominally equivalent hole-doping, the resulting crystal structures

of the three materials are not completely identical. Local disorder or strain concurrent with varying dopant distributions may lead to varying, unexpected behavior. Understanding the structural changes imparted by the dopant atoms is crucial for the optimization of functional properties.

5.4 Conclusions

We have prepared polycrystalline samples of $A_{1-x}X_x$Pd$_3$O$_4$ (A = Ca, Sr X = Li, Na, K). While all three of the X atoms correspond to hole-doping equal amounts of carriers into the system, they do not all substitute identically. In SrPd$_3$O$_4$, the larger hole dopants appear to substitute proximal to each other. This is seen through peak tailing in the diffraction pattern of Sr$_{0.8}$Na$_{0.2}$Pd$_3$O$_4$ and a crystallographically similar second phase precipitating out in Sr$_{0.8}$K$_{0.2}$Pd$_3$O$_4$. Density functional theory calculations support the observed synchrotron diffraction data in that K substitution in SrPd$_3$O$_4$ behaves differently than Li, or Na substitution. While DFT predicts that the observed second phase consists of an ordered arrangement of the K dopant, Rietveld refinement to confirm the identity is not possible owing to the low intensity of the reflections. Interestingly, there is no clear phase separation in Ca$_{0.8}$K$_{0.2}$Pd$_3$O$_4$. The electrical resistivity shows a trend with a decrease in resistivity corresponding to an increase the the

dopant size, suggesting a kind of percolation insulator-metal transition mechanism. This work illustrates the importance of structural considerations when doping in oxide semiconductors which may impact a wide variety of functional applications such as thermoelectrics.

Chapter 6

Outlook and Summary

6.1 The Role of Complex Palladium Oxides for Advancing Thermoelectrics

Oxides are an attractive class of materials for thermoelectric applications necessitating high temperature, air stability, though currently only p-type layered cobaltate compounds have shown sufficient performance. The spin degeneracy of the mixed valent cobalt atoms is believed to lead to high Seebeck coefficients with metallic electrical conductivity. It is prudent to explore new oxide materials in order to potentially discover new, varying mechanisms that can also lead to comparable performance, ideally in n-type oxides. The presence of compo-

sitionally driven insulator-metal transitions in many complex palladium oxides naturally prompts their study as thermoelectric materials, as the delicate interplay of the Seebeck coefficient and electrical transport is generally optimized in the middle of such transitions.

We identified $PbPdO_2$ as a potentially interesting thermoelectric material as its demonstrably small band gap would likely make hole doping successful.[54] The layered connectivity of the Pd square planes together with the lone pair of the Pb atoms would potentially allow for favorable electrical properties and a low thermal conductivity. As discussed in Chapter 2 and in our publication,[43] when Li was used a hole dopant and substituted onto the Pd site, favorable electrical properties for thermoelectric applications are observed. The electrical resistivity drops of $PbPdO_2$ drops by an order of magnitude with Li substitution, while the Seebeck coefficient remains greater than 100 μV/K at room temperature. The Seebeck coefficient continuously increases up to 600 K leading to a measured zT of 0.12.

A key finding of our work is that the Seebeck coefficient and electrical resistivity of polycrystalline Li-substituted $PbPdO_2$ are near identical to polycrystalline Na_xCoO_2, which prompted the research into the cobaltate compounds and renewed interest in oxides as thermoelectrics.[41] Consisting of almost entirely diamagnetic, square planar Pd^{2+}, the electrical performance of Li-

substituted $PbPdO_2$ is believed to arise from mechanisms distinct from Na_xCoO_2 which possess a high degree of spin entropy from the mixed valent cobalt atoms. Electronic structure calculations support experimental measurements which suggest other complex palladium oxides are worth investigating in order to better understand structural, and compositional motifs which may lead to high Seebeck coefficients in metallic materials. Indeed, since the publication of our work, the Wolverton group at Northwestern has computationally examined Bi_2PdO_4 for thermoelectric performance and concluded it may also possess a high Seebeck coefficient with metallic resistivities when hole-doped. They conclude that having a stacked square planar arrangment can lead to a favorable electronic structure.[94] Pb substitution for the Bi atom has been shown to successfully hole dope Bi_2PdO_4 though the resistivity remained in the semiconducting regime.[88] Li-substitution for the Pd atom, as in $PbPdO_2$, has not been carried out so far in the literature.

With the success of Li-substituted $PbPdO_2$, we explored a structurally similar material, $LiBiPd_2O_4$. As detailed in Chapter 5, both Pb substitution onto the Bi site, and excess Li substitution onto the Pd site were found to successfully hole-dope the material resulting in a decrease in resistivity by over three orders of magnitude. Only 5% Li substitution was needed to drive this large decrease, similar to Li substitution in $PbPdO_2$ which saw drastic changes with

small amounts of substitution. Up to 20% Pb was found to substitute into the structure before impurities were observed through X-ray diffraction. While the resistivity of hole-doped $LiBiPd_2O_4$ was drastically lowered, it remained too high for practical thermoelectrical applications. Analysis of the calculated electronic structure imply that the differing connectivity of the Pd square planes leads to a larger band gap and thus higher resistivity. The substitution of Pb for Bi was also studied through ^{7}Li solid state NMR. Despite only one crystallographic Li site in the material, 5 distinct Li environments are observed upon Li substitution. While the exact origin of these sites can not be precisely determined, they suggest possibly an asymmetric distribution of the Pb atoms, and potentially evidence of metallic percolation from a slight Knight shift. Nevertheless, further studies of hole-doping in related complex oxides may continue to inform the design of new thermoelectric materials.

6.2 Hole-Doping in $SrPd_3O_4$ and $CaPd_3O_4$

In addition to exploring the thermoelectric functionality of complex palladium oxides, there was also fundamental interest in studying the compositionally driven insulator-metal transitions in these materials. As 4d, diamagnetic oxides, complex palladium oxides are ideal avenues to study these tran-

sitions owing to their lack of magnetism and comparatively small amounts of electron-electron correlation and spin-orbit coupling. Isostructural $SrPd_3O_4$ and $CaPd_3O_4$ have been reported in the literature to undergo compositionally driven insulator-metal transitions with either Li or Na substitution, but the reported level of necessary doping varies widely. A comparative study of Na-substitution in isostructural $SrPd_3O_4$ and $CaPd_3O_4$ revealed the influence of local disorder on the onset of metallic behavior. High degrees of local is disorder as evidenced through the pair distribution function of neutron scattering data and ^{23}Na NMR are present in $Sr_{0.8}Na_{0.2}Pd_3O_4$ that are much less evident in $Ca_{0.8}Na_{0.2}Pd_3O_4$. This disorder is believed to act as a barrier to bulk metallic behavior.

We have found NMR useful in informing the transition from semiconducting to insulating behavior in these materials. The use of NMR to study local environments with carrier doping is generally difficult due to paramagnetic transition metals, requiring careful and long collection times, and providing spectra that are difficult to interpret. The diamagnetic palladium oxides allow for comparatively simpler MAS experiments. Using ^{23}Na NMR, we observe, upon Na substitution, two distinct Na environments despite one crystallographic site. A sharp peak decreases in intensity relative to a broader, shifted peak with increasing Na substitution. The broad peak occurs at the same position as the single Na environment in metallic $NaPd_3O_4$. Thus, we interpret this as evidence of a per-

colative insulator-metal transition in which Na in a metallic environment grows relative to Na in an insulating environment with increasing Na substitution.

To better inform the influence of local disorder and dopant distribution on observed electrical properties, further studies were conducted on these materials in which the hole-dopant was varied. Understanding structural changes imparted through chemical substitutions is important for a wide variety of materials applications. Li^+, Na^+, and K^+ were used as hole dopants in $SrPd_3O_4$ and $CaPd_3O_4$. We find that when K^+ is used as a dopant in $SrPd_3O_4$, regions of either phase separated KPd_3O_4 or some K-ordered phase result. This is not observed with the smaller hole-dopants or in $CaPd_3O_4$. DFT calculations suggest that K^+ substitution should lead to an ordered phase whereas Li^+, and Na^+ do not show any preference for ordering.

The electrical resistivity of $SrPd_3O_4$ decreases slightly with increasing size of the hole dopant with $Sr_{0.8}K_{0.2}Pd_3O_4$ being the least resistive. This is understandable if the K is ordering in the $SrPd_3O_4$ matrix. The hole-doped $CaPd_3O_4$ did not show any trend with electrical resistivity which is not unexpected as there was no evidence of preferential ordering amongst the dopants. These works highlight the importance of structural considerations with chemical substitutions in oxide materials. Dopant choice may affect local disorder as well as change the preferential distribution into the primary material which should be considered

when attempting to improve functional properties.

6.3 Future Directions for Functionality in Complex Palladium Oxides

We have identified favorable thermoelectric performance in some complex palladium oxides, while also making efforts to fundamentally understand how these materials transition from semiconducting to metallic behavior. There exist still other complex palladium oxides that may also compliment the work describe here. As mentioned, $BiPd_2O_4$ has been identified through DFT as a potentially high performing thermoelectric.[94] Li substitution in this material may be expected to successfully drive it metallic and would hopefully confirm these predictions and inform the role of square planar coordination in supplying high Seebeck coefficients in metallic materials. Other complex palladium oxides should be examined for small bandgaps and favorable square planar coordination for high thermoelectric performance.

The use of solid state NMR is a very promising avenue to study carrier doping in oxides and diamagnetic complex palladium oxides are ideal for this purpose. Continued work in this area would be beneficial to confirm our current

explanation of percolation driven insulator-metal transition mechanisms while informing how to observe and control dopant distributions. While changes in dopant distribution didn't drastically impact the observed electrical resistivities here, there is evidence in Heusler systems, for example, that control of dopant distribution is important for optimizing the interplay of thermal conductivity, electrical resistivity, and Seebeck coefficient in thermoelectrics. It would be of particular interest to explore structurally analogues complex platinum oxides to see if the same trends hold and the role signficiant spin-orbit coupling would play.

Beyond electronic functionality, more attention should be paid to the magnetic properties of complex palladium oxides and 4d oxides in general. Many 4d oxides possess magnetic transition temperatures higher than their 3d counterparts, one example of which being $PdAs_2O_6$ with a transition temperature over 100 K higher than 3d analogues. Preparing magnetic palladium compounds require unusual coordination for palladium atoms. There are sparse reports of Pd^{2+} in an octahedral coordination which allows for 2 unpaired spins. One potential avenue for preparing new complex palladium oxides with this coordination is through optimizing the tolerance factor in a double perovskite structure. By choosing counter cations of ideal sizes so that the structure as a whole is favorable, Pd^{2+} may be forced into octahedral coordination. There is one report in

the literature of Ca_2PdWO_6 prepared through a simple solid state reaction.[131] No magnetic measurements were reported and our attempts to prepare this material and related ones were unsuccessful. Nevertheless, more preparation attempts, potentially using high oxygen pressures, may stabilize these structures.

The work detailed here addressed the electronic functionality of several complex palladium oxides upon hole-doping. Favorable thermoelectric performance has been observed and local disorder imparted through the doping is related to the onset of metallic behavior. There still exists a great need to further study these and related $4d$ and $5d$ oxides in the search for improved materials functionality and fundamental understandings.

Appendix A

Electronic Structure of $NaPt_3O_4$

A.1 Introduction

The study of topological materials has emerged as a significant branch of condensed matter physics.[132] The fundamental physics and potential applications of these materials make them an attractive topic of research for physicists, solid-state chemists, and material scientists alike.[133, 134] Dirac semimetals represent one class of topological materials with exciting potential. The key feature of Dirac semimetals is a linear band crossing in the band structure. Linear bands lead to massless charge carriers which in turn provide exceptional electronic transport properties. Ideally, this band crossing should occur at or near

the Fermi level and without any other bands at the same energy. Graphene is a 2D example of such a system. [125] There exists a strong push to find new 3D materials that also possess linear band crossings near the Fermi level. Recently, Na_3Bi[135] and Cd_3As_2[136] have been identified as 3D Dirac semimetals. There is a huge push to develop design principals and identify new Dirac semimetals. [137, 138]

Analyzing and understanding crystallographic and compositional motifs that lead to linear band crossings proximal to the Fermi level is crucial in identifying new topologically interesting materials and advancing potential technological applications. To this end, we present electronic structure calculations on a series of noble metal oxides, NaA_3O_4 (A = Pd, Pt). These materials possess topological features about 200meV above the Fermi energy,[124] though we further identify a linear band crossing in $NaPt_3O_4$ just below the Fermi level. Highlighting the need for significant spin orbit coupling to achieve topologically interesting materials, we observe that this crossing is not present in $NaPd_3O_4$ owing to the lighter Pd atom. Calculations neglecting spin orbit coupling also break the crossing. The orbital character of the linear bands is primarily from the Pt d states with the d_{z^2} orbitals comprising one of the linear bands and d_{xy} orbitals comprising the other.

A.2 Computational Methods

The electronic structure was calculated using density functional theory (DFT) as implemented in the Vienna *ab initio* Simulation Package (VASP)[63, 64] with projector-augmented wave (PAW) pseudopotentials.[66] For structure optimization, the exchange-correlation was described by Perdew-Burke-Ernzerhof within the generalized gradient approximation (GGA-PBE)[67] using a Γ center k-mesh of $10\times10\times10$.

A.3 Results and Discussion

$NaPd_3O_4$ and $NaPt_3O_4$ both crystallize in the cubic $Pm\bar{3}n$ space group (223). By simple analysis of the valency of the atoms, the Pd/Pt atoms are nominally $2.33+$, making them metallic. This is in contrast to the band semiconducting compounds with Ca or Sr replacing the Na which lead to d^8 Pd/Pt $2+$ and filled orbitals in the square planar crystal field splitting. The electronic structure of $NaPt_3O_4$ is given in Figure A.1. The band structure of $NaPd_3O_4$ is quite similar, though as will be discussed possesses a key difference. It is important to note that this calculation does include spin orbit coupling (SOC). The PBE functional is used as these materials are metallic and thus the tendency for PBE to under-

estimate band gaps, particularly in palladium containing compounds[54] is not relevant. We focus our attention on the bands near the Fermi level from the Γ to X high symmetry points. These bands are quite linear and cross just below the Fermi level, two necessary qualities for the realization of Dirac semimetals for functional applications. While there are clearly other bands crossing at the Fermi level elsewhere in the Brillouin Zone, the crossing between Γ and X is still of fundamental interest.

A key feature of many topological materials is the presence of significant SOC. SOC is the driving force behind many of the band inversions of topological insulators. Here we present further evidence that materials with large of amounts of SOC due to heavy atoms may be fruitful areas to look for new Dirac semimetal materials. To illustrate the importance of SOC in $NaPt_3O_4$, calculations of $NaPt_3O_4$ and $NaPd_3O_4$ have been performed with SOC turned off. The area of interest between Γ to X and near the Fermi level is heavily influenced by SOC, as shown in Figure A.2

What was a band crossing in $NaPt_3O_4$ is very slightly gapped out in $NaPd_3O_4$. The gap is present and more obvious when SOC is removed from the calculation of $NaPt_3O_4$. Both of these band structures highlight the significant effect of strong SOC. In $NaPd_3O_4$ the Pd is not heavy enough for the SOC to lead to a linear band crossing. Likewise, without any SOC at all, $NaPt_3O_4$ does not show

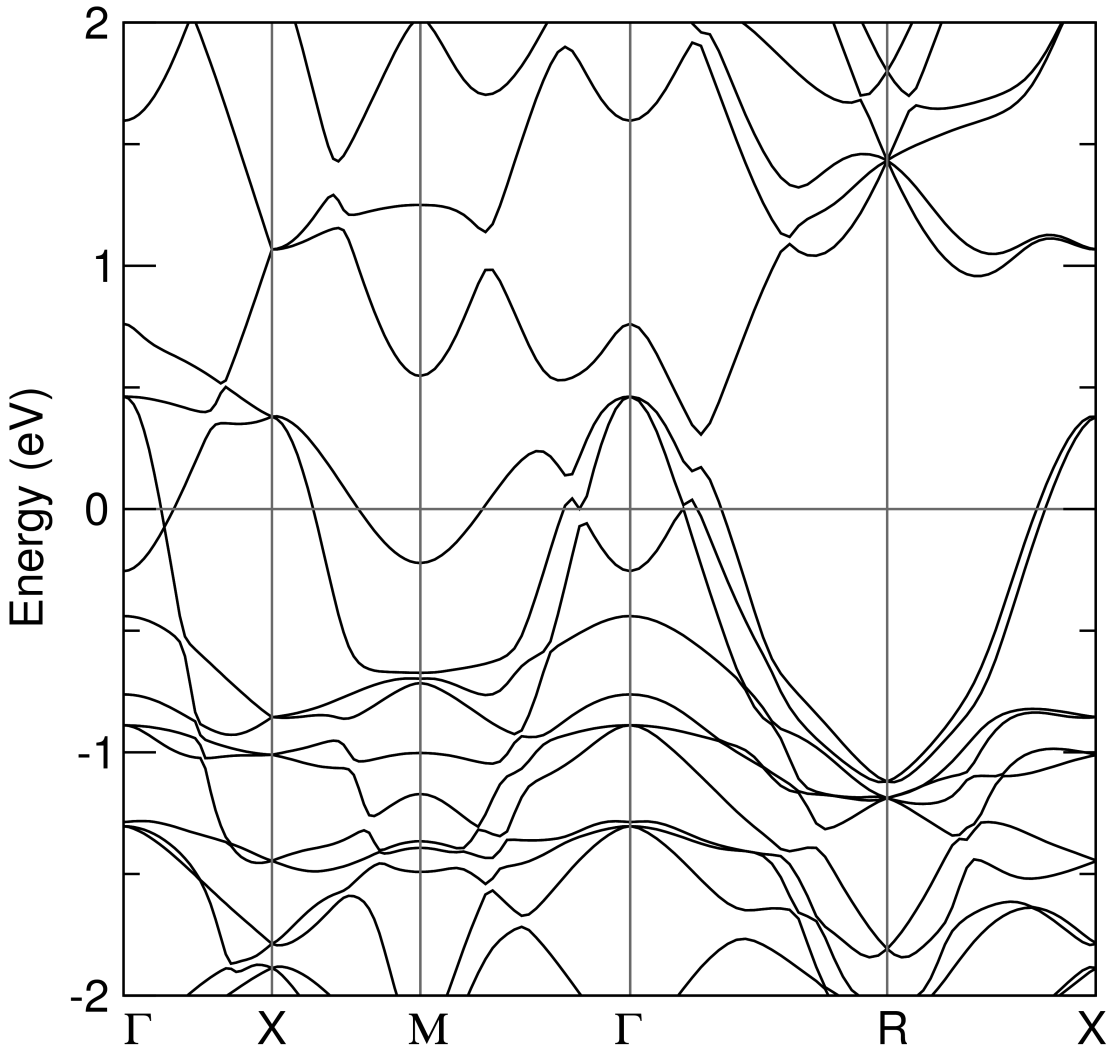

Figure A.1: Band structure of $NaPt_3O_4$ including spin-orbit coupling. A linear band crossing is observed near the Fermi level between the Γ and X points.

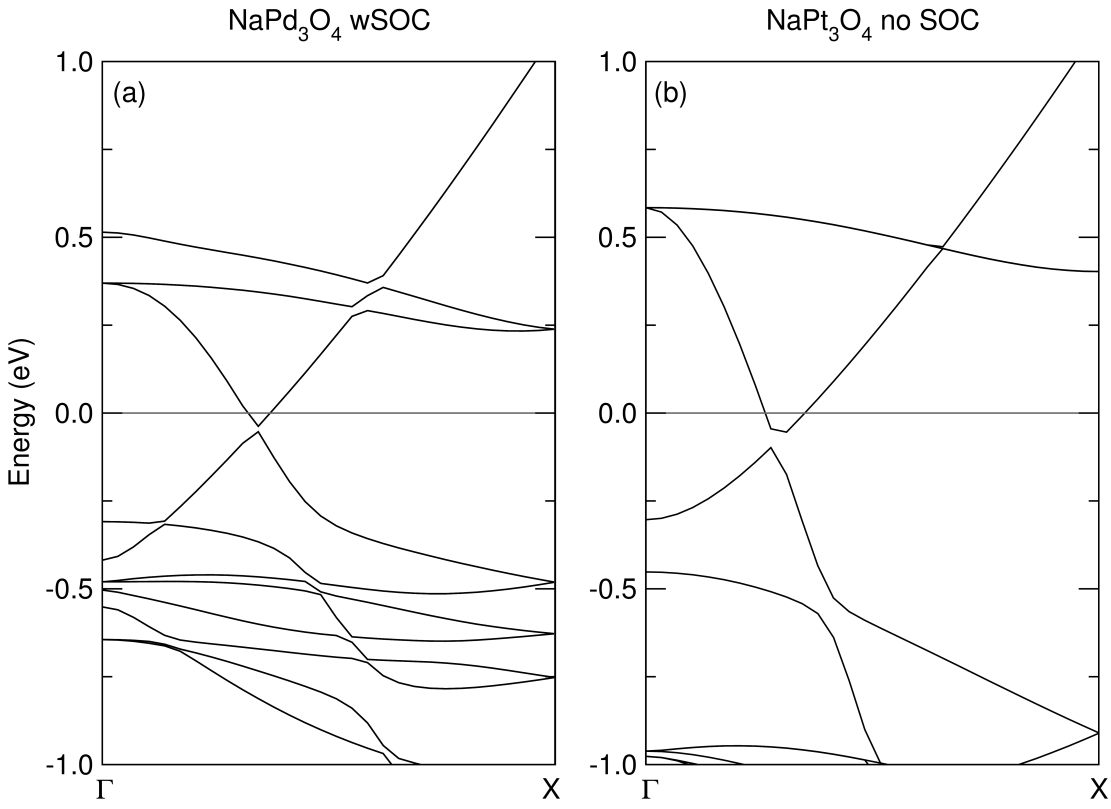

Figure A.2: Γ to X path in $NaPd_3O_4$ (with SOC) and $NaPt_3O_4$ (no SOC). The crossing is gapped out when the spin-orbit coupling is weaker as in $NaPd_3O_4$ or removed from $NaPt_3O_4$.

a crossing. Better understanding the character of this crossing will be useful in furthering understanding of design principals for Dirac semimetals.

Bibliography

[1] C. N. R. Rao. Transition metal oxides. *Annu. Rev. Phys. Chem.*, 40(1):291–326, 1989.

[2] Y. Du and X. Wan. The novel electronic and magnetic properties in 5d transition metal oxides system. *Comput. Mater. Sci.*, 112:416–427, 2016.

[3] C. Dhital, T. Hogan, W. Zhou, X. Chen, Z. Ren, M. Pokharel, Y. Okada, M. Heine, W. Tian, Z. Yamani, C. Opeil, J. S. Helton, J. W. Lynn, Z. Wang, V. Madhavan, and S. D. Wilson. Carrier localization and electronic phase separation in a doped spin-orbit-driven Mott phase in $Sr_3(Ir_{1-x}Ru_x)_2O_7$. *Nat. Commun.*, 5:3377, 2014.

[4] B. J. Kim, H. Ohsumi, T. Komesu, S. Sakai, T. Morita, H. Takagi, and T. Arima. Phase-sensitive observation of a spin-orbital Mott state in Sr_2IrO_4. *Science*, 323(5919):1329–1332, 2009.

[5] I. Nagai, N. Shirakawa, S-i. Ikeda, R. Iwasaki, H. Nishimura, and M. Kosaka. Highest conductivity oxide $SrMoO_3$ grown by a floating-zone method under ultralow oxygen partial pressure. *Appl. Phys. Lett.*, 87(2):24105, 2005.

[6] T. Katsufuji, H. Y. Hwang, and S.-W. Cheong. Anomalous magnetotransport properties of $R_2\mathrm{Mo_2O_7}$ near the magnetic phase boundary. *Phys. Rev. Lett.*, 84(9):1998–2001, 2000.

[7] Y. Maeno, H. Hashimoto, K. Yoshida, S. Nishizaki, T. Fujita, J. G. Bednorz, and F. Lichtenberg. Superconductivity in a layered perovskite without copper. *Nature*, 372:532, 1994.

[8] E. E. Rodriguez, F. Poineau, A. Llobet, B. J. Kennedy, M. Avdeev, G. J. Thorogood, M. L. Carter, R. Seshadri, D. J. Singh, and A. K. Cheetham. High temperature magnetic ordering in the 4d perovskite $SrTcO_3$. *Phys. Rev. Lett.*, 106(6):67201, 2011.

[9] M. Sathiya, A. M. Abakumov, D. Foix, G. Rousse, K. Ramesha, M. Saubanère, M. L. Doublet, H. Vezin, C. P. Laisa, A. S. Prakash, D. Gonbeau, G. Van Tendeloo, and J.-M. Tarascon. Origin of voltage decay in high-capacity layered oxide electrodes. *Nat. Mater.*, 14:230, 2014.

[10] D. Mikhailova, O. M. Karakulina, D. Batuk, J. Hadermann, A. M. Abakumov, M. Herklotz, A. A. Tsirlin, S. Oswald, L. Giebeler, M. Schmidt, J. Eckert, M. Knapp, and H. Ehrenberg. Layered-to-tunnel structure transformation and oxygen redox chemistry in $LiRhO_2$ upon Li extraction and insertion. *Inorg. Chem.*, 55(14):7079–7089, 2016.

[11] J. A. Kurzman, L. M. Misch, and R. Seshadri. Chemistry of precious metal oxides relevant to heterogeneous catalysis. *Dalt. Trans.*, 42(41):14653–14667, 2013.

[12] P. Pyykko and J. P. Desclaux. Relativity and the periodic system of elements. *Acc. Chem. Res.*, 12(8):276–281, 1979.

[13] K. S. Pitzer. Relativistic effects on chemical properties. *Acc. Chem. Res.*, 12(8):271–276, 1979.

[14] L. M. Misch, J. Brgoch, A. Birkel, T. E. Mates, G. D. Stucky, and R. Seshadri. Rapid microwave preparation and ab Initio studies of the stability of the complex noble metal oxides La_2BaPdO_5 and La_2BaPtO_5. *Inorg. Chem.*, 53(5):2628–2634, 2014.

[15] R. D. Shannon, D. B. Rogers, and C. T. Prewitt. Chemistry of noble metal oxides. I. Syntheses and properties of ABO_2 delafossite compounds. *Inorg. Chem.*, 10(4):713–718, 1971.

[16] G. Krämer and M. Jansen. $LaPd_2O_4$, a novel mixed valent oxopalladate. *J. Solid State Chem.*, 114(1):206–210, 1995.

[17] R. V. Panin, N. R. Khasanova, C. Bougerol, W. Schnelle, G. Van Tendeloo, and E. V. Antipov. Ordering of Pd^{2+} and Pd^{4+} in the mixed-valent palladate KPd_2O_3. *Inorg. Chem.*, 49(4):1295–1297, 2010.

[18] R. V. Panin, N. R. Khasanova, A. M. Abakumov, E. V. Antipov, G. Van Tendeloo, and W. Schnelle. Synthesis and crystal structure of the palladium oxides $NaPd_3O_4$, Na_2PdO_3 and $K_3Pd_2O_4$. *J. Solid State Chem.*, 180(5):1566–1574, 2007.

[19] S.-J. Kim, S. Lemaux, G. Demazeau, J.-Y. Kim, and J.-H. Choy. $LaPdO_3$: The first PdIII oxide with the perovskite structure. *J. Am. Chem. Soc.*, 123(42):10413–10414, 2001.

[20] M. Reehuis, T. Saha-Dasgupta, D. Orosel, J. Nuss, B. Rahaman, B. Keimer, O. K. Andersen, and M. Jansen. Magnetic properties of $PdAs_2O_6$: A dilute spin system with an unusually high Néel temperature. *Phys. Rev. B*, 85(11):115118, 2012.

[21] A. M. Nakua and J. E. Greedan. Structural and magnetic properties of transition metal arsenates, $A As_2O_6$, A = Mn, Co, and Ni. *J. Solid State Chem.*, 118(2):402–411, 1995.

[22] R. P. Rao, R. C. Sherwood, and N. Bartlett. Weak ferromagnetism in PdF_2. *J. Chem. Phys.*, 49(8):3728–3730, 1968.

[23] J. W. Stout and E. Catalano. Heat capacity of zinc fluoride from 11 to 300K. Thermodynamic functions of zinc fluoride. Entropy and heat capacity associated with the antiferromagnetic ordering of manganous fluoride, ferrous fluoride, cobaltous fluoride, and nickelous fluoride. *J. Chem. Phys.*, 23(11):2013–2022, 1955.

[24] J. Bruns, M. Eul, R. Pöttgen, and M. S. Wickleder. Octahedral Pd2+ coordination and ferromagnetic ordering in $Pd(S_2O_7)$. *Angew. Chemie Int. Ed.*, 51(9):2204–2207, 2012.

[25] R.i Uriu, D. Shimada, and N. Tsuda. Metal to insulator transition in $Pd_{1-x}Li_xO$. *J. Phys. Soc. Japan*, 60(7):2479–2480, 1991.

[26] F. Hensel, D. R. Slocombe, and P. P. Edwards. On the occurrence of metallic character in the periodic table of the chemical elements. *Phil. Trans. R. Soc. A*, 373:691–696, 1983.

[27] M. Imada, A. Fujimori, and Y. Tokura. Metal-insulator transitions. *Rev. Mod. Phys.*, 70(4):1039–1263, 1998.

[28] Z. Yang, C. Ko, and S. Ramanathan. Oxide electronics utilizing ultrafast metal-insulator transitions. *Annu. Rev. Mater. Res.*, 41(1):337–367, 2011.

[29] F. J. Morin. Oxides which show a metal-to-insulator transition at the Néel temperature. *Phys. Rev. Lett.*, 3(1):34–36, July 1959.

[30] M. M. Qazilbash, M. Brehm, B.-G. Chae, P.-C. Ho, G. O. Andreev, B.-J. Kim, S. J. Yun, A. V. Balatsky, M. B. Maple, F. Keilmann, H.-T. Kim, and D. N. Basov. Mott transition in VO_2 revealed by infrared spectroscopy and nano-imaging. *Science*, 318(5857):1750–1753, 2007.

[31] K. L. Holman, T. M. McQueen, A. J. Williams, T. Klimczuk, P. W. Stephens, H. W. Zandbergen, Q. Xu, F. Ronning, and R. J. Cava. Insulator to correlated metal transition in $V_{1-x}Mo_xO_2$. *Phys. Rev. B*, 79(24):245114, 2009.

[32] T. Yao, X. Zhang, Z. Sun, S. Liu, Y. Huang, Y. Xie, C. Wu, X. Yuan, W. Zhang, Z. Wu, G. Pan, F. Hu, L. Wu, Q. Liu, and S. Wei. Understanding the nature of the kinetic process in a $\mathrm{VO_2}$ metal-insulator transition. *Phys. Rev. Lett.*, 105(22):226405, 2010.

[33] S. A. Corr, D. P. Shoemaker, B. C. Melot, and R. Seshadri. Real-space investigation of structural changes at the metal-insulator transition in $\mathrm{VO_2}$. *Phys. Rev. Lett.*, 105(5):56404, 2010.

[34] C. W. Chu, L. Z. Deng, and B. Lv. Hole-doped cuprate high temperature superconductors. *Phys. C*, 514:290–313, 2015.

[35] G. J. Snyder and E. S. Toberer. Complex thermoelectric materials. *Nat. Mater.*, 7(2):105–114, 2008.

[36] K. Ellmer. Past achievements and future challenges in the development of optically transparent electrodes. *Nat. Photonics*, 6:809, 2012.

[37] G. Hautier, A. Miglio, G. Ceder, G.-M. Rignanese, and X. Gonze. Identification and design principles of low hole effective mass p-type transparent conducting oxides. *Nat. Commun.*, 4:2292, 2013.

[38] BCS Incorporated. Waste heat recovery: Technology and opportunities in U.S. industry. Technical report, U.S. Department of Energy - Industrial Technologies Program, 2008.

[39] K. Koumoto, Y. Wang, R. Zhang, A. Kosuga, and R. Funahashi. Oxide thermoelectric materials: A nanostructuring approach. *Annu. Rev. Mater. Res.*, 40(1):363–394, 2010.

[40] S. Walia, S. Balendhran, H. Nili, S. Zhuiykov, G. Rosengarten, Q. H. Wang, M. Bhaskaran, S. Sriram, M. S. Strano, and K. Kalantar-zadeh. Transition metal oxides – thermoelectric properties. *Prog. Mater. Sci.*, 58(8):1443–1489, 2013.

[41] I. Terasaki, Y. Sasago, and K. Uchinokura. Large thermoelectric power in $NaCo_2O_4$ single crystals. *Phys. Rev. B*, 56(20):R12685—-R12687, 1997.

[42] Y. Wang, N. S. Rogado, R. J. Cava, and N. P. Ong. Spin entropy as the likely source of enhanced thermopower in $Na_xCo_2O_4$. *Nature*, 423(6938):425–428, 2003.

[43] L. K. Lamontagne, G. Laurita, M. W. Gaultois, M. Knight, L. Ghadbeigi, T. D. Sparks, M. E. Gruner, R. Pentcheva, C. M. Brown, and R. Seshadri. High thermopower with metallic conductivity in p-type Li-substituted $PbPdO_2$. *Chem. Mater.*, 28(10):3367–3373, 2016.

[44] M. W. Gaultois, T. D. Sparks, C. K. H. Borg, R. Seshadri, W. D. Bonificio, and D. R. Clarke. Data-driven review of thermoelectric materials: Performance and resource considerations. *Chem. Mater.*, 25(15):2911–2920, 2013.

[45] S. Okada and I. Terasaki. Physical properties of Bi-based rhodium oxides with RhO_2 hexagonal layers. *Jpn. J. Appl. Phys.*, 44:1834–1837, 2005.

[46] Y. Klein, S. Hébert, D. Pelloquin, V. Hardy, and A. Maignan. Magnetoresistance and magnetothermopower in the rhodium misfit oxide $[Bi_{1.95}Ba_{1.95}Rh_{0.1}O_4][RhO_2]_{1.8}$. *Phys. Rev. B*, 73(16):165121, 2006.

[47] W. Kobayashi, S. Hébert, D. Pelloquin, O. Pérez, and A. Maignan. Enhanced thermoelectric properties in a layered rhodium oxide with a trigonal symmetry. *Phys. Rev. B*, 76(24):245102, 2007.

[48] S. Ichikawa and I. Terasaki. Metal-insulator transition in $Ca_{1-x}Li_xPd_3O_4$. *Phys. Rev. B*, 68(23):233101, 2003.

[49] T. Taniguchi, Y. Nagata, T. C. Ozawa, M. Sato, Y. Noro, T. Uchida, and H. Samata. Insulator–metal transition induced in $Sr_{1-x}Na_xPd_3O_4$ for small Na-substitutions. *J. Alloys Compd.*, 373(12):67–72, 2004.

[50] T. C. Ozawa, T. Taniguchi, Y. Nagata, Y. Noro, T. Naka, and A. Matsushita. Metal–insulator transition and large thermoelectric power of a layered palladium oxide: $PbPdO_2$. *J. Alloys Compd.*, 388(1):1–5, 2005.

[51] V. H. Meyer and H.K. Muller-Buschbaum. A new cross linkage of planar polyhedra around Pd^{2+} in $PbPdO_2$. *Z. Anorg. Allg. Chem.*, 442:26–30, 1978.

[52] X. L. Wang. Proposal for a new class of materials: Spin gapless semiconductors. *Phys. Rev. Lett.*, 100(15):156404, 2008.

[53] S. W. Chen, S. C. Huang, G. Y. Guo, J. M. Lee, S. Chiang, W. C. Chen, Y. C. Liang, K. T. Lu, and J. M. Chen. Gapless band structure of $PbPdO_2$: A combined first principles calculation and experimental study. *Appl. Phys. Lett.*, 99(1):012103, 2011.

[54] J. A. Kurzman, M.-S. Miao, and R. Seshadri. Hybrid functional electronic structure of $PbPdO_2$, a small-gap semiconductor. *J. Phys. Condens. Matter*, 23(46):465501, 2011.

[55] K. J. Lee, S. M. Choo, J. B. Yoon, K. M. Song, Y. Saiga, C.-Y. You, N. Hur, S. I. Lee, T. Takabatake, and M. H. Jung. Magnetic properties of gapless semiconductors: $PbPdO_2$ and $PbPd_{0.9}Co_{0.1}O_2$. *J. Appl. Phys.*, 107(9):09C306, 2010.

[56] H. L. Su, S. Y. Huang, Y. F. Chiang, J. C. A. Huang, C. C. Kuo, Y. W. Du, Y. C. Wu, and R. Z. Zuo. Unusual high-temperature ferromagnetism of $PbPd_{0.81}Co_{0.19}O_2$ nanograin film. *Appl. Phys. Lett.*, 99(10):102508, 2011.

[57] T. C. Ozawa, T. Taniguchi, Y. Nagata, Y. Noro, T. Naka, and A. Matsushita. Cu doping and pressure effect on a layered palladium oxide: $PbPdO_2$. *J. Alloys Compd.*, 395(12):32–35, 2005.

[58] H. M. Rietveld. A profile refinement method for nuclear and magnetic structures. *J. Appl. Crystallogr.*, 2(2):65–71, 1969.

[59] A.A. Coelho. TOPAS Academic V5, 2013.

[60] K. Momma and F. Izumi. *VESTA*: a three-dimensional visualization system for electronic and structural analysis. *J. Appl. Crystallogr.*, 41(3):653–658, 2008.

[61] G. Kieslich, C. S. Birkel, J. E. Douglas, M. Gaultois, I. Veremchuk, R. Seshadri, G. D. Stucky, Y. Grin, and W. Tremel. SPS-assisted preparation of the magneli phase $WO_{2.90}$ for thermoelectric applications. *J. Mater. Chem. A*, 1(42):13050–13054, 2013.

[62] R. D. Cowan. Pulse method of measuring thermal diffusivity at high temperatures. *J. Appl. Phys.*, 34(4):926–927, 1963.

[63] G. Kresse and J. Furthmüller. Efficiency of ab-initio total energy calculations for metals and semiconductors using a plane-wave basis set. *Comput. Mater. Sci.*, 6(1):15–50, 1996.

[64] G. Kresse, M. Marsman, and J. Furthmüller. Vienna ab-initio simulation package: VASP the GUIDE, 2012.

[65] P. E. Blöchl. Projector augmented-wave method. *Phys. Rev. B*, 50(24):17953–17979, 1994.

[66] G. Kresse and D. Joubert. From ultrasoft pseudopotentials to the projector augmented-wave method. *Phys. Rev. B*, 59(3):1758–1775, 1999.

[67] J. P. Perdew, K. Burke, and M. Ernzerhof. Generalized gradient approximation made simple. *Phys. Rev. Lett.*, 77(18):3865–3868, 1996.

[68] S. Curtarolo, W. Setyawan, G. L. W. Hart, M. Jahnatek, R. V. Chepulskii, R. H. Taylor, S. Wang, J. Xue, K. Yang, O. Levy, M. J. Mehl, H. T. Stokes, D.O. Demchenko, and D. Morgan. AFLOW: An automatic framework for high-throughput materials discovery. *Comput. Mater. Sci.*, 58:218–226, 2012.

[69] W. Setyawan and S. Curtarolo. High-throughput electronic band structure calculations: Challenges and tools. *Comput. Mater. Sci.*, 49(2):299–312, 2010.

[70] J. Heyd, G. E. Scuseria, and M. Ernzerhof. Hybrid functionals based on a screened coulomb potential. *J. Chem. Phys.*, 118(18):8207–8215, 2003.

[71] J. Brgoch, A. J. Lehner, M. Chabinyc, and R. Seshadri. Ab initio calculations of band gaps and absolute band positions of polymorphs of $RbPbI_3$ and $CsPbI_3$: Implications for main-group halide perovskite photovoltaics. *J. Phys. Chem. C*, 118(48):27721–27727, 2014.

[72] G.K.H. Madsen and D.J. Singh. BoltzTraP. A code for calculating bandstructure dependent quantities. *Comput. Phys. Commun.*, 175:67–71, 2006.

[73] R. D. Shannon. Revised effective ionic radii and systematic studies of interatomic distances in halides and chalcogenides. *Acta Crystallogr. Sect. A*, 32(5):751–767, 1976.

[74] I. D. Brown and D. Altermatt. Bond-valence parameters obtained from a systematic analysis of the Inorganic Crystal Structure Database. *Acta Crystallogr. Sect. B*, 41(4):244–247, 1985.

[75] K. Fujita, T. Mochida, and K. Nakamura. High-temperature thermoelectric properties of $Na_xCoO_{2-\delta}$ single crystals. *Jpn. J. Appl. Phys.*, 40:4644–4647, 2001.

[76] R. Funahashi and I. Matsubara. Thermoelectric properties of Pb- and Ca-doped $(Bi_2Sr_2O_4)_xCoO_2$ whiskers. *Appl. Phys. Lett.*, 79(3):362–364, 2001.

[77] M. Shikano and R. Funahashi. Electrical and thermal properties of single-crystalline $(Ca_2CoO_3)_{0.7}CoO_2$ with a $Ca_3Co_4O_9$ structure. *Appl. Phys. Lett.*, 82(12):1851–1853, 2003.

[78] R. R. Heikes and R. W. Ure. *Thermoelectricity: Science and Engineering*. Interscience Publishers, 1961.

[79] W. Koshibae, K. Tsutsui, and S. Maekawa. Thermopower in cobalt oxides. *Phys. Rev. B*, 62(11):6869–6872, 2000.

[80] W. Koshibae and S. Maekawa. Effects of spin and orbital degeneracy on the thermopower of strongly correlated systems. *Phys. Rev. Lett.*, 87(23):236603, 2001.

[81] D. J. Singh. Electronic structure of $NaCo_2O_4$. *Phys. Rev. B*, 61(20):13397–13402, 2000.

[82] T. Takeuchi, T. Kondo, T. Takami, H. Takahashi, H. Ikuta, U. Mizutani, K. Soda, R. Funahashi, M. Shikano, M. Mikami, S. Tsuda, T. Yokoya, S. Shin, and T. Muro. Contribution of electronic structure to the large thermoelectric power in layered cobalt oxides. *Phys. Rev. B*, 69(12):125410, 2004.

[83] K. Kuroki and R. Arita. Pudding Mold band drives large thermopower in Na_xCoO_2. *J. Phys. Soc. Japan*, 76(8):083707, 2007.

[84] S.L. Dudarev, G.A. Botton, S.Y. Savrasov, C.J. Humphreys, and A.P. Sutton. Electron-energy-loss spectra and the structural stability of nickel oxide: An LSDA+U study. *Phys. Rev. B*, 57:1505–1509, 1998.

[85] M.E. Gruner, U. Eckern, and R. Pentcheva. Impact of strain-induced electronic topological transition on the thermoelectric properties of $PtCoO_2$ and $PdCoO_2$. *Phys. Rev. B*, 92:235140, 2015.

[86] E. J. Skoug and D. T. Morelli. Role of lone-pair electrons in producing minimum thermal conductivity in nitrogen-group chalcogenide compounds. *Phys. Rev. Lett.*, 107(23):235901, 2011.

[87] Y. Laligant, A. Le Bail, and G. Ferey. Complex palladium oxides. V. Crystal structure of $LiBiPd_2O_4$: An example of three different fourfold coordinations of cations. *J. Solid State Chem.*, 81(1):58–64, 1989.

[88] N. Bettahar, P. Conflant, J. C. Boivin, F. Abraham, and D. Thomas. Electrical conductivity of $(Bi,Pb)_2MO_4$ (M = Pd,Pt) linear chain compounds. *J. Phys. Chem. Solids*, 46(3):297–299, 1985.

[89] A. A. Coelho, J. Evans, I. Evans, A. Kern, and S. Parsons. The TOPAS Symbolic Computation System. *Powder Diffr.*, 26(S1):S22–S25, 2011.

[90] L. K. Lamontagne, G. Laurita, M. Knight, H. Yusuf, J. Hu, R. Seshadri, and K. Page. The role of structural and compositional heterogeneities in the insulator-to-metal transition in hole-doped APd_3O_4 (A = Ca, Sr). *Inorg. Chem.*, 56(9):5158–5164, 2017.

[91] C. van der Marel, W. Geertsma, and W. van der Lugt. 7 Li Knight shift of liquid Li-Pb and Li-Sn alloys. *J. Phys. F Met. Phys.*, 10(10):2305, 1980.

[92] C. Marichal, J. Hirschinger, P. Granger, M. Menetrier, A. Rougier, and C. Delmas. ^{6}Li and ^{7}Li NMR in the $LiNi_{1-y}Co_yO_2$ solid solution ($0 \leq y \leq 1$). *Inorg. Chem.*, 34(7):1773–1778, 1995.

[93] E. Bekaert, F. Robert, P. E. Lippens, and M. Ménétrier. ^{7}Li NMR Knight shifts in LiSn compounds: MAS NMR measurements and correlation with DFT calculations. *J. Phys. Chem. C*, 114(14):6749–6754, 2010.

[94] J. He, S. Hao, Y. Xia, S. S. Naghavi, V. Ozoliš, and C. Wolverton. Bi_2PdO_4: A promising thermoelectric oxide with high power factor and low lattice thermal conductivity. *Chem. Mater.*, 2016.

[95] M. Fäth, S. Freisem, A. A. Menovsky, Y. Tomioka, J. Aarts, and J. A. Mydosh. Spatially inhomogeneous metal-insulator transition in doped manganites. *Science*, 285(5433):1540–1542, 1999.

[96] E. Dagotto, T. Hotta, and A. Moreo. Colossal magnetoresistant materials: The key role of phase separation. *Phys. Rep.*, 344(13):1–153, 2001.

[97] M. Baldini, T. Muramatsu, M. Sherafati, H.-k. Mao, L. Malavasi, P. Postorino, S. Satpathy, and V. V. Struzhkin. Origin of colossal magnetoresistance in $LaMnO_3$ manganite. *Proc. Natl. Acad. Sci.*, 112(35):10869–10872, 2015.

[98] P. M. Raccah and J. B. Goodenough. A localized electron to collective electron transition in the system (La,Sr)CoO_3. *J. Appl. Phys.*, 39(2):1209, 1968.

[99] J. Wu and C. Leighton. Glassy ferromagnetism and magnetic phase separation in $La_{1-x}Sr_xCoO_3$. *Phys. Rev. B*, 67(17):174408, 2003.

[100] D. Phelan, D. Louca, K. Kamazawa, S.-H. Lee, S. N. Ancona, S. Rosenkranz, Y. Motome, M. F. Hundley, J. F. Mitchell, and Y. Moritomo. Spin incommensurability and two phase competition in cobaltites. *Phys. Rev. Lett.*, 97(23):235501, 2006.

[101] C. He, S. El-Khatib, S. Eisenberg, M. Manno, J. W. Lynn, H. Zheng, J. F. Mitchell, and C. Leighton. Transport signatures of percolation and electronic phase homogeneity in $La_{1-x}Sr_xCoO_3$ single crystals. *Appl. Phys. Lett.*, 95(22):222511, 2009.

[102] K. Page, T. Kolodiazhnyi, T. Proffen, A. K. Cheetham, and R. Seshadri. Local structural origins of the distinct electronic properties of Nb-substituted $SrTiO_3$ and $BaTiO_3$. *Phys. Rev. Lett.*, 101(20):205502, 2008.

[103] K. Itoh and N. Tsuda. Metal to semiconductor like transition for sintered $Ca_{1-x}Na_xPd_3O_4$. *Solid State Commun.*, 109(11):715–719, 1999.

[104] I. Hase and Y. Nishihara. $CaPd_3O_4$ as an excitonic insulator. *Phys. Rev. B*, 62(20):13426–13429, 2000.

[105] M. M. Savosta and P. Novák. Two-phase character of metallic ferromagnetism in manganites. *Phys. Rev. Lett.*, 87(13):137204, 2001.

[106] P. L. Kuhns, M. J. R. Hoch, W. G. Moulton, A. P. Reyes, J. Wu, and C. Leighton. Magnetic phase separation in $\mathrm{La_{1-x}Sr_xCoO_3}$ by $^{59}\mathrm{Co}$ nuclear magnetic resonance. *Phys. Rev. Lett.*, 91(12):127202, 2003.

[107] O. Muller and R. Roy. *Synthesis and crystal chemistry of some new complex palladium oxides*, chapter 3, pages 28–38.

[108] K. Itoh, Y. Yano, and N. Tsuda. Metal to insulator transition for $Ca_{1-x}Na_xPd_3O_4$. *J. Phys. Soc. Japan*, 68(9):3022–3026, 1999.

[109] J. Neuefeind, M. Feygenson, J. Carruth, R. Hoffmann, and K. K. Chipley. The Nanoscale Ordered MAterials Diffractometer NOMAD at the Spallation Neutron Source SNS. *Nucl. Instruments Methods Phys. Res. Sect. B Beam Interact. with Mater. Atoms*, 287:68–75, 2012.

[110] C. L. Farrow, P. Juhas, J. W. Liu, D. Bryndin, E. S. Božin, J. Bloch, T. Proffen, and S. J. L. Billinge. PDFfit2 and PDFgui: Computer programs for studying nanostructure in crystals. *J. Phys. Condens. Matter*, 19(33):335219, 2007.

[111] S. Kaveh, C. P. Tremblay, N. Norhashim, R. J. Curry, and A. K. Cheetham. Phase separation in garnet solid solutions and its effect on optical properties. *Adv. Mater.*, 25(44):6448–6452, 2013.

[112] J. E. Douglas, P. A. Chater, C. M. Brown, T. M. Pollock, and R. Seshadri. Nanoscale structural heterogeneity in Ni-rich Half-Heusler TiNiSn. *J. Appl. Phys.*, 116(16):163514, 2014.

[113] J. J. Scheer, A. E. Van Arkel, and R. D. Heyding. Oxide complexes formed in the systems platinum metals: Alkali carbonates: Oxygen. *Can. J. Chem.*, 33(4):683–686, 1955.

[114] W. D. Knight. Nuclear magnetic resonance shift in metals. *Phys. Rev.*, 76:1259–1260, 1949.

[115] D. P. Tunstall and W. Ramage. A high-pressure NMR study of sodium tungsten bronze: Na_xWO_3. *J. Phys. C Solid State Phys.*, 13(5):725, 1980.

[116] M. Riccó, G. Fumera, T. Shiroka, O. Ligabue, C. Bucci, and F. Bolzoni. Metal-to-insulator evolution in $(NH_3)_xNaK_2C_{60}$: An NMR study. *Phys. Rev. B*, 68(3):35102, 2003.

[117] G. K. Ramachandran, J. Dong, O. F. Sankey, and P. F. McMillan. $^{23}\mathrm{Na}$ and $^{29}\mathrm{Si}$ NMR Knight shifts in the silicon clathrate $\mathrm{Na_{16}Cs_8Si_{136}}$. *Phys. Rev. B*, 63(3):33102, 2000.

[118] M. T. J. H. Lodge, P. Cullen, N. H. Rees, N. Spencer, K. Maeda, J. R. Harmer, M. O. Jones, and P. P. Edwards. Multielement NMR studies of the liquid–liquid phase separation and the metal-to-nonmetal transition in fluid lithium–and sodium–ammonia solutions. *J. Phys. Chem. B*, 117:13322–13334, 2013.

[119] N. F. Mott. The transition to the metallic state. *Philos. Mag.*, 6:287–309, 1961.

[120] M. Ménétrier, I. Saadoune, S. Levasseur, and C. Delmas. The insulator-metal transition upon lithium deintercalation from $LiCoO_2$: Electronic properties and ^{7}Li NMR study. *J. Mater. Chem.*, 9(5):1135–1140, 1999.

[121] K. Lee, D. Kaseman, S. Sen, I. Hung, Z. Gan, B. Gerke, R. Pöttgen, M. Feygenson, J. Neuefeind, O. I. Lebedev, and K. Kovnir. Intricate short-range ordering and strongly anisotropic transport properties of $Li_{1-x}Sn_{2+x}As_2$. *J. Am. Chem. Soc.*, 137(10):3622–3630, 2015.

[122] J. E. Douglas, C. S. Birkel, N. Verma, V. M. Miller, M.-S. Miao, G. D. Stucky, T. M. Pollock, and R. Seshadri. Phase stability and property evolution of biphasic TiNiSn alloys for use in thermoelectric applications. *J. Appl. Phys.*, 115(4):43720, 2014.

[123] M. L. C. Buffon, G. Laurita, N. Verma, L. Lamontagne, L. Ghadbeigi, D. L. Lloyd, T. D. Sparks, T. M. Pollock, and R. Seshadri. Enhancement of thermoelectric properties in the NbCoSn half-Heusler/Heusler system through spontaneous inclusion of a coherent second phase. *J. Appl. Phys.*, 120(7):75104, 2016.

[124] G. Li, B. Yan, Z. Wang, and K. Held. Topological dirac semimetal phase in Pd and Pt oxides. *Phys. Rev. B*, 95(3):35102, 2017.

[125] A. H. Castro Neto, F. Guinea, N. M. R. Peres, K. S. Novoselov, and A. K. Geim. The electronic properties of graphene. *Rev. Mod. Phys.*, 81(1):109–162, 2009.

[126] CASM Developers. Casmcode: v0.2.1, April 2017.

[127] J. C. Thomas and A. Van der Ven. Finite-temperature properties of strongly anharmonic and mechanically unstable crystal phases from first principles. *Phys. Rev. B*, 88:214111, 2013.

[128] B. Puchala and A. Van der Ven. Thermodynamics of the zr-o system from first-principles calculations. *Phys. Rev. B*, 88:094108, 2013.

[129] A. Van der Ven, J. C. Thomas, Q. Xu, and J. Bhattacharya. Linking the electronic structure of solids to their thermodynamic and kinetic properties. *Math. Comput. Simul.*, 80(7):1393–1410, 2010.

[130] S. P. Ong, W. D.n Richards, A. Jain, G. Hautier, M. Kocher, S. Cholia, D. Gunter, V. L. Chevrier, K. A. Persson, and G. Ceder. Python Materials Genomics (pymatgen): A robust, open-source python library for materials analysis. *Comput. Mater. Sci.*, 68:314–319, 2013.

[131] Z. Fu and W. Li. Phase transition, phase transition temperature and crystal structure of a new compound - Ca_2PdWO_6. *Sci. CHINA Math.*, 39(9):981–990, 1996.

[132] M. Z. Hasan and C. L. Kane. Colloquium: Topological insulators. *Rev. Mod. Phys.*, 82(4):3045–3067, 2010.

[133] L. Müchler, H. Zhang, S. Chadov, B. Yan, F. Casper, J. Kübler, S.-C. Zhang, and C. Felser. Topological insulators from a chemists perspective. *Angew. Chemie Int. Ed.*, 51(29):7221–7225, 2012.

[134] D. Kong and Y. Cui. Opportunities in chemistry and materials science for topological insulators and their nanostructures. 3:845, 2011.

[135] Z. K. Liu, B. Zhou, Y. Zhang, Z. J. Wang, H. M. Weng, D. Prabhakaran, S.-K. Mo, Z. X. Shen, Z. Fang, X. Dai, Z. Hussain, and Y. L. Chen. Discovery of a three-dimensional topological dirac semimetal, Na_3Bi. *Science*, 343(6173):864 – 867, 2014.

[136] Z. K. Liu, J. Jiang, B. Zhou, Z. J. Wang, Y. Zhang, H. M. Weng, D. Prabhakaran, S.-K. Mo, H. Peng, P. Dudin, T. Kim, M. Hoesch, Z. Fang, X. Dai,

Z. X. Shen, D. L. Feng, Z. Hussain, and Y. L. Chen. A stable three-dimensional topological Dirac semimetal Cd_3As_2. *Nat. Mater.*, 13:677, 2014.

[137] Q. D. Gibson, L. M. Schoop, L. Muechler, L. S. Xie, M. Hirschberger, N. P. Ong, R. Car, and R. J. Cava. Three-dimensional dirac semimetals: Design principles and predictions of new materials. *Phys. Rev. B*, 91(20):205128, 2015.

[138] B.-J. Yang and N. Nagaosa. Classification of stable three-dimensional Dirac semimetals with nontrivial topology. 5:4898, 2014.